



On-a-chip microdischarge thruster arrays inspired by photonic device technology for plasma television

A feasibility study

Final Report

Authors: A.N. Grubisic, S.B. Gabriel, L. Jiang

Affiliation: School of Engineering Sciences, University of Southampton

Authors: A. Cranny, M. Kraft, N.M. White

Affiliation: School of Electronics and Computer Science, University of Southampton

ESA Research Fellow: Cristina Bramanti

Date: May 2009

Steven Gabriel

Tel: +44(0)2380 593222

e-mail: sbg2@soton.ac.uk

Leopold Summerer

Tel: +31(0)715656227

Fax: +31(0)715658018

e-mail: act@esa.int



Available on the ACT website
<http://www.esa.int/act>

Ariadna ID: 07/3108

Study Type: Standard (4 months)

Contract Number: 20760/07/NL/CB

EXECUTIVE SUMMARY

This study shows that the practical scaling of a hollow cathode thruster device to MEMS level should be possible albeit with significant divergence from traditional design. The main divergence is the need to operate at discharge pressures between 1-3bar to maintain emitter diameter pressure products of similar values to conventional hollow cathode devices. Without operating at these pressures emitter cavity dimensions become prohibitively large for maintenance of the hollow cathode effect and without which discharge voltage would be in the hundreds of volts as with conventional microdischarge devices. In addition this requires sufficiently constrictive orifice diameters in the $10\mu\text{m} - 50\mu\text{m}$ range for single cathodes or $<5\mu\text{m}$ larger arrays. Operation at this pressure results in very small Debye lengths ($4 - 5.2\text{pm}$) and leads to large reductions in effective work function ($0.3 - 0.43\text{eV}$) via the Schottky effect. Consequently, simple work function lowering compounds such as lanthanum hexaboride (LaB_6) can be used to reduce operating temperature without the significant manufacturing complexity of producing porous impregnated thermionic emitters as with macro scale hollow cathodes, while still operating $<1200^\circ\text{C}$ at the emitter surface. The literature shows that LaB_6 can be deposited using a variety of standard microfabrication techniques.

One significant challenge is the need to use an orifice plate to increase upstream pressure; the ion density within individual cathodes and in particular contacting the orifice remains very high. In a traditional approach, some design solutions in this report considered the orifice at either cathode potential or as an insulator. This results in significant ion losses from the plasma and large reductions in total efficiency ($<3\%$). A solution was to form the orifice as part of the anode itself to limit ion recombination by repulsion. As a consequence this design solution gives much higher thrust efficiencies ($>7\%$) and was selected for use in each subsequent design. It was also found that to avoid the use of ballast resistors due to the negative resistance characteristic of hollow cathodes, arrays must be operated in the abnormal glow mode to ensure equal current flow in each cathode. Knudsen and Reynolds numbers would also indicate that the flow is laminar and in a continuum regime throughout cathodes at these pressures and temperatures.

Several design solutions have been proposed to meet the general thrust requirements of micro ($<20\text{kg}$) and pico ($<1\text{kg}$) spacecraft with varying levels of conservatism. In the case of the microspacecraft, which would require a minimum of 0.11mN of thrust, parametric analysis would show that it should be possible to develop a MEMS HC device to operate at $\sim 1.01\text{W}$ producing up to 155s specific impulse or 1.33W delivering 190s specific impulse with efficiencies between $7\% - 9\%$. The device size is largely governed by the cooling requirement and would be between 1.79mm^2 and 3.55mm^2 depending on how hot ($1000 - 800^\circ\text{C}$) the thruster was allowed to run. Larger thrusters, while operating at a cooler temperature, also require greater preheating power before ignition however this does not exceed 25% of the operating power for all design solutions. The study also shows that it should also be possible to deposit a parallel track tungsten filament heater on the surface of the chip for preheating ignition purposes whilst giving an operating voltage $<24\text{V}$ without too great a coverage area of the chip itself by careful selection of heater track length, width and height.

The picospacecraft concept which required a continuous thrust of only 0.014mN could be met with operating powers of only $0.12 - 0.21\text{W}$ for specific impulse of 155s and 190s respectively. The array configuration of 100 cathodes however required very small orifices of $0.5\mu\text{m}$ to give sufficient backpressure. This is on the limit of MEMS manufacture given that the orifice also had to be $25\mu\text{m}$ in length to give sufficient dissipation. This solution also resulted in high orifice current

densities $\sim 450 \text{ A/mm}^2$ far in excess of current densities in conventional cathodes; consequently this was the only design solution which did not seem reasonable.

The study shows that the practical reality of fabricating a MEMS based hollow cathode thruster means that production of scaled down versions of conventional cathodes is geometrically not possible. Manufacture on a wafer limits the possible geometries based on the range of possible processing technique to achieve the end result. The various methodologies have been reviewed, as have the possible design variations and processes required in realising this objective. MEMS-based solutions will not be able to reproduce conventional geometries however the study has shown that it should at least be feasible to produce device conducive to a functional hollow cathode and thruster.

An obvious difference between this MEMS hollow cathode thruster and its macro-scale counterpart is the location of the heater element. It is not possible to place the heater concentrically around the thruster body since cathodes have to be manufactured through a solid wafer so it must be produced as a track on the wafer itself. The use of a Silicon-on-Insulator (SoI) wafer in the fabrication of a microthruster has the advantage that it removes two process steps, *viz* the deposition of the anode layer and electrode separating insulation layer cathode longitudinal axis. This type of wafer comprises two layers of silicon, referred to as the handle wafer and the device wafer, separated by a silicon dioxide insulating layer. An alternative fabrication route is to use just a single silicon wafer to form the cathode structure and to then fabricate the anode from a metallisation layer deposited on the top surface of the wafer. This method would seemingly be simpler to fabricate and has the advantage that the heater element can be located closer to the emitter layer, at the orifice end of the hollow cathode structure, which is not possible with the SoI implementation. With this arrangement, it would be necessary to open a window in the anode layer to permit electrical connection to the underlying heater.

The minimum thickness of the handle wafer required has been shown to be of the order of 300 microns. This will have repercussions on the minimum geometries of each of the generic device versions illustrated in the Figure below. In particular, the fixed angle of the sloping walls that define the thruster nozzle of the anisotropically wet etched devices (54.7°) means that the nozzle throat width and the overall device width are directly related to the anode thickness. The same is not true, however, of those devices where the nozzle in the anode is fabricated using the deep reactive ion etching technique, since here the nozzle throat width is entirely independent of the anode thickness. Clearly, for a given thickness of anode layer, a greater packing density of microthruster devices can be achieved for designs where the thruster nozzle is formed by the deep reactive ion etching technique than for those where the nozzle is formed by anisotropic wet etching. In the case of the SoI the handle layer can take the form of the anode layer. Since the heater should be located close to the emitter it would seem intuitive to use the anode layer as the handle and locate the heater directly behind the emitter on the rear of the wafer.

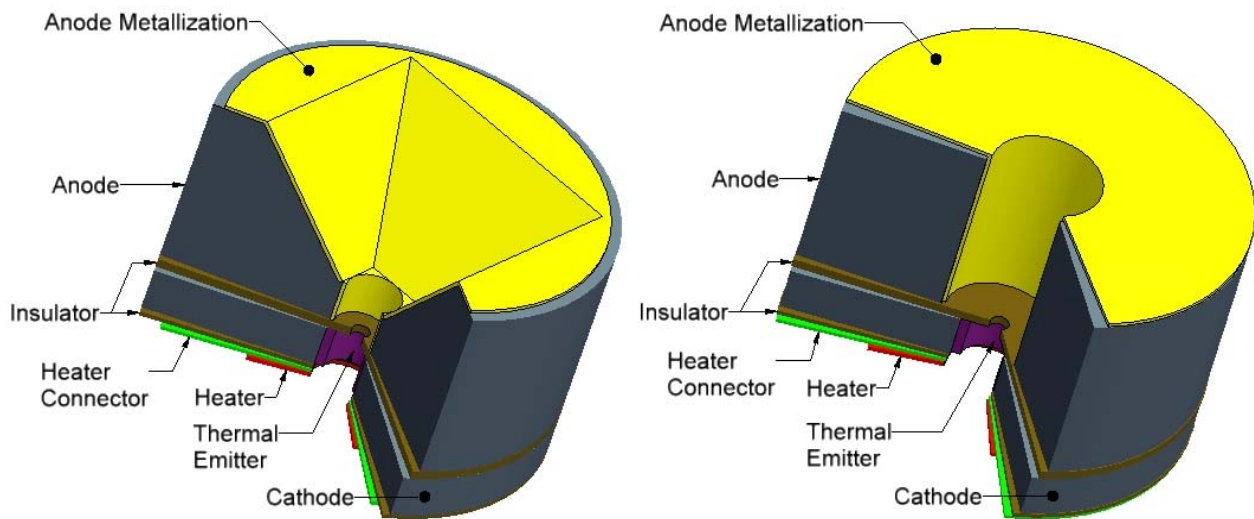


Figure: Cut-away isometric views of cathode apertures

To avoid the potential ‘show-stopper’ situation attributable to the operating temperature being comparable with or higher than the operating point of the material from which the hollow cathode thruster is fabricated and thereby affecting mechanical structural integrity, a number of different design strategies have been investigated where this problem should be reduced or negated. Of these, three different design philosophies have been identified as offering the safest mitigation routes, whilst still being practicable, namely:

1. A device based on silicon and using conventional thermal emitter materials with a high temperature plasma, but where critical and exposed regions of the silicon construction have been sufficiently thermally insulated to prevent structural damage.
2. A device based on silicon using a thermal emitter material of lower work function, such that the plasma is initiated and sustained at an operating temperature well below the melting point of silicon.
3. A device based on a different micro-machineable material as the underlying structure with a higher melting point than silicon.

Since the operating parameters of the thruster fall well within the general resource constraints of small spacecraft and the MEMS processes to produce a functionally comparable device to current hollow cathode thrusters it is anticipated that the successful development of a hollow cathode microthruster on a chip would seem feasible from an operation and manufacturing viewpoint.

TABLE OF CONTENTS

EXECUTIVE SUMMARY	2
TABLE OF CONTENTS	i
LIST OF FIGURES	iii
LIST OF TABLES	iv
NOMENCLATURE	v
PART 1: HOLLOW CATHODE THRUSTERS: SCALING AND MINIATURIZATION	1
1. Introduction	1
1.1. Hollow Cathode Thrusters at Present	1
1.2. Hollow Cathode Thruster Application	1
1.2.1. As a Primary Propulsion System	1
1.2.2. As a Secondary Propulsion System	2
2. Hollow Cathode Thruster Operation	3
2.1. Ignition and Operating Description	3
2.2. Spot and Plume Modes	5
2.3. Thrust Mechanism	6
2.4. Propellant Selection	6
3. Hollow Cathode Emitter Miniaturisation	7
3.1. Scaling of a Micro-Hollow Cathode	8
3.1.1. Electrical Breakdown	8
3.2. Maintaining the Hollow Cathode Effect	10
3.3. Micromanufactured Microdischarge Devices	12
3.4. Micromanufactured Arrays	14
3.5. Gas Temperature	15
3.6. Materials Compatibility	15
4. Thermionic Emitter Selection	16
4.1. Field Emitting Arrays (FEA)	16
4.2. Thermionic Emitters	17
4.2.1. Oxide Cathodes	18
4.2.2. Impregnated Cathodes	18
4.2.3. Boride Cathodes	19
5. Heater Design	19
6. Hollow Cathode Micro-Thruster Design Exercise	21
6.1. Parametric Model	21
6.1.1. Emitter Surface	21
6.1.2. Plasma Power Balance	22
6.2. Insert Processes	23
6.2.1. Emitter	23
6.2.2. Plasma Electrons	24
6.3. Orifice Processes	24
6.4. Discharge Parameters	26
6.5. Energy Conservation	27
6.6. Anode Cooling	28
6.7. Preheating Energy Balance	29
6.8. Lifetime Estimation	29
6.9. Design Iteration 1	30
6.10. Design Iteration 2	36

6.11.	Design iteration 3	41
6.11.1.	Series Heater	44
6.11.2.	Parallel Heater	45
7.	Discussion	46
7.1.	Concepts	46
7.2.	Parametric Scaling Results	47
7.3.	Microspacecraft Concept	49
7.4.	Picospacecraft Concept	50
7.5.	Empirical Comparisons	50
8.	References	52
PART 2: MEMS PRODUCTION PROCESSES, DESIGN CONSIDERATIONS AND CONSTRAINTS		58
9.	Introduction	58
10.	MEMS Design Considerations	59
10.1.	Scaling Issues	60
10.2.	Base Material Selection	61
10.3.	Generic Design Geometries	63
11.	Micro-Thruster Body Designs	66
11.1.	Thermally Insulated Devices	66
11.2.	Low Work Function Devices	68
11.2.1.	Lanthanum Hexaboride (LaB ₆)	69
12.	Conclusion	71
13.	References	73
APPENDIX		76
14.	MEMS Processing Techniques	76
14.1.	Photolithography	76
14.1.1.	Subtractive Pattern Transfer	77
14.1.2.	Additive Pattern Transfer	77
14.2.	Subtractive Processes	78
14.2.1.	Wet Etching	78
14.2.2.	Dry Etching	80
14.2.3.	<i>Milling</i>	80
14.3.	Additive Processes	81
14.3.1.	Chemical Vapour Deposition	81
14.3.2.	Physical Vapour Deposition	81
14.3.3.	Thermal Oxidation	82
14.3.3.1.	Sol-Gel Deposition	83
14.3.3.2.	Spin Coating	83
14.3.3.3.	Ion Implantation	83
14.3.3.4.	Electrochemical Deposition	83
14.4.	Bonding	84
14.4.1.	Anodic Bonding	84
14.4.2.	Direct Bonding	84
14.4.3.	Eutectic Bonding	84
14.4.4.	Adhesive Bonding	84

LIST OF FIGURES

Figure 1 Internal schematic of a T5 cathode.....	4
Figure 2 Energy/particle flux within a cathode.....	5
Figure 3 Limiting specific impulse based on complete thermal to kinetic energy conversion.....	6
Figure 5 Schematic diagram of a typical Paschen curve (a plot of the breakdown voltage vs. the product of pressure and planar electrode separation).....	8
Figure 6 Breakdown voltage vs. the gap spacing at the pressure of 760 torr in argon (a) and air (b). For both gases, solid curves represent theoretical predictions obtained by using the analytical solutions with the inclusion of field emission, while the dashed line corresponds to the standard Paschen law.....	9
Figure 7 Characteristics of electrical discharge transitions	11
Figure 8 Type-1, 2 and 3 cathodes etched into a silicon wafer.....	12
Figure 9 SEM image of 3×3 arrays of (50 μm) ² devices in a circular arrangement with separate power feed	14
Figure 10 Relationship between operating temperature and work function for emission currents of 0.5mA and 50mA at the respective emitter geometries neglecting field enhancement.....	18
Figure 12 Sputtering yield for molybdenum.....	30
Figure 13 Relative power contributions.....	31
Figure 14 Current density and operating power relative to aspect ratio	31
Figure 15 Operating pressure and emitter diameter relative to orifice aspect ratio.....	32
Figure 16 Required chip dimensions for adequate cooling at 800 and 1000C relative to orifice aspect ratio	33
Figure 17 Emitter operating temperature and diameter relative to orifice aspect ratio	34
Figure 18 Electric field strength and effective work function relative to orifice aspect ratio	34
Figure 19 Time for orifice diameter to reach 98% of its	35
Figure 20 Discharge current and total efficiency with respect to orifice length.....	36
Figure 21 Representation of the +Ve orifice hollow cathode	37
Figure 22 Discharge parameters with respect to orifice length	37
Figure 23 Operating power and orifice resistance with respect to orifice length	38
Figure 24 Thrust efficiency of both the +Ve and -Ve hollow cathode with respect to orifice length.....	38
Figure 25 Required chip size for radiative cooling requirement with respect to orifice length	39
Figure 26 Preheating power requirement with respect to orifice length.....	39
Figure 27 Emitter temperature with respect to orifice length	40
Figure 28 Directly heated lanthanum hexaboride filaments	40
Figure 29 Specific impulse and total operating power with respect to propellant temperature.....	42
Figure 30 Relative power investment and total efficiency with increasing propellant temperature ..	42
Figure 31 Specific power and orifice current density with respect to specific impulse	43
Figure 32 Required discharge current and discharge voltage with respect to propellant temperature.....	43
Figure 33 Figure Required heater track length to maintain operation at 24Volts dissipating 1.43W (59.6mA).....	44
Figure 34 Figure Required track length width base on track number and height in a parallel heater circuit	45
Figure 35 Figure Track geometry required for 20 windings on each track of a parallel heater circuit to produce 1.43W at 24V with 59mA	46
Figure 36 Extrapolation of Hutchinson's results down to very small anode keeper separations	51
Figure 38 Cross-section through conceptual MEMS-based hollow cathode microthruster.	60
Figure 39 Cross-section through hollow cathode microthruster implemented on silicon wafer.	62
Figure 40 Alternative track connections to concentrically positioned heater element.	62

Figure 41 Generic variations for MEMS microthruster devices fabricated using a SoI wafer (not to same scale).....	64
Figure 42 Examples of thermally insulated silicon microthrusters. Left – thruster nozzle formed by anisotropic wet-etch and incorporating a chimney structure. Right – thruster nozzle formed by deep reactive ion etching and having no chimney structure.....	67
Figure 43 Cut-away isometric views of single thrusters depicted in Figure 42.....	68
Figure 44 Examples of microthrusters with low work function thermal emitters. Left – thruster nozzle formed by anisotropic wet-etch and incorporating a chimney structure. Right – thruster nozzle formed by deep reactive ion etching and having no chimney structure.....	69
Figure 45 Cut-away isometric views of single thrusters depicted in Figure 43.....	69
Figure 46 Process steps (top to bottom) for both subtractive and additive pattern transfer using positive and negative resists. (a) Deposition of functional material for subtractive pattern transfer process. (b) Coating of resist layer, either positive or negative. (c) Photolithography using dark-field mask or clear-field mask depending on resist type. (d) Developing resist. (e) Etching of functional material for subtractive pattern transfer technique or deposition of functional material for positive pattern transfer technique. (f) Removal of resist to leave pattern.....	78
Figure 47 Etch profiles for various techniques on a {100} silicon wafer.....	79

LIST OF TABLES

Table 1 Thrust requirements for micro and pico-spacecraft.....	2
Table 2 Propellant Characteristics.....	7
Table 3 Material properties for heater selection.....	20
Table 4 Individual track resistance for increasing track numbers.....	45
Table 5 Preliminary device criteria.....	47
Table 6 Parametric scaling results for both pico and micro spacecraft concepts for array, conservative and demanding configurations.....	48
Table 7 Minimum discharge voltage obtained from 3 types of cathode.....	51
Table 8 Comparison of major parameters for Hutchinson's cathode and the parametric model results for Hutchinson's cathode and also the conservative and demanding microspacecraft designs.....	52
Table 9 Wafer diameters (mm) and layer thicknesses (μm) of some 'Silicon on Insulator' wafers..	61
Table 10 Minimum device widths (W) for thruster nozzles with chimneys fabricated by anisotropic etching as a function of hollow cathode internal diameter (D) and chimney length (L).....	65
Table 11 Examples of wet etchant recipes.....	79
Table 12 Etch chemistries for different etching processes.....	80

PART 1: HOLLOW CATHODE THRUSTERS: SCALING AND MINIATURIZATION

1. Introduction

Part 1 of this report focuses on understanding the influence of terminal parameters such as discharge current, mass flow rate and cathode geometry on micro hollow cathode performance. Several possible design configurations are then offered based on varying degrees of conservatism. Part 2 focuses on the possible means of manufacture of a micro hollow cathode device and suggests typical processes which could be applied to produce some of the design solutions offered in part 1.

1.1. Hollow Cathode Thrusters at Present

Recently at the University of Southampton, a new form of thruster termed the hollow cathode thruster (HCT) has been researched based on the T5 and T6 hollow cathodes [1-5]. These particular cathodes are a mature technology developed extensively over the last 35-years for application on the UK-10, UK-25, T5 and T6 gridded ion thrusters [6-11] and as an electron source for various ion beam neutralisation applications [12]. Early testing by Gessini *et al* confirmed that usable thrusts (~1mN) could be generated with reasonable specific impulse (~300s) using the T6 cathode with no attempt at optimisation [4]. However, thrust efficiencies remained very low, <0.5%, with a total power of around 800W. Further development by Grubisic *et al* has shown that by optimising aspects of HCT design, the T6 high current hollow cathode can operate as a low power MPD thruster delivering over 1050s specific impulse. Grubisic *et al* have also shown that by reducing orifice diameter of cathodes to enhance Ohmic heating (discussed in Section 6) as in the T5 hollow cathode, thrust efficiencies over 16% can be generated forming a low power (<80W) diffuse discharge thermal arcjet. In this case, thrusts in the milli-Newton range can be generated with specific impulse over 400s with argon.

1.2. Hollow Cathode Thruster Application

With its current baseline performance and low operating power (10-80W) the T5 HC may present a microthruster suitable for smaller satellites (<150kg) which have typically relied on only the simplest propulsion systems due to the severe resource constraints (power, regulation, mass, volume, cost) on small spacecraft. In particular, satellites in the 1-20kg range have even greater restriction on their propulsion systems and would benefit the most from development of a higher performance low power electrothermal thruster. The advent of MEMS (micro-electro-mechanical-systems) technologies may provide a means to build highly miniaturised low power (0.1-5W) on-chip devices suitable as relatively high performance electrothermal propulsions systems.

1.2.1. As a Primary Propulsion System

As demands on small spacecraft also continue to grow for missions such as formation-flying, inspection and rendezvous, requiring drag compensation, constellation phasing and proximity

manoeuvring [13], conventional robust microsatellite propulsion systems such as cold gas thrusters and resistojets can not deliver sufficient performance. Due to the high density-specific impulse (a term used in more volume limited spacecraft) required on microsatellite platforms, xenon has become a generally preferred propellant due to its high storage density and inert nature. However, its high molecular mass limits the performance of cold gas thrusters and resistojets to between 15-48s specific impulse [14, 15]. While resistojet performance is materials temperature limited, hollow cathode thrusters are able to sustain a plasma temperature well above wall temperatures (discussed more fully in Section 6) and thus present an opportunity for much greater performance through direct propellant heating. Guidelines issued by the Inter-Agency Space Debris Coordination Committee (IADC) also recommend that spacecraft in low earth orbit have the ability to deorbit within 25-years. This increases the mission delta-V by some 100-500% for typical earth observation missions and calls for a solution particularly for small satellites <150kg [16].

While a hollow cathode microthruster on-a-chip may give improvements in performance, the diffuse arc in the hollow cathode permits operation at convenient discharge voltages (10-25V) for microsatellites with limited power electronics, especially when compared to other electrothermal, electrostatic or electromagnetic thrusters [17]. As previously mentioned a hollow cathode microthrusters system would be able to draw from existing inert propellant storage and feed architectures for conventional cold gas/resistojet systems which find considerable use on small satellites due to their simplicity and low cost nature. This makes their addition a reasonably simple process. The inert propellant also bears no contamination risk to sensitive spacecraft equipment when compared with other thrusters in the milli-Newton thrust range such as PPTs (Pulsed Plasma Thrusters), colloid and FEEP (Field Emission Electric Propulsion) thrusters [18]. Hollow cathode thrusters may therefore be a fitting compromise of performance, simplicity, cost, and onboard resources.

This study will take 3 small spacecraft configurations as examples of thrust requirements for hollow cathode microthrusters with associated mass and inertial characteristics. These examples are shown in Table 1. Since small impulse times are at least, at present limited, impulsive burn periods are assumed to be over 10-seconds per burn.

S/C Dimensions		Moment of Inertia (kgm ²)	Required Impulse Bit (Ns)						Min. Thrust for slew (mN)
Mass (kg)	Scale (m)		17mrad		0.3mrad		0.02mrad		
			20s	100s	20s	100s	20s	100s	
1	0.1	0.017	1.4×10^{-4}	2.9×10^{-5}	2.5×10^{-6}	5.1×10^{-7}	1.7×10^{-7}	3.4×10^{-8}	0.014
10	0.3	0.150	4.3×10^{-4}	8.5×10^{-5}	7.5×10^{-6}	3.0×10^{-6}	1.0×10^{-6}	1.0×10^{-7}	0.043
20	0.4	0.533	1.1×10^{-3}	2.3×10^{-4}	2.0×10^{-5}	4.0×10^{-6}	1.3×10^{-6}	2.7×10^{-7}	0.110

Table 1 Thrust requirements for micro and pico-spacecraft [19].

Spacecraft characteristics of 1kg, 10kg and 20kg are shown to require minimum thrust levels of 0.014mN, 0.043mN and 0.11mN respectively for a 10-second impulsive burn either side of a slew period of either 20 or 100s. These thrust levels are taken as baseline design criteria for the HCT-on-a-chip optimisation described in Section 6.

1.2.2. As a Secondary Propulsion System

Hollow cathodes may also represent an attractive propulsion device for both large and small spacecraft. Spacecraft which operate primary electrostatic or electromagnetic propulsion systems such as gridded ion thrusters and Hall thrusters are typically required to carry a secondary chemical

system for reaction/momentum control or to compensate for thrust misalignment [20-23]. These secondary systems constitute a large fraction of the overall propulsion system mass while they are only required to produce a small fraction of the total impulse. These systems also bring substantial cost increases in manufacture, assembly, integration, test operations and launch preparation primarily due to hazardous propellants [24].

A simpler solution would be to use a moderate performance secondary system able to operate from a common inert propellant with the primary system; however again, the high molecular mass of xenon limits the performance of cold gas thrusters and resistojets. If low power hollow cathodes can be optimised to show higher thrust efficiencies they may be well suited to this purpose. Recent concurrent design studies have highlighted the possibility of producing an all-electric lunar transfer orbiter utilising the T5 gridded ion thruster and 8 hollow cathode AOCS thrusters at less than 150kg wet mass [25]. A similar NEO rendezvous mission study utilising 3 microsattellites with T5 gridded ion thrusters and T6 hollow cathode thrusters also generated relatively low-cost spacecraft (50 M€ for the first and 30 M€ for subsequent spacecraft) with a wet mass of less than 120kg each [26].

2. Hollow Cathode Thruster Operation

This section gives a qualitative description of hollow cathode operation based on the current understanding in the subject.

2.1. Ignition and Operating Description

An internal cutaway of a representative T5 cathode is shown in Figure 1 which is at least functionally comparable to a HCT-on-a-chip. A tungsten filament heater is used to raise the temperature of an emitter ($>1000^{\circ}\text{C}$) sufficient for initial thermionic emission. A trigger voltage applied to an external electrode is typically used to initiate the discharge (15-200V). The orifice plate increases the internal pressure and generates sufficiently dense plasma within the internal volume to promote ion recombination at the emitter surface and the hollow cathode effect itself (described in Section 3). Self-heating is then maintained by the acceleration of ions through the sheath (region between the cathode and plasma column), which recombine on internal surfaces to form neutrals. Confining the plasma column within the hollow cavity of the cathode permits operation at low cathode fall voltages while allowing high currents to be carried.

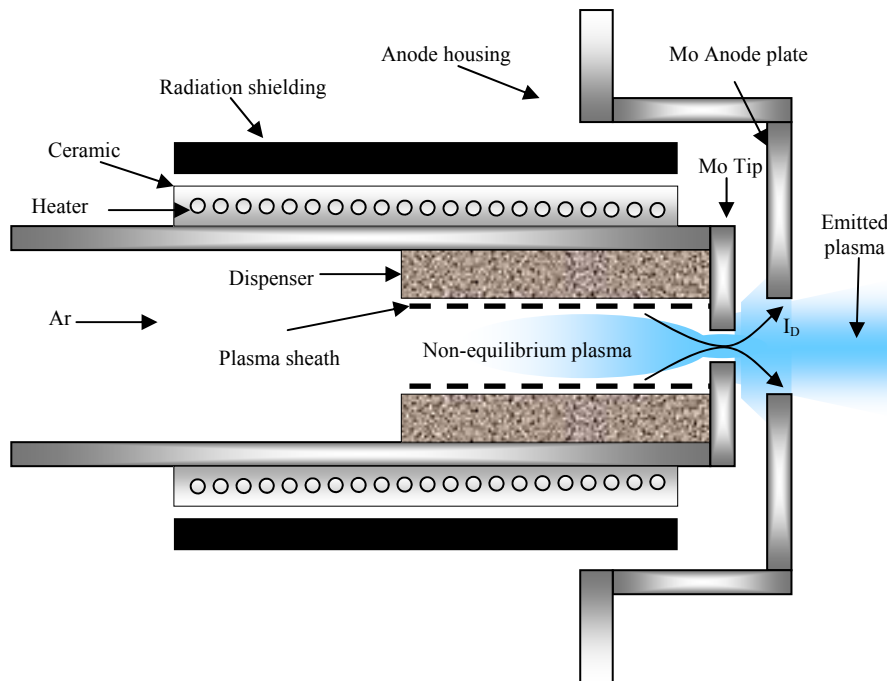


Figure 1 Internal schematic of a T5 cathode.

The plasma column induces sheath-enhanced emission at the emitter surface due to the intense field ($\sim 10^7 \text{V/m}$) between the plasma column and cathode potentials at a distance on the order of the Debye length. These impregnate constituents within the porous tungsten emitter undergo thermochemical reactions and liberate free Ba/BaO/CaO, which are adsorbed from the emitting surface during heating and operation. These components introduce a dipole and decrease the electronegativity barrier of the emitting surface, corresponding to a decrease in work function for thermionic emission [27]. Emitter life is generally based on the ability of the emitter to liberate free barium, where the rate of desorption is considered temperature dependant and a function of the emitted current density.

Thermionically emitted electrons are accelerated through the sheath potential and generally considered as a mono-energetic beam. The plasma potential within the emitter volume generally remains 6-10V above the cathode potential (however lower values are recorded in large orifice cathodes) consistent with the energy required for the excitation of meta-stable states of xenon (3P0 $\sim 9.45\text{eV}$, 3P2 $\sim 8.32\text{eV}$). Ion production is generally assumed to be achieved by multi-step processes firstly by electron impact of primary electrons from the atomic ground state [28] within the emitter volume, and then by lower energy thermalized electrons (2-6eV) within the orifice which then contribute significantly to the ionisation process. The total process thus requires transfer of at least the ionisation energy (12.13eV for xenon). The discharge current is drawn through the orifice toward the anode. Processes within the orifice dominate performance. The operating regime acts to maintain emitter temperatures for thermionic emission by balancing power deposition to the cathode with cooling by particle efflux and heat transfer to the surroundings.

Energy input to the plasma can be attributed to the energy of thermionically emitted electrons accelerated through the cathode fall and through Ohmic (collisional) heating within the orifice channel. While direct measurements have not fully characterised the processes following ignition, it is considered that xenon plasma initially forms between the orifice plate and the anode. This plasma extends into the hollow core of the cathode insert. Coupling of the electric field into this region drives the ionisation electrons that ultimately provide the breakdown of the main discharge. Since Ohmic heating of the plasma volume within the emitter is small compared to the orifice due to relative number densities in the respective volumes, orifice geometry drives resistive dissipation

and energy equipartition to the plasma. This is the prime propellant heating method and this process has a strong influence on performance as an electrothermal thruster as discussed in Section 5. A schematic of the energy flux within a cathode is shown in Figure 2. In the T5 cathode an ionisation fraction close to 1 has been found at the orifice exit [29] in comparison to other ion engine applications where gas utilisation is typically low (5-10%) indicating that full utilisation of the gas is possible at higher current densities.

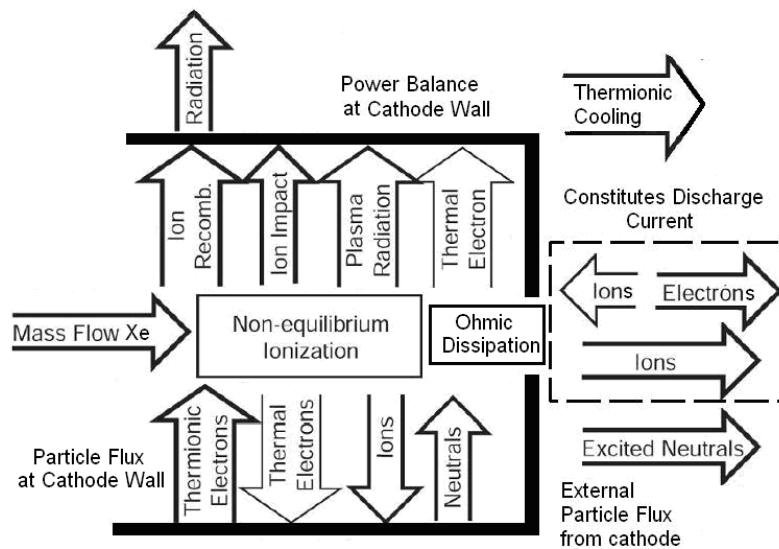


Figure 2 Energy/particle flux within a cathode.

2.2. Spot and Plume Modes

Spot and plume-modes are the two major discharge regimes considered in orificed hollow cathode design, especially important when operating off a small satellite bus at low powers. If the flux of ions into the cathode-anode gap is sufficient, the anode will passively collect the discharge current from the plasma without the presence of anode fall. This type of operation is referred to as spot mode. If the ion flux to the cathode-keeper gap is not sufficient for the anode to passively collect the electron current, an additional voltage drop forms between the plasma and anode to facilitate ionisation so that electrons can traverse the gap within the quasi-neutral plasma. This occurs as the mass flow rate or discharge current is decreased beyond a critical point and the combination of mass flow, discharge current and available anode area is not sufficient and is termed plume mode. Since in plume mode the ions created in the gap have some fraction of the cathode fall to accelerate them toward the cathode orifice plate, it exhibits ion sputtering [30] and discharge instabilities, which limit lifetime [31] and give high coupling voltages. As in cathode development for ion engines, consideration must be given to maintain reasonable discharge voltages and operating temperatures. Lifetime is normally limited by impregnate depletion in Kaufman type ion engines and ion sputtering in ring-cusp chamber designs. Application as an electrothermal thruster on-a-chip will demand high current densities within the orifice to maximise Ohmic heating therefore the maximum tolerable tip temperature for adequate thruster life will dictate the limiting current density and maximum acceptable power deposition into the orifice/anode. Operation at orifice plate temperatures below 1300°C has typically been used in development of low power low flow 3.2mm cathodes consistent with practices proven to enable lifetimes greater than 10,000 hr [32].

2.3. Thrust Mechanism

Plasma models suggest that cathodes are capable of generating peak heavy particle temperatures greater than 6,000K with wall temperature not exceeding 1,500K [33]. Laser Induced Fluorescence (LIF) has identified neutral temperatures in cathode-keeper gaps are between 1800-4000K, well above cathode wall temperature [34]. Experiment has also suggested heavy particle temperatures between 3200-6000K necessary to explain elevated backpressures within conventional cathodes [35]. The main mechanism of plasma heating is known to be Ohmic heating by plasma electrons within the cathode orifice with collisional heat transfer to the heavy particles [36]. This increase in heavy particle temperature within the orifice and an increased orifice pressure provides a means to produce higher exit velocities and thrusts, and consequently higher specific impulse. A thermal thrust mechanism with significant arc heating within the cathode would be possible while low wall temperatures are maintained (<1700K) given the low plasma densities contacting the orifice ($\sim 10^{20} \text{ m}^{-3}$) [37].

Assuming the orifice to be a simple cylinder the flow through the orifice can be assumed to choke and at the sonic speed since it is expelling into a hard vacuum. The thrust contribution at the orifice exit thus consists of components of momentum thrust and pressure thrust. Assuming a fully ionised flow at high orifice current densities, total thrust is given by:

$$F = \dot{m} \sqrt{\gamma R_{xe} T_i} + A_{or} (n_e k T_e + n_i k T_i) \quad (1.1)$$

Ambient pressure can be neglected since the thruster would be operating in vacuum.

2.4. Propellant Selection

When considering thermalisation of the propellant to produce thrust with xenon, krypton or argon, the theoretical limit to specific impulse (assuming full conversion of thermal to directed kinetic energy) is shown in Figure 3.

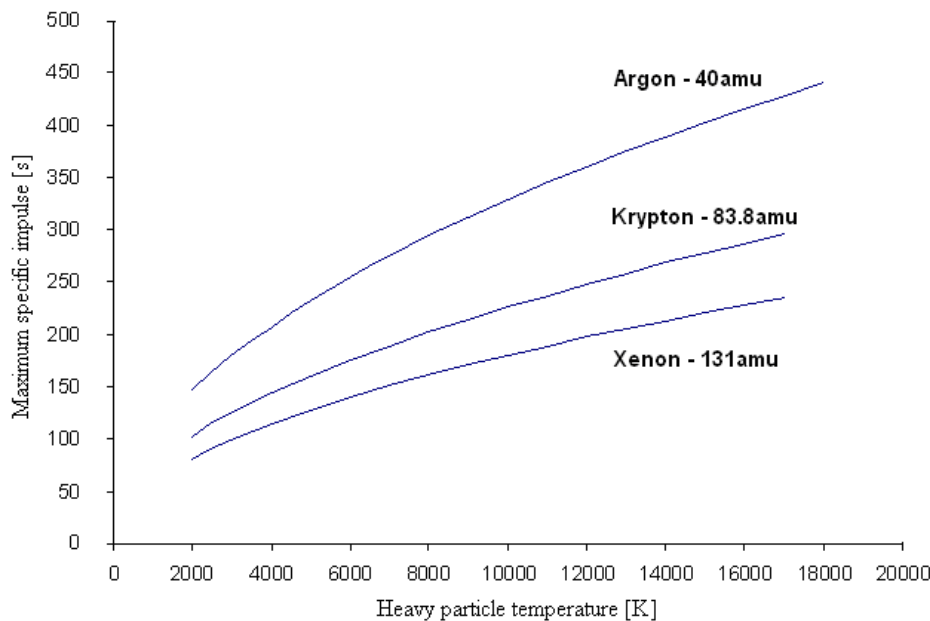


Figure 3 Limiting specific impulse based on complete thermal to kinetic energy conversion

As shown above, lighter propellants generate higher specific impulse, however lighter propellants generally possess lower storage densities and higher primary ionisation energies. The properties of xenon make it attractive for small satellite applications, which are generally more volume limited rather than mass limited. Xenon can maintain high storage densities of $1,570 \text{ kgm}^{-3}$ in gaseous form at approximately 69 Bar and 20°C . This makes the density-Isp (the product of the specific impulse and the propellant density) much higher than all other inert propellants. Crucially the factor that is of primary concern is not the mass of the tank but the storage density of the propellant. Maximising storage density also minimises the ballistic coefficient for the spacecraft by giving a high-density spacecraft with minimum cross sectional area and thus will help minimise orbit degradation at LEO due to atmospheric drag. The low primary ionisation energy of xenon, in comparison to all other inert gases, also minimises the loss of efficiency due to lower ionisation losses (a form of frozen flow loss) in the propellant also resulting in lower discharge voltages; important when scaling to MEMS level.

Mercury and caesium have also been considered as a potential propellant in the HCT. Mercury possesses a very high storage density, however its high mass produces poor electrothermal performance and it also possesses higher primary ionisation energy than all of the inert propellants. Caesium on the other hand has the lowest ionisation energy of all propellants, however it has a low storage density even as a solid, with a melting point of 28.4°C and requires heat input for vaporisation. This would significantly complicate the feed system which would have to deal with solid, liquid and gaseous forms of the propellant with no benefit in storage density. Mercury and particularly caesium also require significant handling and testing considerations due to their toxicity and reactivity. The design study described in section 6 and 7 thus considers xenon as the propellant of choice for the HCT-on-a-chip. Characteristics of the propellants considered are shown below in Table 2.

Propellant	Mercury	Caesium	Xenon	Krypton	Argon
Atomic number	80	55	54	36	18
Atomic mass [g.mol^{-1}]	200.59	132.90	131.29	83.80	39.95
Density at 20°C 1Bar [g.cm^{-3}]	13.6	1.9	5.9	3.73	1.78
Boiling point [$^\circ\text{C}$]	356	669	-107	-153	-185
Energy of first ionisation [kJ.mol^{-1}]	1007	375	1170	1351	1520
Energy of second ionisation [kJ.mol^{-1}]	1810	2234	2046	2350.4	2665

Table 2 Propellant Characteristics.

3. Hollow Cathode Emitter Miniaturisation

Creation of a low power HCT device in the 0.5-5W range while operating efficiently as a thruster ultimately requires miniaturisation of hollow cathodes for operation within this range. Development of MEMS level hollow cathode devices has been considered by many institutions as a means to produce a low cost high resolution array for applications such as flat panel displays. Scaling of hollow cathode devices as an electrothermal thruster requires similar considerations since attaining ignition and operation in the ‘hollow cathode’ mode for a microdischarge device requires a number of geometric and gas dynamic conditions to be met in combination with meeting thruster requirements. This section discusses the possibility and requirements for the scaling of arrays of hollow cathodes on a chip.

3.1. Scaling of a Micro-Hollow Cathode

Planar microdischarge devices fabricated in silicon were first developed in 1997 [38] with the first arrays developed in 1998 [39, 40]. Recent advances in materials processing have opened the door to confining low temperature, non-equilibrium plasmas to microcavities with characteristic dimensions as small as $10\mu\text{m}$ [41] and volumes below one nanolitre. Experiments have clearly demonstrated several of the unique characteristics of these plasmas, the foremost of which is the ability to operate continuously at gas or vapour pressures up to and beyond one atmosphere, and to do so with specific power loadings ranging from tens of kWcm^{-3} to 1MWcm^{-3} .

Micro hollow cathode discharges (MHCD) essentially obey two distinct scaling laws.

1. Electrical breakdown: The product of pressure (p) and anode cathode separation (d) for weakly-ionised ‘macroscopic’ plasmas obeys the well know Paschen breakdown law which applies to all discharge devices and determines the required breakdown voltage based on pd and the type of gas. See Figure 5. However for microscopic plasmas this relationship diverges at higher pressures
2. Oscillatory enhancement: A second scaling law unique to hollow cathode devices involves the product of pD (where D is the cathode opening diameter). If the product pD is in the range 0.1 to 10 Torr-cm the discharge develops in stages, each with a distinct V-I characteristic and allowing for the transitioning to hollow cathode mode, as discussed in greater detail in the next section.

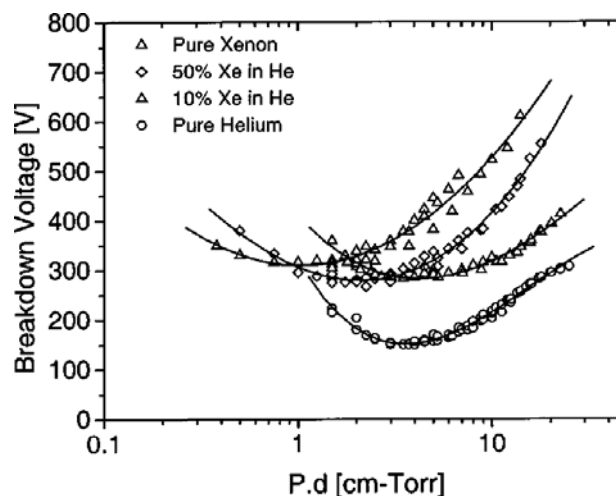


Figure 4 Schematic diagram of a Paschen curve (a plot of the breakdown voltage vs. the product of pressure and planar electrode separation) for various mixtures of xenon and helium [98].

3.1.1. Electrical Breakdown

Typical low pressure plasma discharges have electrode separations of centimetres to tens of centimetres, however at atmospheric pressure breakdown voltages in the kV range are required to ignite the discharge. In a high pressure discharge the breakdown voltage leads to a high current density after the discharge is ignited. The high current density is the source of discharge instabilities in the cathode fall region, which quickly leads to the formation of an arc and irreversibly damages the cathode which brings lifetime issues when considering thruster development. The study therefore aims to meet the requirement for a low voltage ignition.

As a consequence of pd scaling, the breakdown voltage can be kept low, if the electrode separation “ d ” is reduced when the pressure “ p ” is increased. At atmospheric pressure, d -value below 1mm is required to be near the minimum in the Paschen curve for essentially all gases. A pd value close to 1-Torr-cm corresponds to a minimum breakdown voltage [42] for pure xenon $\sim 300\text{V}$ increasing to $\sim 500\text{V}$ at 10 Torr-cm. It has been shown however that field-emission-related effects play a significant role in the deviation of the breakdown voltage from that predicted by Paschen's law in the range of micrometer gaps. Beginning from a certain gap spacing, breakdown voltage diverges from the climbing curve seen in the left half of the Paschen curve. DC breakdown voltage in microgaps depends on the gap size d and the pressure p , particularly, rather than on the product pd with inclusion of the field emission at micron and submicron gaps necessary to describe properly the experimental data.

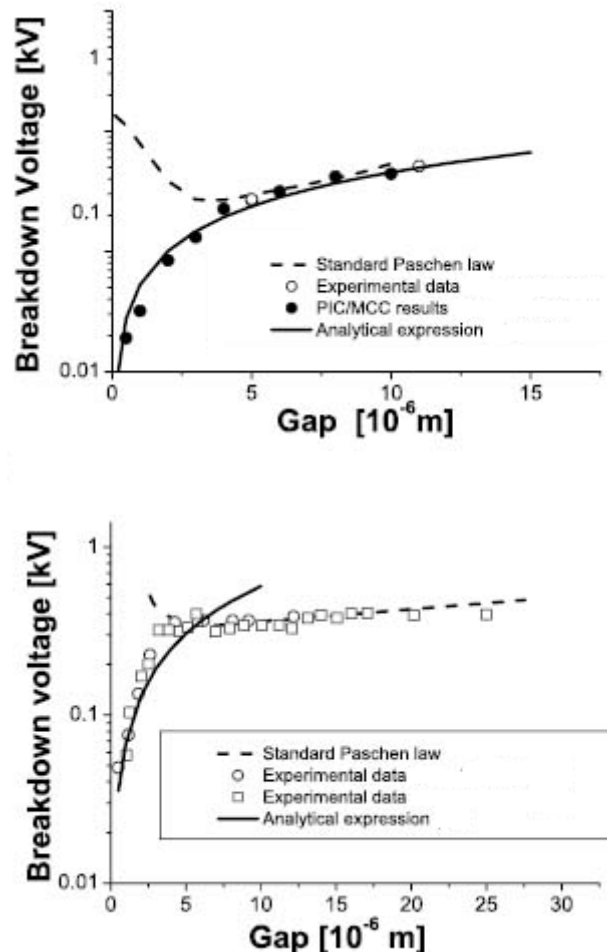


Figure 5 Breakdown voltage vs. the gap spacing at the pressure of 760 torr in argon (a) and air (b). For both gases, solid curves represent theoretical predictions obtained by using the analytical solutions with the inclusion of field emission, while the dashed line corresponds to the standard Paschen law. [40]

The source of electrons supporting avalanche breakdown in microgaps is field emission from the cathode due to the extremely high electric field. Inclusion of the field emission effect causes the rapid fall of the breakdown voltage in microgaps as shown in Figure 6. The variation of the breakdown voltage with respect to the pressure in microgaps does not show such a dramatic trend indicating that breakdown is no longer controlled by processes within the gas. At the gas pressure of 760 torr or higher, the electron mean path is of the order of a few micrometers so at small inter-electrode spacing breakdown is initiated by the secondary-emission processes instead of a gas avalanche process.

It should be noted that this breakdown condition implies that there is no pre-heating of the hollow cathode/emitter prior to ignition and thus no initial ionisation condition. In applications for ion thrusters, preheating of the emitter has been shown to reduce the breakdown voltage of the device to below 8V in some configurations since highly energetic electrons are able to influence the initial conductivity of the working gas [1]. Anode area and geometry also has been shown to play an important role in breakdown characteristics [2]. In the hollow cathode microthruster scaling of the appropriate geometries to meet the pd requirements will at least serve to minimise breakdown voltages as much as possible given the limited onboard resources.

Another factor that at least in part contributes to the stability of high-pressure microplasmas is the high losses of charge carriers to the surrounding walls at small scales. The typical operating parameters of microplasmas (pressures up to and exceeding 1 atm (760 Torr) and dimensions below 1 mm) correspond to pd values of between 1 and 10 Torr-cm. Similarly, hollow cathode microplasma devices have been found to operate stably in the rare gases for values of pd between 2 and 6 Torr-cm. The theoretical design in Section 6 thus considers the geometrical requirements and operating parameters necessary for the operation of a HCD with minimum ignition voltages.

3.2. Maintaining the Hollow Cathode Effect

An indication that MHCDs are not merely an extension of the low-pressure hollow cathode (HC) discharge to higher pressures is the fact that their observed stable operation at cathode openings of 250 μ m at atmospheric pressure (in air) violates the “White-Allis” similarity law [43, 44], which relates the discharge sustaining voltage V of a discharge to the product (pD) and the ratio (J/p), where J is the discharge current density, p is the pressure, and D is the diameter of the opening in the cathode. Thus, high-pressure operation of a HC discharge can be accomplished by reducing the size D of the hole in the cathode.

It is important to distinguish the importance of the hollow cathode effect and the difference in operating parameters between a hollow cathode and planar discharge. In a discharge between two planar electrodes, there are three main regions to consider. In the cathode fall region, electrons are accelerated. At the edge of the cathode fall, where the plasma potential is essentially constant, maximum electron kinetic energy occurs. Beyond that is the negative glow region, where electrons are slowed. The length of the negative glow region is proportional to the square of the voltage applied. Therefore, the power density of a planar glow discharge is limited because the glow region is spread over a long distance. The third region is the positive column, which makes up the remaining length of the cathode-anode distance.

The hollow cathode discharge (HCD) is a subclass of glow discharge and offers characteristics quite unique from that of a planar cathode [45]. At low currents in a MHCD a pre-discharge is observed. This is a glow discharge with the cathode fall generally outside the hollow cathode structure as in the planar discharge. Under these circumstances there is a single region of positive space charge and the electrons follow a path that is essentially determined by the direction of the vacuum electric field between the anode and cathode in the absence of a discharge. As the current increases the positive space charge region moves closer to the cathode and eventually enters the hollow cathode structure. A positive column, which then serves as a virtual anode, occupies the interior space of the MHCD between two separate sheath regions. This results in a change in electric field distribution forming a radial field and a potential well within the cavity causing a strong radial acceleration of electrons toward the cavity. This leads to an oscillatory motion of electrons within the cavity as they are accelerated into the virtual anode then repelled from the opposite cathode fall. Thus the path length of electrons is increased and these pendulum electrons can undergo many collisions with the background gas.

In this transition from axial to radial electric field, the voltage required to sustain the discharge dramatically drops as the current is increased. This results in a negative differential resistance characteristic and is distinctive of the hollow cathode mode. As the current is increased further the cathode sheath expands and the current voltage characteristic becomes that of a normal glow discharge with constant voltage at increasing current. Any further increase requires an increase in discharge voltage and thus transitions to an abnormal glow discharge. The theoretical upper limit of pressure (p_{max}) for HCD operation represents the transition to a normal glow discharge where discharge efficiency begins to decrease. The characteristics of the glow transitions are shown in Figure 7.

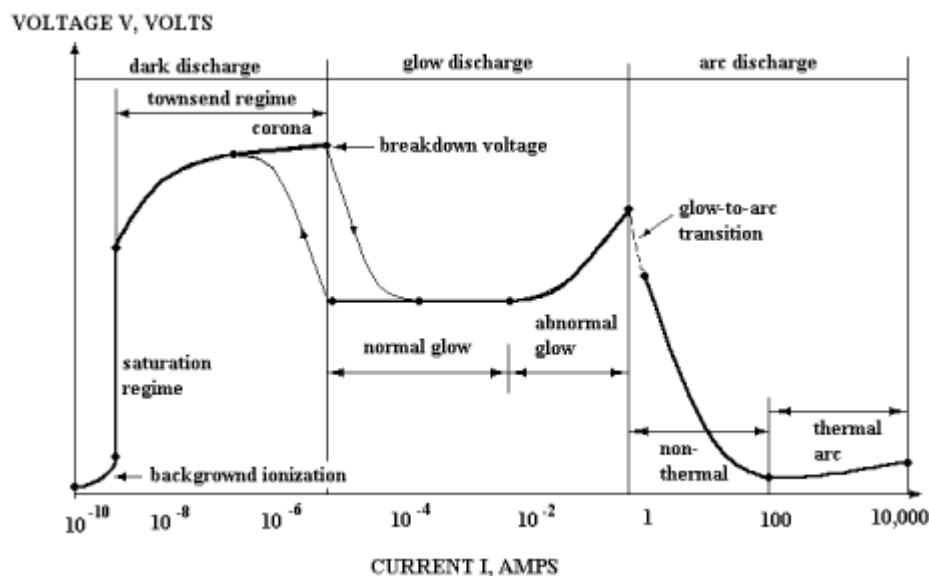


Figure 6 Characteristics of electrical discharge transitions

Early experiments by White [43] were conducted at a product of 7.5 Torr-cm in 100 Torr of neon. When the pressure is above this limit, the negative glow length will drop to below the cathode wall spacing and the oscillatory effect characteristic of the HCD will not be sustained. Therefore, reduction of the cavity dimensions allows a device to operate as a hollow cathode at higher pressure. A conventional hollow cathode discharge with cathode spacing in the centimetre range will typically operate at pressures up to a few Torr. The decrease in the diameter of a cylindrical cathode down to the micron level, for example, will permit an HCD to operate at pressures beyond one atmosphere.

The key features of the HCD over a planar discharge can be summarised as follows:

1. A HCD is associated with a large increased current density and discharge efficiency;
2. For given dimensions and voltage, the discharge current is only weakly influenced by gas pressure;
3. Finally, the HCD requires a lower operating voltage, reducing degradation by ion erosion and increasing the lifetime of the device. Lower operating voltage also simplifies the control electronics.

The design study in Section 6 thus considers the necessary geometrical and operational parameters necessary for operation in the hollow cathode regime.

3.3. Micromanufactured Microdischarge Devices

Micromachining and MEMS technology and processes have been explored as a means to further reduce the sizes of MHCDs as well as their costs. Because of the batch-nature of some micromachining processes, not only are the performance characteristics of the device improved but the cost of fabricating large arrays is also reduced.

Microcavity plasma devices have been fabricated in several materials platforms, including semiconductors, ceramics and multilayer metal/dielectric sandwiches. In recent years, researchers began to investigate methods for miniaturising discharge devices. Microdischarge devices have been made in molybdenum [46], silicon [47] and polymer/metal film structures [48]. The microcavities were generally made in these devices by drilling: mechanically, with ultrasound, or with a laser. However, the feature sizes that were made by using these methods are on the order of $75\mu\text{m}$ [45]. Devices made by such methods suffer from a number of flaws. First, the size of the cathode opening is large and its cross-section profile is not uniform. The wear of drill bits, along with normal mechanical inaccuracies, prevents achieving accurate dimensional control and repeatability. Second, due to the serial nature of the processes, it is expensive and time-consuming to realise a large array of such discharge devices. As a result two silicon bulk-micromachining techniques have been considered to create two distinct geometric profiles in the silicon substrate. These include deep reactive ion etching (DRIE) and anisotropic crystalline wet etching [49]. Thin film micro discharge arrays have also been fabricated based on a metal/polymer substrate structure [48].

Using the wet etching method, an inverted pyramid can be generated with the surfaces defined by $\{111\}$ crystal planes. These thin film devices consisting of pyramidal cathode structures around $50\mu\text{m} \times 50\mu\text{m}$ and $35\mu\text{m}$ in depth produced by wet etching with an $8\mu\text{m}$ polymer film and $1\mu\text{m}$ thick $\text{Si}_3\text{N}_4/\text{SiO}_2$ film forming the anode layer [50]. The overall depth of such cathodes is exactly determined by the width of the cavity opening due to the pyramidal plane structure. The DRIE process creates a hole with relatively vertical sidewalls. The depth of the holes is, in this case, independent of the cathode diameter. The former processes have been used to manufacture three forms of microdischarge device as shown in Figure 6 [51].

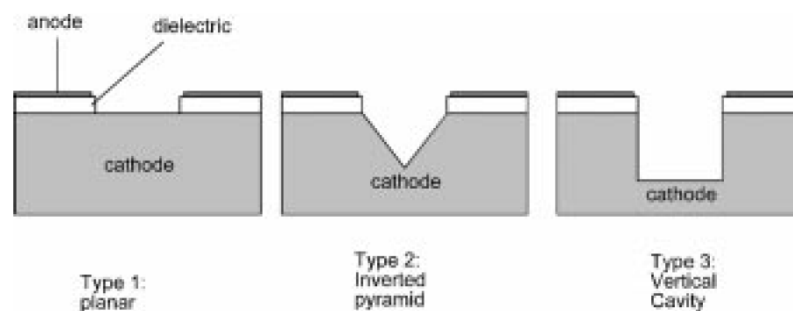


Figure 7 Type-1, 2 and 3 cathodes etched into a silicon wafer.

With reference to Figure 6, the three forms of microdischarge device are:

1. Planar microdischarge devices which do not have a cathode cavity (Type-1);
2. Microdischarge devices with inverted pyramidal cathodes (Type-2);
3. Microdischarge devices with hollow cylindrical cavity (Type-3).

Type-1 devices have consisted of a 1500\AA thick nickel thin film on top of an $8\mu\text{m}$ -thick polyimide dielectric layer, which is, in turn, deposited onto a $\{100\}$ silicon surface. The actual process of

creating the Type-2 device very different but it produces essentially the same physical device except for the inverted cavity. The Type-3 device is created using a DRIE etching process which enables the creation of vertical sidewalls rather than sloped $\{111\}$ surfaces.

In the School of Electronics and Computer Science at Southampton University, such fabrication techniques have been used to realise similar devices of even smaller size. For example, Figure 7 shows an array of inverted pyramids etched into a silicon wafer with an opening of $20\mu\text{m}$. The University of Southampton has used these devices for applications such as mirrors for optical cavities with very high finesse for so-called ‘Atom Chips’ [52, 53].

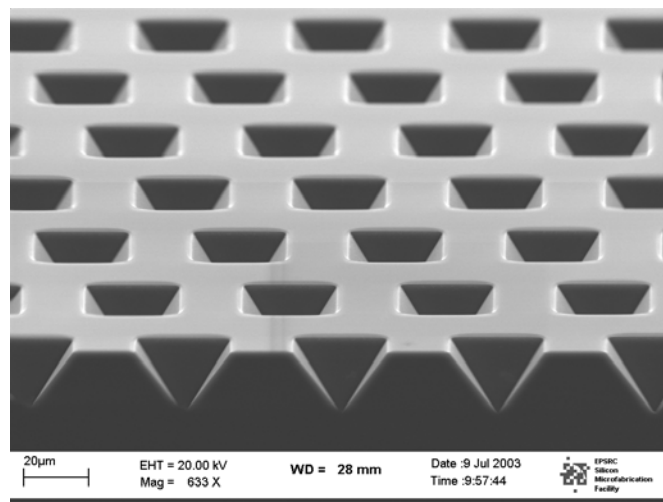


Figure 7: Array of Type-2 inverted pyramids etched into a silicon wafer.

Type 2 devices have shown insensitivity to operating pressure and discharge characteristics consistent with that of a hollow cathode discharge when operated between 400-800Torr with slightly reduced operating voltage when compared to Type-1 devices. Spectroscopic measurements have also confirmed that Type-2 devices do operate in a hollow cathode regime [54]. Type-3 devices have however showed an even greater reduction $\sim 100\text{V}$ in discharge voltage over the Type-2 devices and an order of magnitude increase in attainable current over the planar cathode design indicating that while inverted pyramidal cathodes do exhibit a hollow cathode type glow mode, the Type-3 device has much more desirable operating characteristics. It should also be noted that if the device is not operated well in to hollow cathode mode, there are also complications with operation of arrays in parallel, requiring ballast resistors due to the positive resistance slope, discussed more fully in the next section.

As previous studies have shown, the Type-3 device exhibits the most desirable operating characteristics and can be considered intuitive based on the previous description of hollow cathode operation in Section 2 and the ballistics of operation. Considering that in ideal current condition where the positive space charge region moves completely within the cathode structure, the positive column (virtual anode) acts to accelerate electrons through the sheath normal to the surface. Because the walls of the inverted pyramid are inclined at 54.7 degrees (determined by the silicon crystal structure) in a Type-2 device, there are some multiple reflections of electrons between the two sheath edges within the structure, particularly at depth. However the structure provides poor oscillatory containment of energetic electrons and after a finite number of reflections the electrons exit the cathode aperture. By comparison, in a Type-3 device energetic electrons are able to rebound from the cylindrical walls almost indefinitely until they transfer their energy to the bulk plasma via an ionising or excitation collision. The increase in apparent path length in a Type-2 device is therefore not as substantial as in a Type-3 device. While the manufacturing techniques are available for each type of device, Type-3 devices would seem the better use of the technology based on the

associated operating characteristics. A Type-3 device is thus explored in the design study in Sections 5 and Section 6.

3.4. Micromanufactured Arrays

These micromanufacturing techniques discussed previously have demonstrated the possibility of forming large arrays of up to 250,000 cathodes per device with cavity apertures as small as $(10\mu\text{m})^2$ [55] and it is likely that the future will see the development of arrays with smaller apertures possibly down to $1\mu\text{m}$ in diameter.

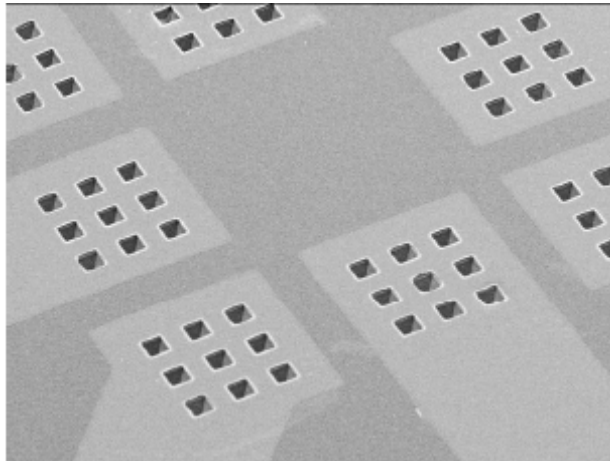


Figure 8 SEM image of 3×3 arrays of $(50\ \mu\text{m})^2$ devices in a circular arrangement with separate power feed [50].

Micromanufacturing has also shown it is possible to separate power feeds to the anodes of groups of 3×3 arrays as shown in Figure 8. This may bring possible advantages when considering thrust ranges and resolutions. Since operation in the hollow cathode mode requires quite a specific combination of electrode pressure and distance, maintaining this ratio may only be possible for a specific range of mass flow rates in each individual cathode. This means that each individual cathode has a finite thrust range of around 100-to-1 while maintaining hollow cathode operation. Increasing throttleability beyond this would require individual switching of groups or individual cathodes to attain the desired thrust range. The supporting micro-flow valve technologies have also been under development such as micro-piezoelectric actuators at the University of Uppsala [56] and micro-isolation valves at JPL [57]. The University of Southampton also has experience in fabricating such building blocks and microfluidic chips such as micro-machined pumps suitable for pumping gaseous media [58-60] integrated microfluidic circuit boards [61] and actuators that are suitable for valves [62]. These micro flow technologies are discussed more fully in Part 2.

Microdischarges can be operated in parallel without individual ballast resistors, if the discharges are operated in the range where the current–voltage ($I-V$) curve has a positive slope [63-67]. In regions where the $I-V$ characteristics have a negative slope (hollow cathode mode) or is flat (normal glow mode), arrays can be generated by using a distributed resistive ballast such as semi-insulating silicon as the anode material [68] or multilayer ceramic structures where each microdischarge is individually ballasted typically with a $3.96\text{k}\Omega$ load [69, 70]. These arrays have demonstrated operation at pressures of up to 1200 Torr to over 1-atmosphere in Neon, typically at discharge voltages of 90V delivering $\sim 35\text{mA}$ of current and having breakdown voltages $>1.2\text{kV}$. The resulting plasma resistance is on the order of $2.5\text{k}\Omega$. Individually ballasted cathodes may thus experience a factor of 3 loss of operating efficiency in the form of dissipated ballast heat even before considering cathode optimisation. One alternative is to operate in the pre-hollow cathode

discharge mode or in the abnormal glow mode [71]. However, this represents a very specific operating point and is thus likely to highly constrain the thrust range of any particular device unless some form of multiple device switching is included, which brings about additional considerations such as discrete feed and electrical systems.

When operated with Ni or Cu screens as the anode layer and operated beyond 300 Torr, these devices exhibit hollow cathode behaviour and have demonstrated lifetimes of hundreds of hours with no visible signs of deterioration.

The study in Section 5 thus considers two forms of device. Firstly a throttleable single cathode device which is able to operate alone with a continuous thrust range and secondly, multiple cathode arrays of which each cathode is operated in the abnormal glow mode and thus requires feed lines and electrical switching for throttleability.

3.5. Gas Temperature

The most recent advances on the behaviour of microplasmas has shown that cavities with d at least as small as $30\mu\text{m}$ is also described by the pd product extends the range in spatial dimension over which this scaling relationship remains valid. This also confirms that driving d further downwards will require gas pressures well beyond 1 bar [72]. These “ pd ” values are similar to those for large volume, low-pressure plasmas. However, the current and the energy densities in these microplasmas are much higher. This results in gas heating and momentum transfer from the electrons to the heavy particles and is of course beneficial as an electrothermal thruster. The heating process has been investigated somewhat since excimer laser emission (one application of microplasma devices) particularly in the UV spectrum is sensitive to heavy particle temperature, therefore most microplasma devices for this purpose are designed to limit heavy particle temperature and minimise gas heating [73].

Experimental studies [54] of microplasmas over a range of cavity geometries show the electron energy distribution to be non-Maxwellian with the local electron temperature (T_e) reaching 5 eV or more, depending upon the excitation conditions. The high specific power loadings characteristic of microplasma devices result in electron densities (n_e) typically in the 10^{14} – 10^{15}cm^{-3} range for dc operation. The temperature of the neutral gas is dictated by the gas or gas mixture in the microcavity, as well as the current density and the microcavity geometry. Both emission and absorption spectroscopic experiments reveal gas temperatures only 100–150K above ambient for rare gas microplasmas operated at dc. In contrast, discharges in air at atmospheric pressure are characterised by gas temperatures approaching 2000K due to increased dissipation and energy equipartition. In comparison, typical current densities in microarrays for operation at modest currents ~ 5 – 10mA are 16 – 33Acm^2 . It is worth noting that these current densities are at least two orders of magnitude less than in T5 hollow cathode experiments [70] and thus energy transfer to and from electrons to the heavy particles is minimised. Design considerations to promote gas heating are discussed more fully in Section 5.

3.6. Materials Compatibility

MEMS fabrication in silicon represents one of the roots of the field though little research has been conducted in the use of other materials for MEMS devices. The melting temperature of silicon $\sim 1414^\circ\text{C}$ is one of the main concerns in the current applications which traditionally use refractory metals and operate ~ 1000 – 1200°C . Appropriate coating of silicon with various inert materials, such as silicon nitride or metals (even gold) may easily be performed, and is common in the field of microfabrication. Coating with refractory metals may bring some reduction in the substrate

operating temperature; however the small scale and high conductivity of the materials involved means that this process is not able to produce substantial thermal standoff between the substrate and the working gas. Careful design conditions to maintain operating temperatures within the limits of silicon are discussed more fully in Part 2, thus possibly avoiding materials limitation issues. In this way some of the beneficial aspects of silicon can be included in a design such as its high thermal conductivity of about 150 W/mK [74]. This high conductivity has been exploited in the design of microelectronic circuits, the fabrication of which represents one of the roots of the field of MEMS. In the case of conventional thrusters such as MEMS resistojets, heat needs to be contained in the propellant to be turned into kinetic energy of the exhaust. In the case of the hollow cathode microthruster where wall temperature is significantly higher than the gas temperature the silicon base material presents an advantageous means to conduct heat away from the anode which is continuously heated during operation. Silicon also possesses relatively high emissivity [40] and therefore also provides a means to radiate the waste heat to the space environment. These design requirements will ultimately define chip geometries or packaging techniques. These scenarios are explored and discussed in Section 6 as a means to maintain acceptable operating temperatures based on heat fluxes.

Silicon, although very hard, is also a brittle material. Propulsion components may be required to potentially withstand many cycles of internal pressurisation. The behaviour of silicon under such conditions has not been studied at this scale, and sufficient factors of safety will need to be designed into MEMS propulsion components. Thruster components made from silicon will ultimately have to be joined to metal since even the smallest microspacecraft will require propellant tanks that will need to be conventionally machined (metal or metal-lined composites). These are discussed more fully in Part 2. Visions of tanks machined directly into silicon wafers are unfortunately far from feasible since this will not allow for enough propellant volume for even the smallest propulsion requirements. Joining of silicon chips, possibly via modules to metal tubes connected to the tank will also require leak-tight bonding.

4. Thermionic Emitter Selection

The ability of the MHCD to sustain a discharge is dependant primarily on the supply of electrons from the emitter surface. Electrons can be supplied by two principal mechanisms:

1. Field emission (FE)
2. Thermionic emission.

4.1. Field Emitting Arrays (FEA)

Two factors limit the application of field emitters to the problem: operating voltage and lifetime. Typically FE cathodes are operated in a close-spaced triode or diode configuration with one electrode as the anode. In an HCT system the FE cathode would have to operate in a triode configuration with a gate electrode and the upstream structure producing the virtual anode. The space-charge current limit depends on the plasma density and temperatures, electron beam energy and current density. The cathode lifetime will be limited because it will be subjected to constant ion bombardment. A self-generated ion population originates near the cathode when the electrons emitted by the cathode ionise ambient neutrals. These ions are accelerated to the cathode gate electrode or the emitting area of the cathode. The energy of these ions will depend on the potential where they are created. However, the ion flux depends on the cathode current, cathode potential, and local pressure. The local pressure can be determined from the thrust requirements as in Section 6. Since an electrothermal thruster would have to be operated at high pressure it follows that FE

cathodes would be subject to extremely intense ion bombardment, much more severe and damaging than in any other form of FE electric propulsion device. Secondly the voltages required for provision of currents in the mA range are in the 0.5kV range which increases the complexity of the power supply system. However, it has been shown that the energy threshold for sputtering Mo and Si FEA cathodes with xenon ions is 39eV and 48eV, respectively [75]. Spindt-type cathodes have demonstrated current densities greater than 2000 A/cm² from Mo [76, 77] FEA cathodes and 2 A/cm² from Si FEA cathodes [78] in Ultra High Vacuum (UHV) in triode configurations. Nevertheless, even with optimistic FEA cathode characteristics, modelling results show that it is impossible to attain even 100 mA/cm² at these operating voltages with Mo and Si FEA cathodes operating in the plasma environment generated by a Hall or ion thruster, let alone the environment of a HCT [75].

4.2. Thermionic Emitters

Thermionic emitters provide much higher current densities than field emitting cathodes by direct or indirect heating of the cathode and subsequent emission of hot electrons which have energies sufficient to overcome the work function of the emitting surface. Various work function reducing materials are provided in the form of coatings, impregnates or as the cathode material itself to lower operating temperature and provide higher current densities at the emitter surface. Subclasses of thermionic emitters include:

1. Oxide and scandate cathodes
2. Impregnated cathodes
3. Boride cathodes.

For a set current density, the operating temperature of a specific cathode is dependant on the work function. Thermionic current density at the emitter surface is given by the Richardson-Schottky equation [79] for a given cathode surface temperature and emission constant:

$$J_{th} = A_R T_c^2 e^{\left(\frac{\phi_{eff} e}{kT_c}\right)} \quad (1.4)$$

In this approximation the Richardson constant (A_R) is set to $1.20173 \times 10^6 \text{ Am}^{-2}\text{K}^{-2}$ consistent with the theoretically obtained value:

$$A_R = \frac{4\pi m_e k^2 e}{h^3} \quad (1.5)$$

The relationship between work function and operating temperature for a set discharge current is shown in Figure 9.

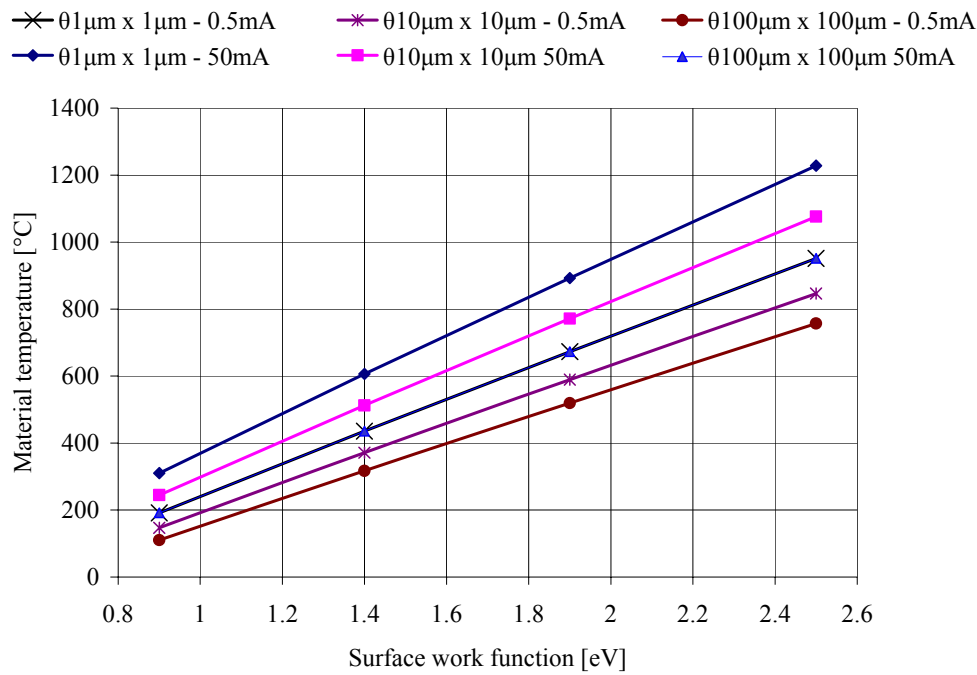


Figure 9 Relationship between operating temperature and work function for emission currents of 0.5mA and 50mA at the respective emitter geometries neglecting field enhancement.

4.2.1. Oxide Cathodes

Oxide cathodes consist of layers of various molar compositions of barium, scandium, barium oxide, calcium oxide and aluminates and generate reasonable current densities $<8\text{A}/\text{cm}^2$. Since oxide cathodes are able to produce very low work functions $<1.2\text{eV}$ they have the lowest operating temperatures of all the thermionic cathodes. However, their lifetime is particularly sensitive to ion bombardment and high voltage operation. The ion bombardment process destroys the work function reducing layer resulting in a subsequent increase in work function and shortly after, device failure. This therefore limits their use to relatively high vacuum environments similar to FEA cathodes [80]. Oxide cathodes are also particularly sensitive to poisoning due to their limited supply of work function reducing compounds.

4.2.2. Impregnated Cathodes

Impregnated cathodes are able to somewhat overcome the issues with oxide cathodes by providing a supply of work function reducing compounds from within the structure [81]. Impregnated cathodes generally consist of a porous refractory metal matrix impregnated with various molar compositions of barium-oxide, calcium-oxide and aluminates. Common cathode impregnate compositions include 5:3:2, 4:1:1 and 3:1:1, where the notation indicates the stoichiometric ratio of $\text{BaO}:\text{CaO}:\text{Al}_2\text{O}_3$ [82]. These compounds undergo thermo-chemical reactions during heated operation liberating a continuous supply to the surface. Impregnated cathodes are therefore able to operate in ion bombardment environments for reasonably long durations, continuously replenishing the emitting layer until impregnates are depleted.

It is unlikely that conventional macroscopic impregnation processes can be applied to micro dispenser cathodes since in conventional dispenser cathode manufacture upwards of 200 separate steps are required in order to produce the suitable porous structure, impregnate and then activate the emitter. This includes slurry-based osmotic infiltration processes in which the impregnate is melted and allowed to absorb into the structure requiring post process machining. In this case, thin film

coatings have been applied to the surface of micro cathodes using radio-frequency (RF) sputtering techniques for micro-thermionic generators [83]. These techniques have also shown to be able to produce an effective dispenser structure with a porous structure with sufficient ion bombardment [84]. These processes have demonstrated work functions of 2.2eV; however there is no evidence of any life tests of the process or subsequent operation in an ion bombardment environment to confirm that the process can be applied to a gas discharge device.

4.2.3. Boride Cathodes

Emitting materials such as LaB_6 and CeB_6 slowly evaporate during operation to produce the work function lowering compounds. LaB_6 has been extensively used in the Russian electric propulsion program and has demonstrated reliable operation for thousands of hours [85]. Historically, LaB_6 cathodes have required the use of a cathode heater to sustain stable operation due to their higher work function $\sim 2.6\text{eV}$. Therefore, the power required to create the same plasma current levels as lower work-function impregnated cathodes was higher. Recently, however, researchers have created LaB_6 cathodes which are able to sustain a discharge without the continual use of the heater [86] and have showed that LaB_6 cathodes can be operated at low currents [87]. Lanthanum hexaboride hollow cathodes are also two orders of magnitude less sensitive to emitter poisoning than impregnated cathodes, but require higher operating temperatures to attain similar emission current densities.

Since the work function lowering compound in LaB_6 and CeB_6 cathodes is the emitter itself, no impregnation, activation or post process machining is required during construction. As a consequence, boride emitters could possibly be directly manufactured by MEMS processes or micromachining into a boride substrate presenting significant simplification of the manufacturing problem when compared to impregnated cathodes. As a consequence, one of the design studies conducted in Part 2 considers LaB_6 as the emitter material.

5. Heater Design

A heater is necessary in the hollow cathode design to raise the emitter temperature sufficiently for the generation of energetic electrons. In conventional macro-scale devices, the heater traditionally uses refractory metals such as tungsten, molybdenum or tantalum as a resistive dissipater, typically raising the cathode temperature of the order of $\sim 1200^\circ\text{C}$. At the University of Southampton gold has been deposited around pyramidal pits etched into silicon as shown in Figure 40 producing tracks (20 μm wide, 5 μm thick) through which an electrical current is passed. This process can also be applied to the creation of heating elements on the surface of emitter structures.

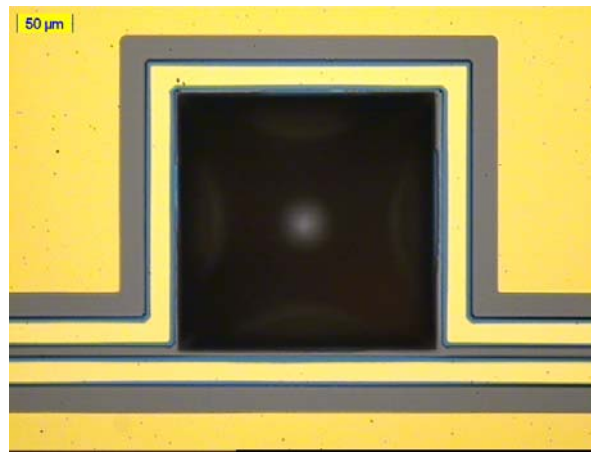


Figure 10 Pyramidal pit with a gold track on an insulating layer surrounding the opening.

With these rules in mind, there are two possible implementations of the heater circuit. Firstly, the heater and tracks can be fabricated from the same low resistivity material with the connecting tracks designed to be significantly wider than the actual heater element. Table 4 below shows the material characteristics of refractory metals typically considered in high temperature heater manufacture and other materials which have been previously deposited on MEMS devices.

Material Properties	Gold	Silicon	Tungsten	Tantalum	Molybdenum	Rhenium
Electrical resistivity 20°C [Ohm-m]	2.2×10^{-8}	1.0×10^{-4}	6.7×10^{-8}	1.3×10^{-7}	5.7×10^{-8}	1.9×10^{-7}
Electrical resistivity 1200°C [Ohm-m]	NA	NA	4.03×10^{-7}	6.30×10^{-7}	3.84×10^{-7}	8.44×10^{-7}
Thermal conductivity [W/m-K]	301	124	163	54	138	40
Emissivity	0.04	0.3-0.5	0.15	0.2	0.17	0.42
Density [g/cm ³]	19.32	2.3	19.3	16.65	10.22	21.03
Melting point [C]	1064	1412	3370	2996	2617	3180

Table 3 Material properties for heater selection [B26].

With reference to Table 8, gold would appear to be an ideal candidate for the heater element and connecting track since it has a very high thermal conductivity, yet very low emissivity and resistivity. However, its melting point temperature is at least 300°C less than that required for thermionic emission. Rhenium would also be a poor choice since it possesses a high emissivity and would thus radiate a significant proportion of the input energy. Of the remaining materials, tungsten would seem to present the most favourable characteristics based on the lowest emissivity, highest melting point and highest thermal conductivity when compared to tantalum and molybdenum.

6. Hollow Cathode Micro-Thruster Design

Exercise

The following design exercise is conducted to meet thrust requirements dictated in Section 6 including:

1. Emitter optimisation
2. Orifice optimisation
3. Anode optimisation
4. Heater optimisation.

6.1. Parametric Model

Sahli and Turchi have successfully used parametric modelling to determine bulk physical and electrical characteristics of hollow cathode operation [99,100]. Based on this work this section develops a similar parametric model in an attempt to understand the characteristics and thrust performance of a micro hollow cathode discharge.

6.1.1. Emitter Surface

The necessary mass flow rate and hence internal gas pressure to meet a thrust and specific impulse requirement based on a given orifice size is determined from equation 1.1. It is assumed that the configuration of the thruster allows for the condition of fully ionised plasma at the orifice exit which is a safe assumption at high current $\gg 63\text{A}/\text{mm}^2$ where Crofton has shown there to be a high degree of gas utilisation [29]. Conservative assumptions of electron temperatures of 0.5eV (Maxwellian) are made based on conventional cathode operation [102]. At the hollow cathode surface the dominant energy gain processes are thermal energy input by ion bombardment which deposit their ionization energy, the energy gained from falling through the sheath but also have to overcome the surface work function. Hot plasma electrons with energies sufficient to exceed the cathode fall voltage also input energy to the cathode surface, depositing their thermal energy plus the energy gained from falling through the work function. Energy is removed from the emitter surface by thermionic emission if electrons which carry with them their thermal energy (which is equal to the cathode surface temperature) and is termed convective cooling, and radiative flux. The electron or ion temperature in volts is given by:

$$\frac{kT}{e} \tag{1.51}$$

The thermal power of a convected flow is thus given by:

$$I \frac{5kT}{e} \tag{1.52}$$

This power balance at the thermionic emitter surface (only) from the particle flow described above is thus represented by:

$$\int J_{th} \left(\phi_{eff} + \frac{5kT_c}{2e} \right) dA_e = \int J_i \left(\varepsilon_i + V_f - \phi_{eff} \right) dA_e + \int J_e \left(\phi_{eff} + \frac{5kT_e}{2e} \right) dA_e - fq_r \quad (1.6)$$

With a view factor from the emitter to the cathode body:

$$f = \frac{A_e}{A_s} \quad (1.7)$$

The energy of the thermionic electrons can be approximated as a mono-energetic beam since the energy gained by acceleration through the sheath is much greater than the thermal energy, and assumes a collisionless sheath. In this analysis it is assumed that energy deposited into the cathode surfaces other than the emitter does not return to the plasma.

6.1.2. Plasma Power Balance

Electron emission provides energy to the plasma in the form of electrons accelerated by the cathode fall. This energy is utilised to ionise and excite the gas, and heat the plasma electrons. Energy is also added to the plasma by Ohmic heating of the resistive plasma within the orifice. Energy is lost by particles flowing out of the cathode, given by:

$$\int J_{th} \left(V_p + \frac{5kT_e}{2e} \right) dA_{em} + \int \frac{J_D^2}{\sigma} dV = \int J_i \left(\varepsilon_i + \frac{5kT_i}{2e} \right) dA_s + \int J_e \left(\frac{5kT_e}{2e} \right) dA_s + (I_D + \alpha I_{eq}) \left(\frac{5kT_e}{2e} \right) + \frac{I_{eq}}{\alpha} \left(\frac{5kT_e}{2e} \right) + q_r \quad (1.8)$$

Where equivalent flow rate is defined by:

$$I_{eq} = \frac{e\dot{m}}{m_i} \quad (1.9)$$

A similar energy balance has been used successfully in [99].

If the configuration of the thruster allows for the condition of fully ionised plasma (where $\alpha = 1$) at the orifice exit then the energy balance can be expressed as:

$$I_{th} \left(V_p + \frac{5kT_e}{2e} \right) + \int \frac{I_D^2}{\sigma} dV_{oh} = I_i \left(\varepsilon_i + \frac{5kT_i}{2e} \right) + I_e \left(\frac{5kT_e}{2e} \right) + (I_D + I_{eq}) \left(\frac{5kT_e}{2e} \right) + I_{eq} \left(\frac{5kT_i}{2e} \right) + q_r \quad (1.10)$$

This assumes Ohmic heating of the plasma volume within the emitter is small compared to the orifice since emitter diameter \gg orifice diameter.

6.2. Insert Processes

6.2.1. Emitter

Thermionic current density at the emitter surface is given by the Richardson-Schottky equation [79] for a given cathode surface temperature and emission constant:

$$J_{th} = A_R T_c^2 e^{\left(\frac{\phi_{eff}}{kT_c}\right)} \quad (1.11)$$

Thermionic electron emission from the cathode occurs primarily at the downstream end due to the higher plasma potential and fall voltages, resulting in greater ion heating and enhanced emission. The plasma column induces sheath-enhanced emission at the emitter surface due to the intense field ($\sim 10^7$ V/m) between the plasma column and cathode potentials at a distance on the order of the Debye length. The effective work function in terms of the electric field at the cathode surface is given by:

$$\phi_{eff} = \phi - \sqrt{\frac{e - |E_c|}{4\pi\epsilon_0}} \quad (1.12)$$

It is assumed that no significant amounts of secondary emission contribute to the main discharge current [88]. The strength of the enhancing electric field can be estimated from the double-sheathed analysis at the cathode surface governed by Poisson's equation. An approximation to the double sheath analysis was developed by Siegfried and Wilbur [89]:

$$E_c = \sqrt{\frac{n_e k T_e}{\epsilon_0} \left(\left[2 \sqrt{1 + 2 \frac{e V_p}{k T_e}} - 4 \right]^{0.5} \right)^{0.5}} \quad (1.13)$$

The fall voltage is considered across a non-neutral, collisionless region between the cathode surface and the plasma. In this analysis the cathode potential drop is assumed to be approximately 8-10V above the cathode potential, consistent with experiment, with other parameters, particularly Ohmic heating, constituting energy continuity. This is consistent with the energy required for the excitation of meta-stable states of xenon (3P0 \sim 9.45eV, 3P2 \sim 8.32eV) which will remain consistent at micro scale [28] as discussed in Section 1. Ion production is generally assumed to be achieved by multi-step processes firstly by electron impact of primary electrons from the atomic ground state within the emitter volume, and then by lower energy thermalized electrons.

The ion flux density to the cathode surface is due to random thermal flux in the bulk plasma. This ion current density is assumed to be uniform within the emitter cavity and within the orifice and equal to the Bohm current.[101]:

$$J_i = en_i \left(\frac{kT_i}{2\pi m_i} \right)^{1/2} \quad (1.14)$$

Ions enter the sheaths at the Bohm velocity and diffuse downstream at the thermal velocity. The finite Bohm velocity implies the existence of a pre-sheath field and density gradient: a weak electric field penetrating into the plasma near the sheath edge, which accelerates the ions as they enter the

main sheath. The potential change in the pre-sheath region is on the order of kT_i , equal to the thermal energy of the electrons/ions.

6.2.2. Plasma Electrons

Energy balance is a result of resistive heat input into the orifice, and electrons accelerated through the sheath potential. As the discharge current is increased, resistive heating scales quadratically, however this heating alters the plasma parameters and thus the resistivity. In this case resistive heating should be maximised for power deposition within the plasma while maintaining low voltages and powers. Energetic plasma electrons contribute an electron back-current. Plasma electrons are assumed to have a Maxwellian distribution with only electrons having energies higher than the fall voltage able to reach the cathode surface. The plasma electron flux to the cathode emitter and orifice can be expressed as [99]:

$$J_e = en_e \left(\frac{kT_e}{2\pi m_e} \right)^{1/2} e^{\left(\frac{-eV_f}{kT_e} \right)} \quad (1.15)$$

6.3. Orifice Processes

Ionisation, radiative and resistive processes within the constricted orifice of hollow cathodes have a strong influence on operating parameters and the transition point from spot to plume mode [90]. Katz presented a model of the ionisation and energy balance in the orifice of a hollow cathode treating the orifice as a homogeneous region with a thin wall sheath [91]. In this section an analysis of cathode performance parameters will define acceptable dimensions of the orifice and keeper based on a similar energy balance and to meet thrust requirements as described in Section 5.

Within the orifice, resistive dissipation is balanced by energy loss from the plasma by ion production, (which is balanced by the ion losses from orifice boundaries), excited atom flux, electron convective cooling and radiation. The Ohmic drop over the orifice may be estimated from classical resistivity ignoring the self-induced magnetic field:

$$\Delta V_{oh} = \frac{J_e L_{or}}{\sigma} \quad (1.16)$$

Where:

$$J_e = \frac{I_d}{A_0} \quad (1.17)$$

Energy removed from the cathode at the orifice exit is given by:

$$P_{loss} = P_{ion} + P_{rad} + P_{conv} \quad (1.18)$$

This assumes negligible secondary ionisation given the high secondary ionisation potential of xenon (33.2eV) and that the ion production rate equals the ion loss rate.

$$\frac{dn_i}{dt} = 0 = \left(\frac{dn_i}{dt} \right)_{ionization} + \left(\frac{dn_i}{dt} \right)_{in} - \left(\frac{dn_i}{dt} \right)_{out} \quad (1.19)$$

In this operating regime, it is assumed that the orifice is both long enough and of sufficiently small diameter to allow full utilisation of the gas with Ohmic dissipation directly heating the heavy particles. Assuming negligible radiative losses and each particle has 5 degrees of freedom yields an expression for the power loss by particle efflux and ion recombination within the orifice as [102]:

$$P_{loss} = J_i \varepsilon_i \pi r (r + 2l) \left(\frac{5kT_i}{2e} \right) + I_D \left(\frac{5kT_e}{2e} \right) \quad (1.20)$$

Power loss can then be equated to resistive dissipation within the orifice for the power balance:

$$P_{loss} = I_D^2 R \quad (1.21)$$

Given the narrow orifice, the ion density at the outlet can be found by assuming the drift velocity is equal to the thermal random velocity in the direction of the outlet with net flux equal to the propellant flow rate. At the outlet where a sudden change in plasma density is expected, this can serve as a first approximation [92].

$$n_i = \frac{\dot{m}}{A_0 e} \left(\frac{eT_i}{2\pi m_i} \right)^{-1/2} \quad (1.22)$$

Since the work function of the orifice is much higher than the emitter work function ($\sim 2.5\text{eV}$) it is assumed that thermionic emission from the orifice is negligible and does not contribute to the discharge current.

Orifice resistance is approximated to that of a fully ionised gas due to the high degree of ionisation. Spitzer and Harm have solved this problem for fully ionised plasmas by means of numerical integration [93]. The conductivity of fully ionised plasma is considered to be independent of the ion density. Conductivity of the plasma based on electron-electron collisions is given by:

$$\sigma = \frac{1.53 \times 10^{-2}}{\log \Lambda} T_e^{3/2} \quad (1.23)$$

Where the plasma parameter, Λ , is given by:

$$\Lambda = 4\pi n \lambda_d^3 \quad (1.24)$$

This dimensionless parameter is equal to the typical number of particles contained in a Debye sphere. Considering that the Debye length is given by:

$$\lambda_d = \sqrt{\frac{\varepsilon_0 k T_e}{n e^2}} \quad (1.25)$$

and that the average distance between particles is given by:

$$r_d \equiv n_e^{-1/3} \quad (1.26)$$

and further, that the distance at which the coulomb energy of one charged particle in its electrostatic field is zero is given by:

$$r_c \equiv \frac{e^2}{4\pi\epsilon_0 T_e} \quad (1.27)$$

Then these equations can then be combined to give a solution for the plasma parameter:

$$\Lambda = \frac{1}{4\pi} \left(\frac{r_d}{r_c} \right)^{3/2} = \frac{4\pi\epsilon_0^{3/2} T_e^{3/2}}{e^3 n_e^{1/2}} \quad (1.28)$$

From which it follows that:

$$\Lambda = 1.24 \times 10^{-7} \left(\frac{T_e^3}{n_e} \right)^{1/2} \quad (1.29)$$

The conductivity of the plasma can then be solved for the conditions found in the orifice under the assumption that the Debye length is much smaller than the orifice diameter. This is a safe assumption given the high internal gas pressure thus plasma density required to give sufficient flow rate at the sonic speed as shown in the results of the parametric model in Section 7.2. The bulk of the ion are thus free of the strong electric field near the wall.

$$\frac{\lambda_d}{d_o} \ll 1 \quad (1.30)$$

6.4. Discharge Parameters

The total discharge current from surfaces at cathode potential is based on the contributions of all particle fluxes at for preservation of current continuity. This consists of the emitted thermionic current, ion recombination and an electron back current expressed as:

$$I_D = I_{th} + I_i - I_e \quad (1.31)$$

To relate the operating power to the discharge current all potential drops between the cathode and the anode should be calculated. The total discharge voltage can be expressed as:

$$V_d = V_p + V_{oh} \quad (1.32)$$

This is the sum of the cathode fall voltage (plasma potential drop at the emitter surface) and the Ohmic drop across the orifice. The Ohmic drop across the orifice is as calculated previously.

This section contains a mixture of gas dynamics and plasma processes. The treatment of such an analysis thus is inherently limited and may only serve as a first approximation. The degree of rarefaction is given by the Knudsen number:

$$Kn = \frac{\lambda}{L} \quad (1.35)$$

The characteristic flow dimension is the expansion slot width (orifice diameter) in this case. Free molecule conditions are defined by $Kn \gg 1$ where either the mean free path is very large or the characteristic dimension is very small. Knudsen number range between 0.1 and 1.0 and represents a transition regime where the inviscid flow analysis that follows is expected to only be approximate. The flow field within the cathode orifice is complex and is not easily understood in the context of classical nozzle analysis [95]. In these, the Reynolds number (Re) is used to evaluate the relative importance of viscous effects at the orifice expansion. This is given by the equation:

$$Re = \frac{\rho VL}{\mu(T)} \quad (1.36)$$

Due to the potentially large flow field gradients and small physical dimensions in the orifice, it is difficult to choose a characteristic body dimension and to assign appropriate values for the density and viscosity. If an average density is assumed, then equation (1.36) can be rewritten as:

$$Re = \frac{4\dot{m}}{\pi L \mu(T)} \quad (1.37)$$

It would be expected that viscous losses would increase with decreasing Re but the exact dependence is sensitive to specific characteristics of the thruster such as geometry. Eq. (1.37) also indicates that Re decreases with decreasing mass flow rate if both the characteristic body dimension and the viscosity remain fairly constant, since the dependence of these variables on the mass flow rate in the arc is unknown in terms of the flow field characteristics.

Assuming a uniform velocity profile across the orifice, thrust generated as a result of pressure and momentum thrust is given by Equation 1.1, where, assuming that all particles behave like a perfect dilute gas and neglecting magnetic pinch effects, the plasma pressure in the hollow cathode orifice can be evaluated from the equation of state:

$$p_{or} = n_e kT_e + n_i kT_i + n_n kT_n \quad (1.38)$$

Considering the small orifice area compared to the cross sectional area of the internal diameter of the cathode, the internal pressure may, as a first approximation, be estimated from the critical flow relation for sonic flow through the orifice assumed to be adiabatic.

$$p_{ins} = p_{or} \left(1 + \frac{\gamma - 1}{2} \right)^{-1/(\gamma - 1)} \quad (1.39)$$

6.5. Energy Conservation

At the insert surface, the energy loss due to convected thermionic electrons is balanced primarily by ion bombardment. If energy input due to plasma electrons overcoming the fall voltage is neglected (since the fall voltage is much greater than most of the electron energies for a Maxwellian distribution) the energy balance can be expressed as:

$$\int J_{th} \left(\phi_{eff} + \frac{5kT_c}{2e} \right) dA_e = \int J_i (\varepsilon_i + V_f - \phi_{eff}) dA_e \quad (1.40)$$

This then allows the calculation of the required emitter temperature based on the contribution of all particle fluxes to the surface. The Richardson coefficient is set to a moderate value for S-type impregnated porous tungsten dispensers of 120 [27]. The approximate working temperature of a given emitter can be found based on the fall voltage, particle densities and emitter geometry assuming the full length of the emitter is responsible for thermionic emission. In reality emitter temperature increases at the downstream end of the cathode due to increasing plasma potential and plasma density however in this case we can use uniform temperature as a first approximation of working temperature.

From Equation (1.39) the insert pressure can also be considered as a contribution of all particle fluxes to an equation of state (1.38). The ion number density necessary to balance convective energy loss can be determined by assuming ions traverse the thin sheath at the cathode surface at the Bohm velocity as given by Equation (1.14). Conservative assumptions of electron temperatures of 0.5eV (Maxwellian) [102] are made within the internal volume considering a quasi-neutral plasma where:

$$n_i = n_e = n \quad (1.41)$$

Within the internal emitter volume, the ion temperature is assumed to be at thermal equilibrium with the emitter wall temperature ~0.1eV given the high gas pressures (>1bar) and low degree of resistive heating in comparison to the orifice due to the relative cross sections.

6.6. Anode Cooling

Heat is deposited in the anode primarily by electron convection and ion bombardment. The primary anode heating mechanism is convective heat transfer from the emitter to the anode by the discharge current and ion flux (where ion flux is primarily within the orifice due to the high plasma density). The thermal power flux of ions and electrons is given by equations 1.52 and 1.8. The emissivity dependant radiative power of a body is given by Stefans Law:

$$P = A \varepsilon [T] \sigma T^4$$

To avoid anode overheating, the necessary anode area required for a given heat input to maintain a given temperature is given by:

$$A_a = \frac{I_{i-A} \left(\varepsilon_i + \frac{5kT_i}{2e} \right) + I_D \left(\frac{5kT_e}{2e} \right)}{\varepsilon_A [T] \sigma T_A^4} \quad (1.43)$$

This assumes the anode is only cooled radiatively which will serve as a conservative assumption since in reality heat will also be conducted away from the device to the supporting housing and spacecraft structure.

6.7. Preheating Energy Balance

Assuming that a tungsten heating element has the dimensions described in Part 2, and that the cathode whilst preheating is at a constant temperature equal to the necessary ignition temperature, heater resistance is given by:

$$R_h = \frac{\rho_h [T_h] L_h}{A_h} \quad (1.44)$$

Assuming negligible conductive heat transfer from the wafer the energy balance between the heater input power and power radiated by the cathode is given by:

$$I_h^2 R_h = A_c \varepsilon_c [T] \sigma T_c^4 \quad (1.45)$$

This assumes the cathode is only radiative cooled which is fair given that conductive cooling should be minimised in the final design by thermally isolating the device. The radiative area is given by the necessary dimensions for heat dissipation during operation from Eqn.1.43. The heater operating voltage is then given by:

$$V_h = I_h R_h \quad (1.46)$$

For application to small satellites is necessary to base heater design for operation from a 24V bus able to provide current regulation.

6.8. Lifetime Estimation

Experimental sputter yield data of molybdenum, a material preferred for traditional cathode orifice plates, is shown in Figure 11.

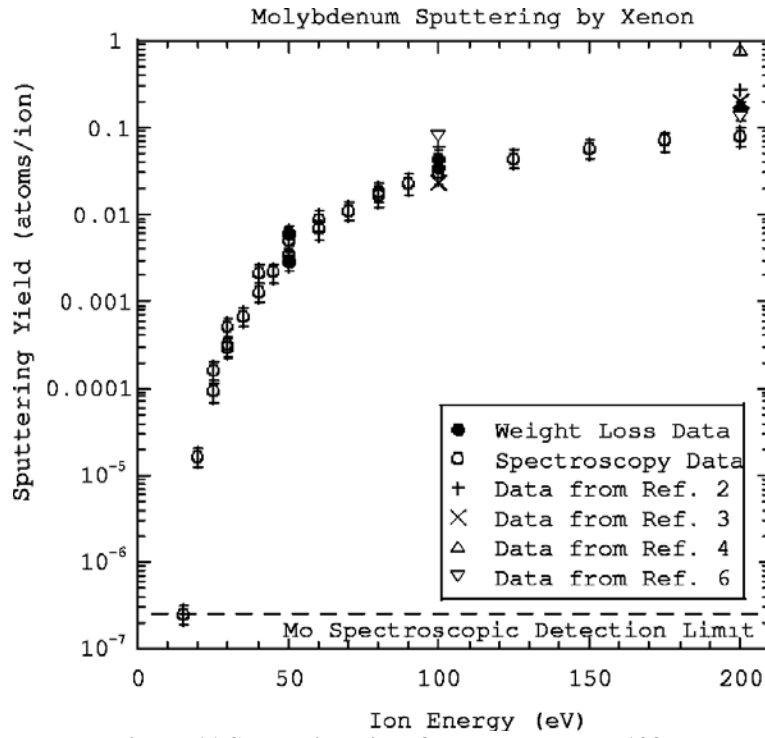


Figure 11 Sputtering yield for molybdenum [103]

Since the plasma density is highest in the cathode orifice an estimation of the time taken to enlarge the orifice can be made based on the initial orifice diameter, ion flux and sputter yield data. The ion current density contacting the orifice can be found from Equation 1.1.4. Assuming a lifetime limit as a 2% change in orifice diameter the total mass loss is given by:

$$\Delta m_{or} = \rho_{mo} \pi \left((1.02 d_{or})^2 - d_{or}^2 \right) L_{or}$$

Given the small change in orifice diameter, the increase in ion flux to the orifice wall is considered negligible. The mass loss rate of orifice material is given by:

$$\dot{m}_{or} = \frac{J_i \pi d_{or} L_{or} Sp[V_d] M_{mo}}{e}$$

The life of the cathode is then given by:

$$\frac{\Delta m_{or}}{\dot{m}_{or}}$$

6.9. Design Iteration 1

The model was iterated firstly in an attempt to quantify the necessary geometrical parameters, operating conditions and performance of a single channel HCMT. The required output parameters from the model were a heavy particle temperature of 2,000K which generates a specific impulse of 155s with a xenon plasma with the inclusion of the plasma pressure component, and a total thrust level of 0.11mN presenting a relatively demanding thrust requirement. The initial aim was to determine the sensitivity of cathode geometry in terms of both efficiency and terminal parameters. An arbitrary cathode of orifice length 50µm was selected and the model was used to predict

operating parameters for aspect ratios (cathode diameter/length) of 0.25 to 2. Figure 12 shows the relative effect of orifice aspect ratio.

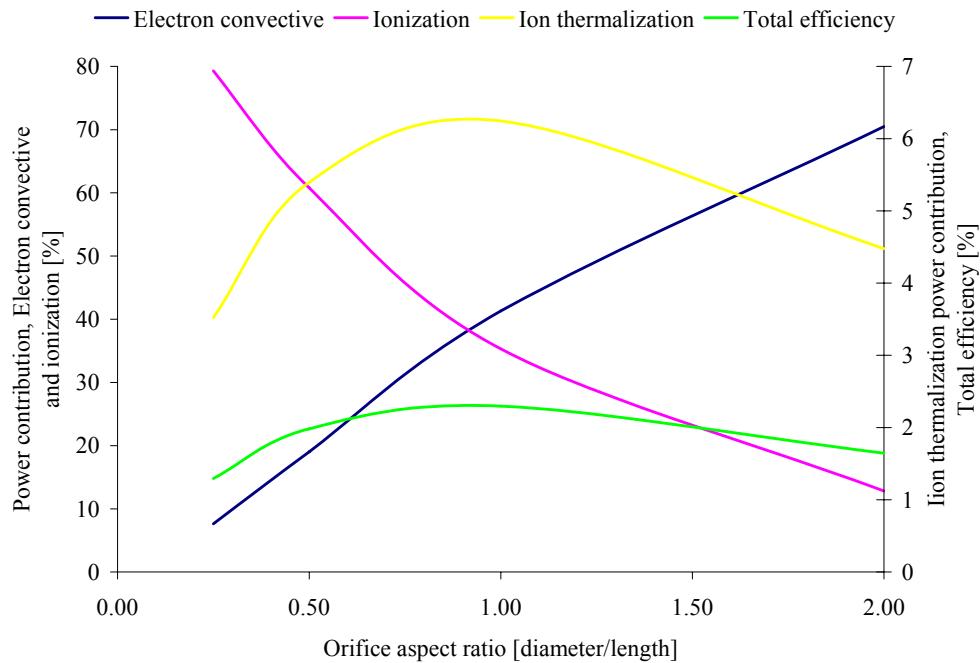


Figure 12 Relative power contributions

Increasing aspect ratio initially leads to an increase in thrust efficiency up to a maximum of 2.3% after which efficiency begins to decrease. Maximum thrust efficiency is found at the point where the dominant loss mechanisms of electron convective power loss and ionisation losses are equal and losses are essentially minimal for a given performance. Increasing aspect ratio further leads to increased ionization losses due to recombination with the orifice walls with a less significant electron convective power loss saving. Figure 13 shows the influence of orifice aspect ratio on the required operating current and orifice current density.

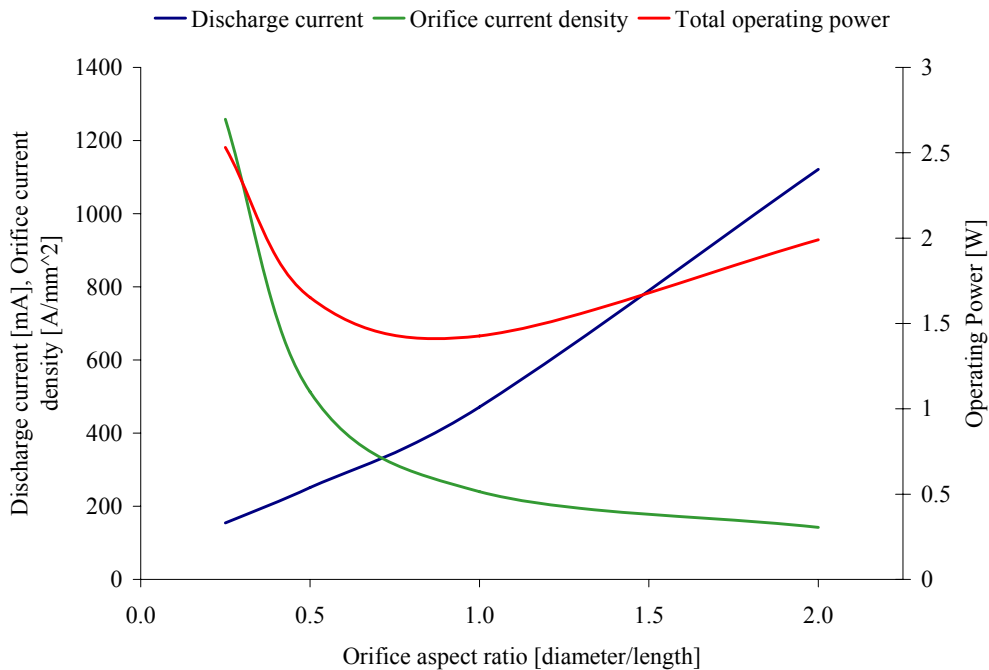


Figure 13 Current density and operating power relative to aspect ratio

Discharge current is reduced significantly with decreasing orifice diameter (smaller aspect ratios) which is shown as increased efficiency and lower power operation, however this incurs a penalty in terms of increasing orifice current density. Orifice current densities have been the primary determining factor in establishing empirically derived lifetimes. Operation at orifice plate temperatures below 1300°C and below 13A/mm² has typically been used in development of low power low flow 3.2mm cathodes consistent with practices proven to enable lifetimes greater than 10,000 hr [32]. The T5 cathode was originally designed for the main discharge cathode in the UK-10 ion engine and has been extensively characterised [96] operating with orifice current densities of up to 65A/mm². The minimum power requirement shown above however requires orifice current densities ~ 250A/mm² with 2% thrust efficiency while operating at an aspect ratio of 2 requires a current density of 148 A/mm² at 1.64% thrust efficiency.

Figure 14 shows the influence of aspect ratio on operating pressure. For constant mass flow with decreasing orifice diameter upstream pressure must increase significantly leading to operation > 2bar at diameters <12.5µm. Critically, in order to maintain the hollow cathode effect by sustaining a pressure-emitter cavity diameter product ~ 10torr-cm, emitter diameter increases dramatically with aspect ratio. In this case to maintain an emitter diameter <190µm for this particular case requires aspect ratios no greater than 0.5 giving an operating pressure of 0.69bar. This is of course related to the decreasing pressure of operation due to a larger orifice. At smaller orifice diameters upstream pressure must increase significantly to maintain the necessary mass flow rate to meet thrust requirements as the flow speed through the orifice cannot exceed mach 1. One realization is therefore that crucial to the miniaturization of hollow cathode emitters is operation at elevated pressures. Operation at very high pressures does of course bring complications in the propulsion system design since this represents the minimum propellant tank pressure limit at which the cathode can function at the operating conditions for which it was designed. In the case of very high pressure operation this therefore could present a significant propellant utilization problem. On the other hand smaller orifices are more efficient since discharge current and electron convective losses are significantly reduced.

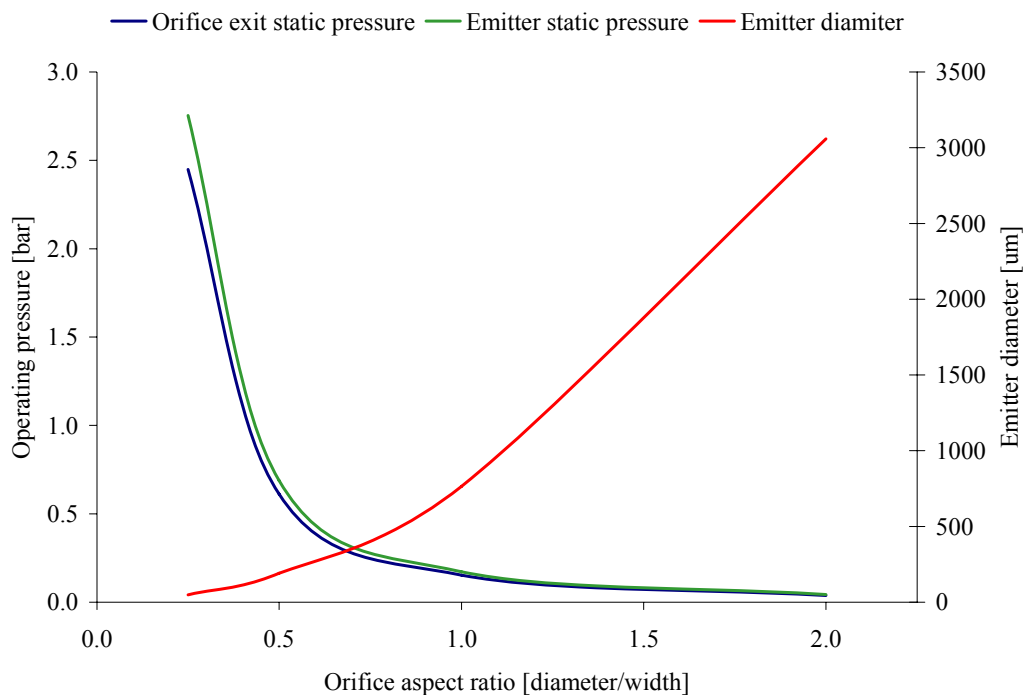


Figure 14 Operating pressure and emitter diameter relative to orifice aspect ratio

Figure 15 shows the required chip size based on cooling requirement at 800°C and 1000°C depending on the maximum operating temperature of the device. Also shown is the required

preheating power requirement based on the respective chip sizes. More inefficient aspect ratios which either result in excessive ion or convective losses also drive up the minimum chip size required for cooling and thus the preheating peak power requirement. It is also noted that the preheating power requirement is up to 4 times greater than the steady state power requirement due to the fact that the device must be heated to 1200°C, significantly higher than the normal operating temperature. More inefficient device designs therefore drive up the peak power requirement at preheating prior to ignition.

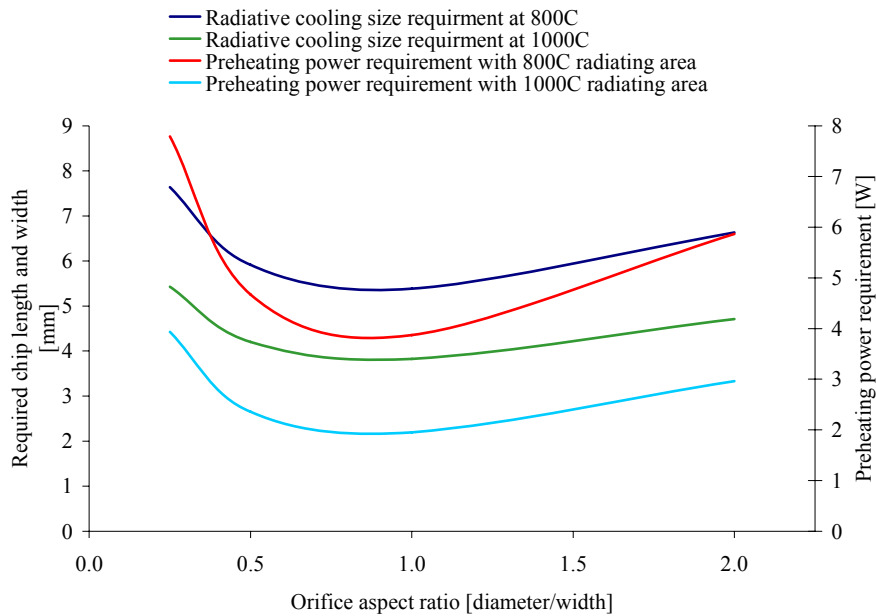


Figure 15 Required chip dimensions for adequate cooling at 800C and 1000C relative to orifice aspect ratio

Figure 15 also shows the influence of aspect ratio on emitter diameter and operating temperature. For preservation of the hollow cathode effect emitter diameter must be increased to give the empirically derived pressure-diameter product of ~ 10 torr-cm. In this case, as orifice size is increased the upstream pressure decreases and emitter diameter is increased inversely. In this case an aspect ratio of >1 results in an emitter diameter $>300\mu\text{m}$ and quickly approaches the scale of the chip size required for cooling. The emitter temperature is evaluated based on the effective work function due to field-enhanced emission (primarily a function of the operating pressure), the required discharge current and available emitter area. Emitter length was set to 10-times the emitter diameter as consistent with the T5 and T6 hollow cathode emitters and maintaining reasonable emitter dimensions.

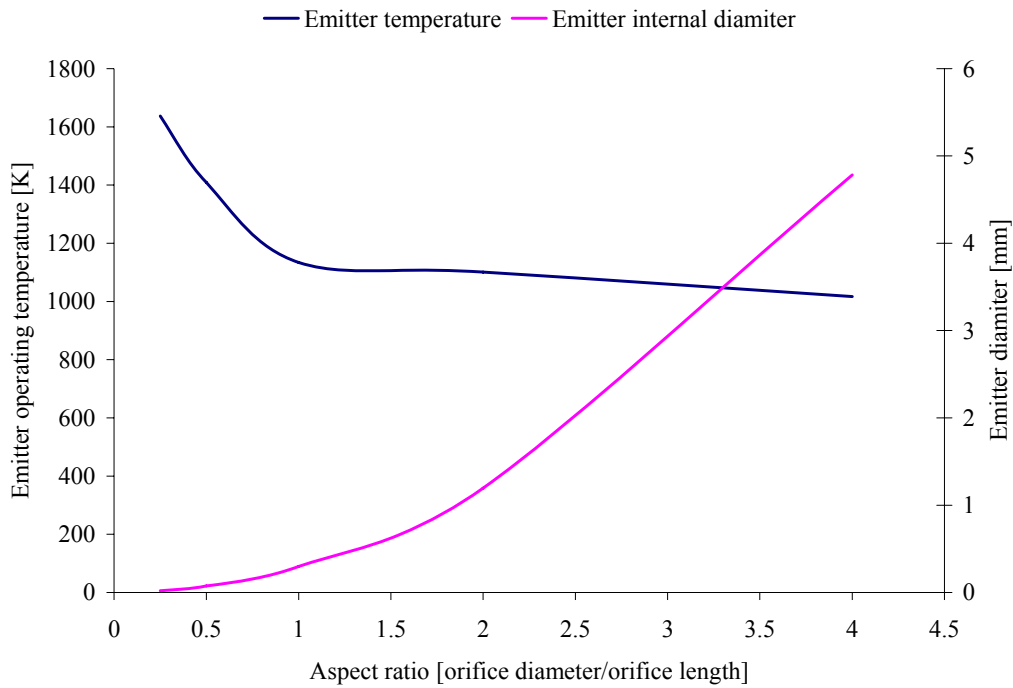


Figure 16 Emitter operating temperature and diameter relative to orifice aspect ratio

As aspect ratio is decreased from 0.25 to 1 emitter operating temperature is reduced by 502K due to the greatly decreased current demand but also due to the increase in available emitter area. In this case available emitter area follows a cubic relationship with operating pressure and thus orifice diameter. Further increase in aspect ratio does not yield much greater reduction in operating temperature due to the reduction in electric field strength at the emitter surface and exponential influence of effective work function on emitted current density. LaB₆ cathodes have traditionally operated at this temperature and thus it is anticipated that thermal desorption of LaB₆ would not present a life limiting mechanism in this case. The influence of aspect ratio on effective work function and electric field strength at the emitter surface is shown in Figure 17.

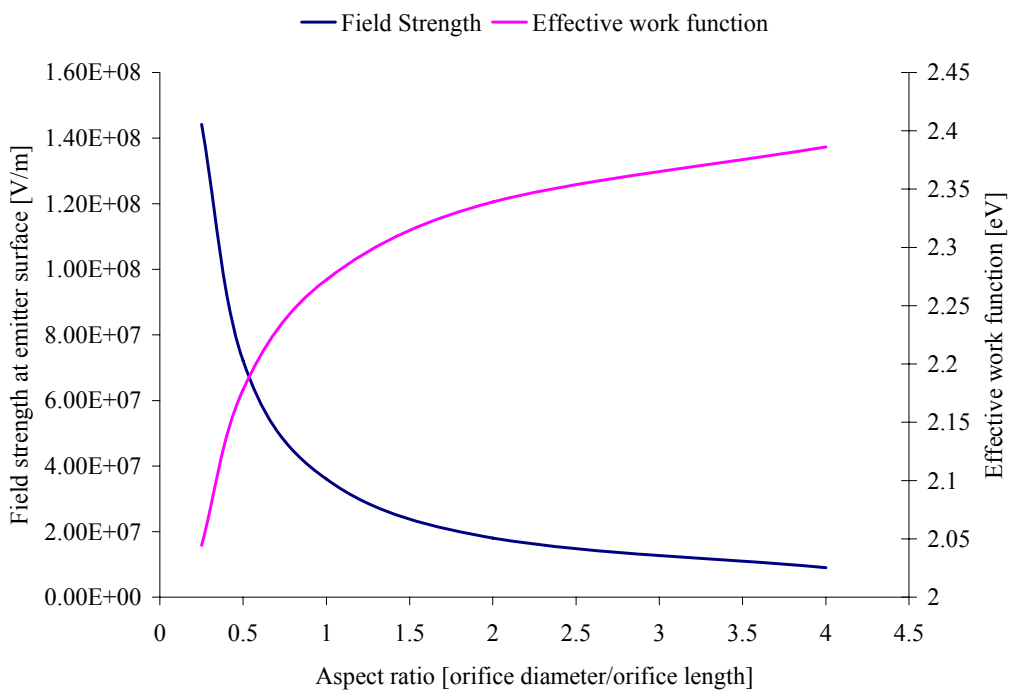


Figure 17 Electric field strength and effective work function relative to orifice aspect ratio

Figure 18 shows the time taken for the orifice of each cathode at the respective aspect ratio to increase its diameter by 10% due to ion erosion at a range of incident ion energies. This assumes that there is no redeposition of material to the orifice walls and that there is no increase in exposed surface area throughout the erosion process. In reality, a roughening of the surface and thus an increased in surface area is known to increase sputter yield.

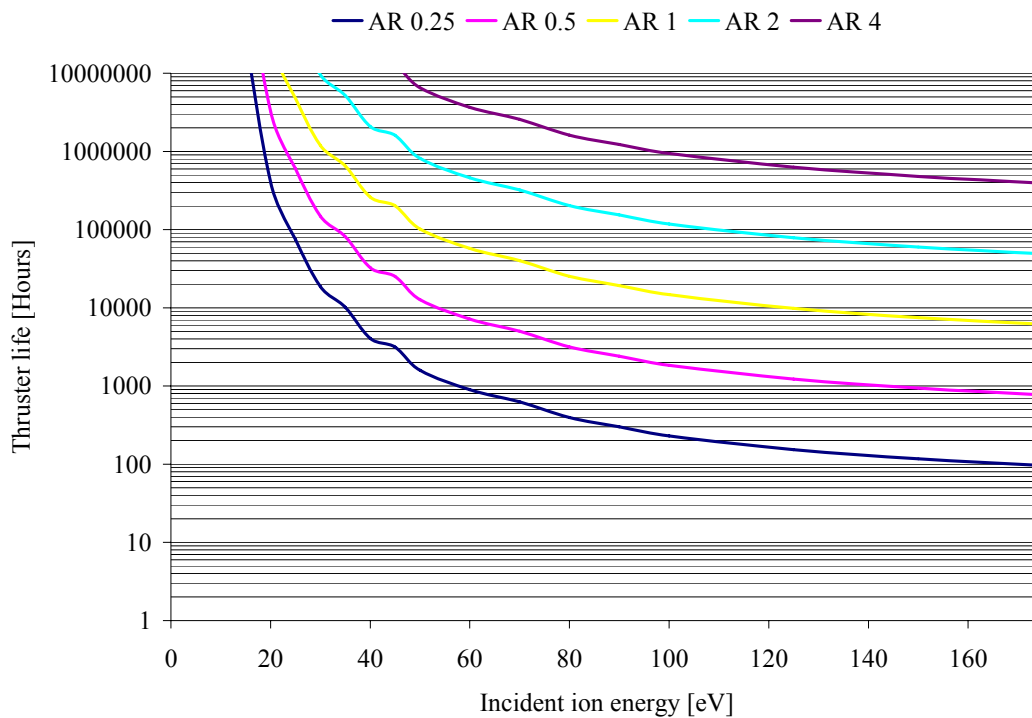


Figure 18 Time for orifice diameter to reach 98% of its initial value with respect to incident ion energy for various aspect ratios [95]

There are no direct measurements of ion energies within the interior of a cathode, however measurements downstream have detected ions well in excess of the discharge voltage as stated earlier. In our case the discharge voltage for all aspect ratios does not exceed 72V and it is expected that the emitter will not experience ions significantly above the discharge potential. In any case it can be seen that based on available data for low energy sputtering of molybdenum by xenon lifetimes of hundreds of hours are achieved even for the smaller orifice (12.5 μ m). Larger orifices show greatly increased lifetimes due to the lower pressure operation and decreased ion current density at the orifice walls from greater volume to surface area ratios.

This first design iteration has shown the relative influence of orifice geometry in driving emitter geometry, thruster chip size, preheating power and performance. It has shown that for maximum efficiency ionization losses should be equal to electron convective losses, which for an orifice length of 50 μ m demands a specific aspect ratio close to 1. The design has also shown that even when efficiency is maximized the useful transfer of thermal energy to the propellant is no greater than 6% and frozen flow losses reduce the propulsive efficiency to no greater than 2%. Even in this case, the orifice current density is still at least 4 times greater than in the T5 hollow cathode at maximum rated current. Attempting to reduce current density by increasing orifice length results in decreasing efficiency as ion recombination losses become the dominant loss mechanism in with respect to electron convective losses. At this scale, the fundamental limitation is ion losses due to the volume/surface area dilemma in the cathode orifice. The volume-area ratio for a cathode with an aspect ratio of 1 scales with:

$$\frac{2r_{or}}{r_{or}^2}$$

A cathode with a 100 μm orifice therefore has a volume to a area ratio 10 times greater than that of a 10 μm orifice. The implication of this is a greater proportion of ions are lost to the walls of smaller orifices however this has to be traded off with the reduced electron convective losses from the lower discharge currents required, hence maximum efficiency is achieved when both ion and electron convective losses are equal. This represents a fundamental dilemma in this current design of device.

6.10. Design Iteration 2

Figure 19 shows the discharge parameters of a cathode with 25 μm and orifice length from 25 μm -100 μm . It can be seen that the smaller cathode orifice show a small improvement in efficiency due to reduced current requirement, however even by including orifice lengths up to 100 μm , this configuration is still unable to significantly reduce orifice current densities, which remain between 5-6 times the orifice current densities of traditional cathodes.

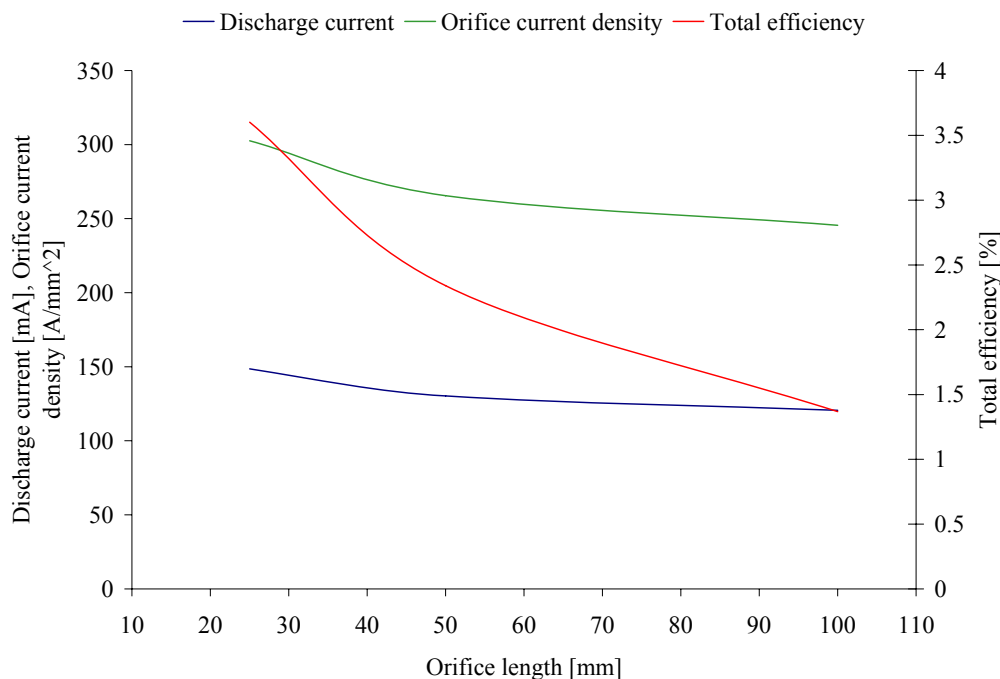


Figure 19 Discharge current and total efficiency with respect to orifice length

Further reduction in orifice diameter <25 μm results in excessive backpressure >1.7bar and may substantially decrease propellant utilization efficiency at the end of life. A proposed design solution is to reduce the tendency of ions to recombine on the cathode orifice is to form the orifice as part of the anode itself. In this way ion recombination with the orifice walls can be prevented by repulsion at the edge of the positive sheath forming the virtual anode which collects electrons from the plasma. The process of drawing the current through the length of the orifice will still result in resistive dissipation similar to a conventional orifice however without the high ion recombination losses found in the previous design. In this case a proportion of the discharge current will be collected as it passes through the orifice however in this simple analysis we assume that the orifice wall area is small in comparison to the anode collection area available downstream of the orifice thus the current collected within the orifice itself is negligible. A representation of this configuration is shown in Figure 20.

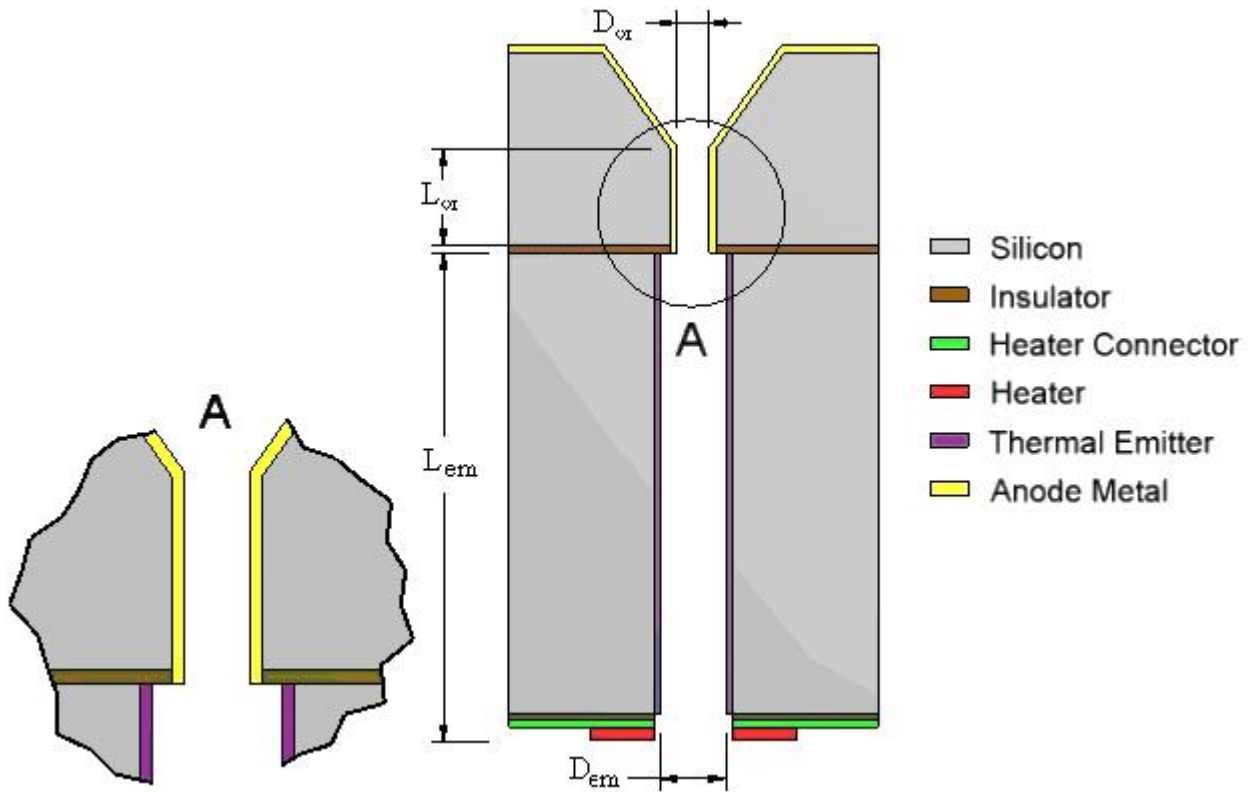


Figure 20 Representation of the +Ve orifice hollow cathode

Figure 21 shows the resulting discharge parameters with both the orifice at cathode potential (designated -Ve) and anode potential (designated +Ve) with a fixed orifice diameter of 25μm and varying orifice length.

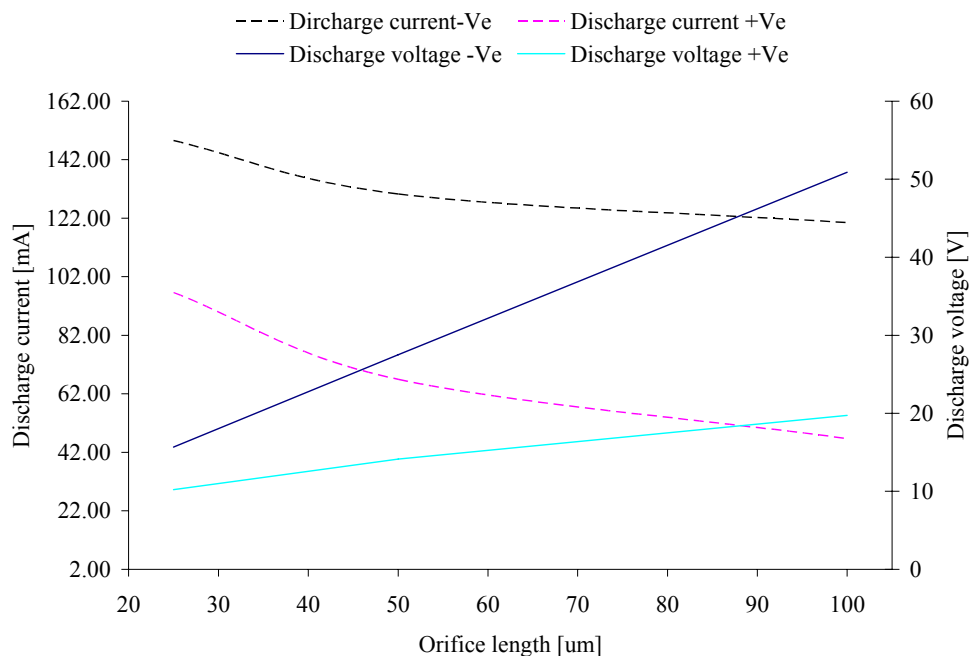


Figure 21 Discharge parameters with respect to orifice length

The cathode at +Ve orifice potential shows a dramatic reduction in the required discharge current and resulting discharge voltage in comparison to the cathode with an orifice at -Ve potential. This is owed to the large reduction in ion recombination losses at the orifice wall and therefore the reduced energy input requirement for maintained ionization fraction. Although the current

requirement is reduced however the orifice resistivity remains constant for each orifice length thus the corresponding discharge voltage is also significantly reduced. Figures 22 and 23 illustrate the power requirement and efficiency for each design.

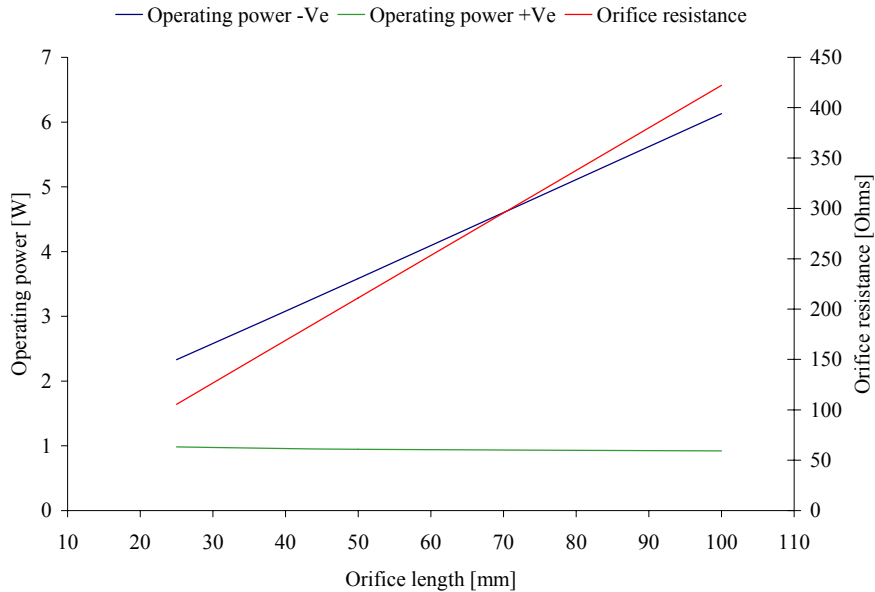


Figure 22 Operating power and orifice resistance with respect to orifice length

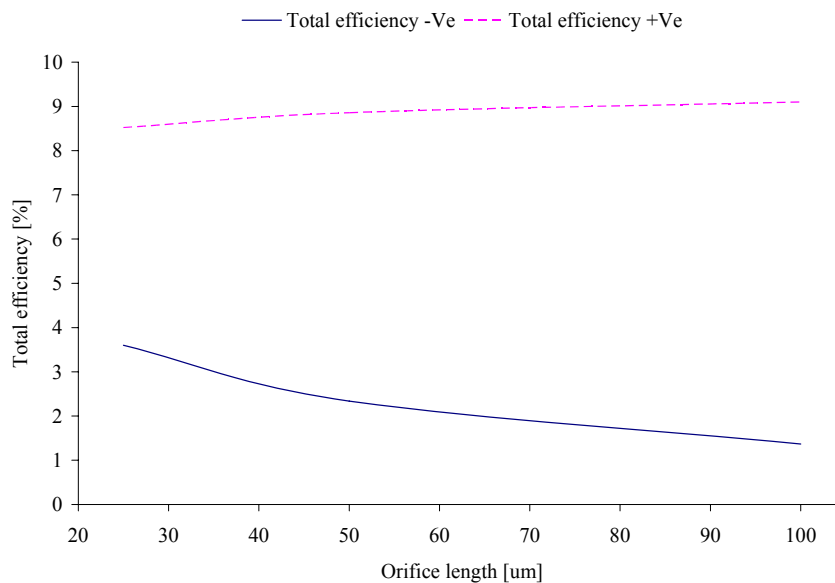


Figure 23 Thrust efficiency of both the +Ve and -Ve hollow cathode with respect to orifice length

The +Ve orifice cathode shows increasing efficiency with orifice length tending towards an asymptote. This is a result of the dominant loss mechanisms become heavy particle thermalization and ionization losses rather than electron convective losses. In a 100um orifice for example, electron convective losses represent only 6.3 % of the total operating power while thermal energy addition to ions and electrons represents 25% of the power invested. The remaining 68.7% of the operating power is invested in ionization of the flow. In this scenario 9-10% represents a practical upper limit of the efficiency achievable for a fully ionized flow at 2000K. Propulsive efficiency can however increase further by operating at lower temperature however the assumption of a fully ionized flow may not be justified at such low specific powers.

Figure 24 shows the required chip length based on a square design to meet radiative area requirement for both types of device at 800°C and 1000°C. Reduced losses generate much more compact chip dimensions owed to the reduced radiative cooling requirement. Furthermore the reduced chip size reduced so does the peak preheating power requirement for ignition of the device as shown in Figure 25.

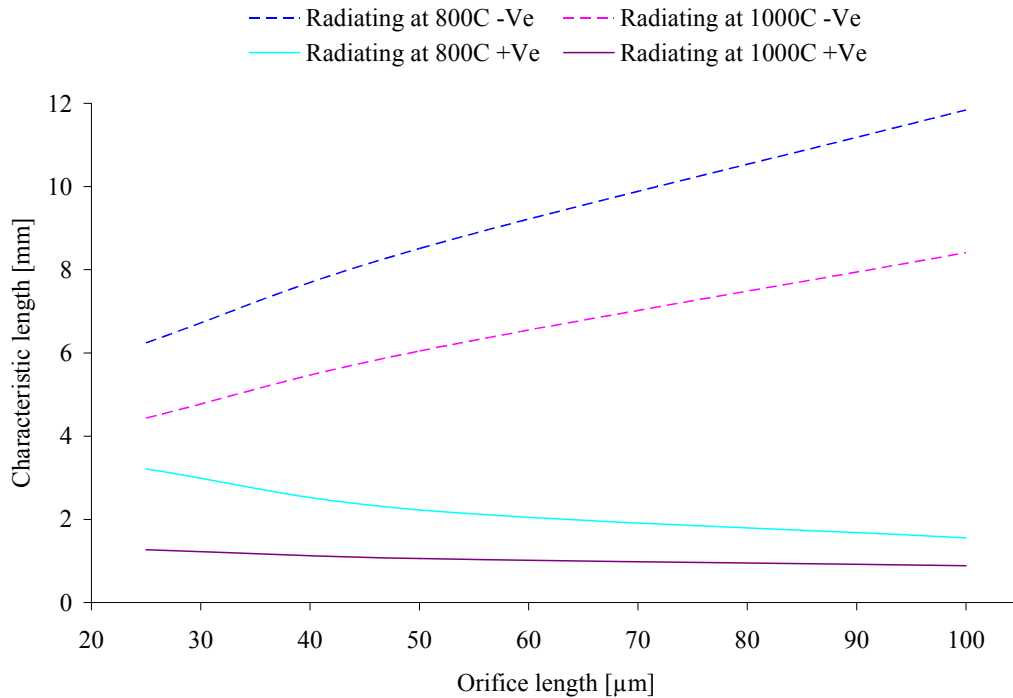


Figure 24 Required chip size for radiative cooling requirement with respect to orifice length

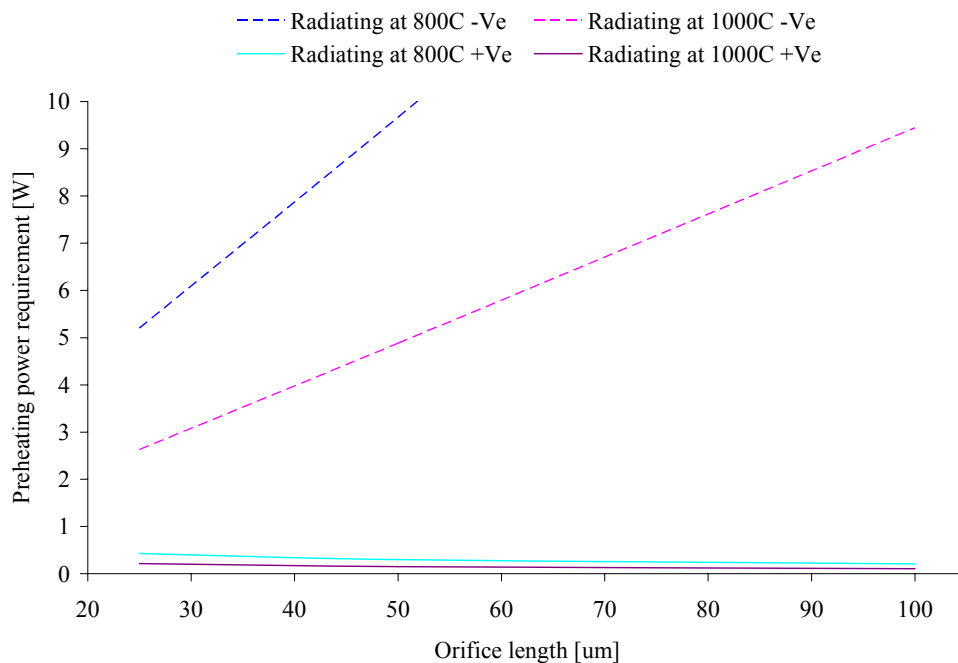


Figure 25 Preheating power requirement with respect to orifice length

The operating temperature of each emitter is shown in Figure 26. The reduced current requirement also leads to decreased emitter temperature, which in turn promotes greater lifetime.

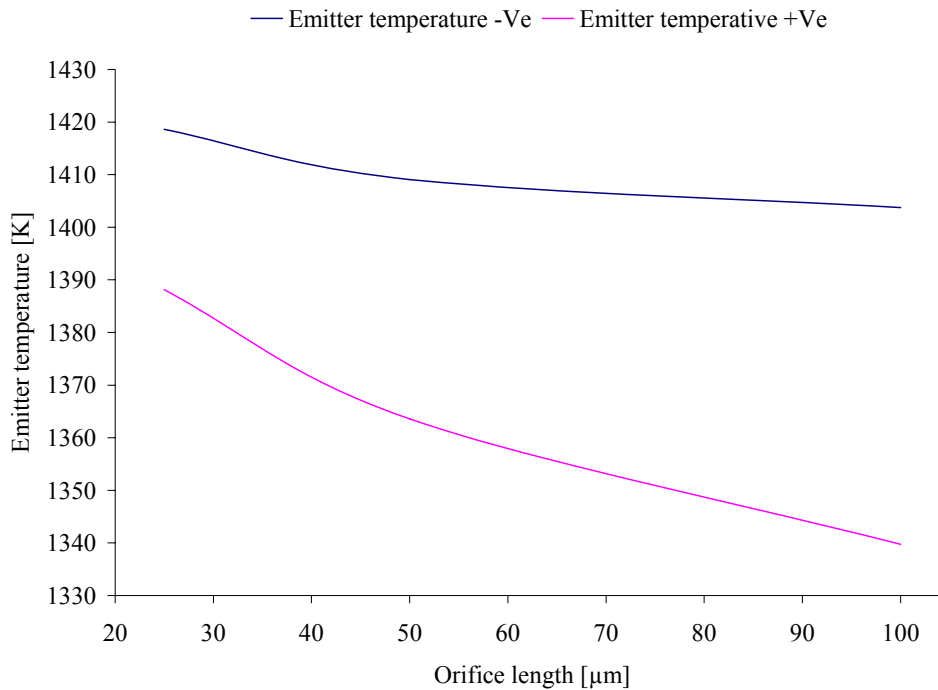


Figure 26 Emitter temperature with respect to orifice length

The evaporation rate of a 1mm² area of LaB₆ based on operating temperature is shown in Figure 27. Since both devices operate with a very low operating temperature due to the intense electric field from the small Debye length, the evaporation rate of LaB₆ is negligible. The inclusion of ion bombardment may change this rate but no data is available for this process.

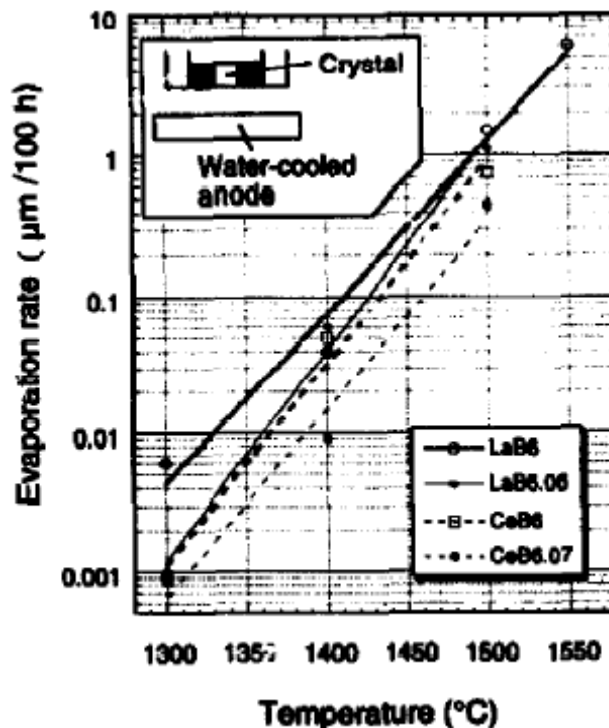


Figure 27 Directly heated lanthanum hexaboride filaments

Both of the cathode designs here operate at ~1340Torr or 1.76bar. Typical plasma screen displays operate at 500Torr however in pursuit of extended life by reducing discharge voltage manufacturers have sought operation at pressures >900Torr with plasma cavities of 50μm. In our application it may be reasonable to suggest that cathode lifetime may not be a problem, particularly if the +Ve

cathode is employed and current density is reduced. The large reduction in effective work function, from 2.5eV to 2.06eV is due to field-enhanced emission from the high plasma density. The Debye length is thus short causing a strong electric field at the emitter surface ($1.32 \times 10^8 \text{V.m}^{-3}$). The large reduction in work function actually enables the LaB₆ emitter to operate with an effective work function over 0.2eV lower than modern dispenser cathodes resulting in very large current densities. This has a stark effect on emitter temperature, operating at just 1408K to for the required discharge current. This operating temperature is only slightly higher (~50K-100K) than that of modern barium-tungsten dispenser cathodes. Emitter temperature remains constant for all orifice lengths since emitter length is varied in order to solve the energy balance at the surface. This also has the effect of keeping the operating temperature of the emitter constant, however it should be noted that emitter area only weakly influences operating temperature given the strong dependence of emitted current density on operating temperature. The assumption that emission is uniform over the complete emitter area only brings a small error in operating temperature. At this operating temperature the LaB₆ emitter, which typically operates at much higher temperatures, should have a lifetime well in excess of the mission length at least when considering emitter evaporation as the life limiting mechanism. The LaB₆ emitter should also be very resilient to poisoning and present reduced handling requirements when compared to impregnated cathodes.

This second design study has demonstrated the benefit in reducing ion recombination losses by novel design of the cathode assembly to provide resistive heating of the propellant while minimizing losses in the high pressure, high temperature region of the cathode orifice. Operating with an orifice diameter of 25μm and length of 50μm for instance gives an operating power of 0.59W for the for a cathode with orifice at positive potential when compared to the orifice at negative potential which operates at 3.58W, a factor of 7 reduction. The analysis has also shown that thermal evaporation rates of LaB₆ at these temperatures is very low and is thus not likely to be a life limiting mechanism.

6.11. Design iteration 3

This design study takes the novel +Ve orifice cathode and documents the varying performance with a fixed mass flow rate to demonstrate the possibility of performance throttling. Figure 28 shows the influence of discharge parameters on heavy particle temperature and specific impulse and relates this to the total power. Operation at 167 s and 240s requires operating powers of 0.85W and 2.64 respectively with corresponding heavy particle temperatures between 2000K-8000K.

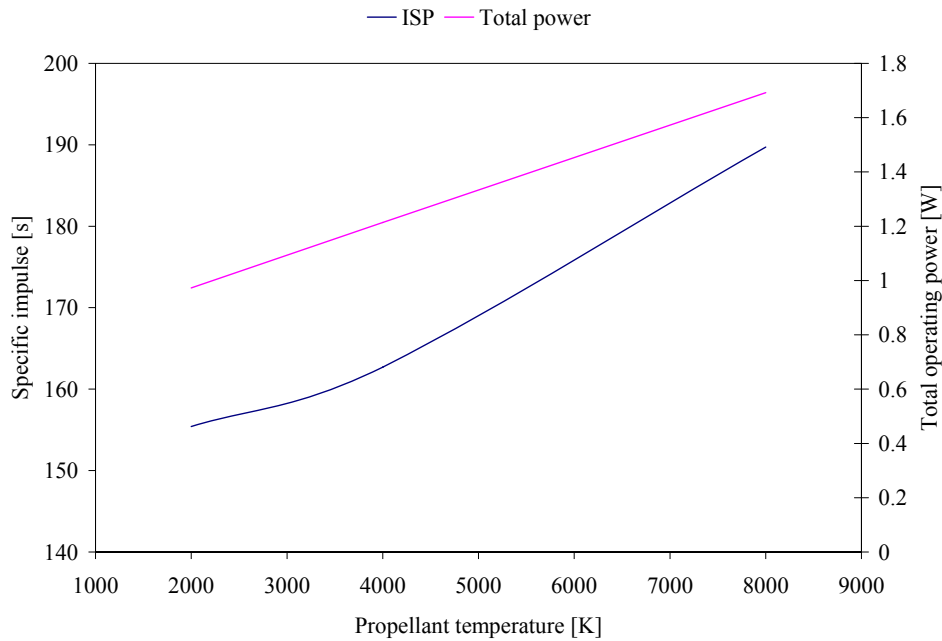


Figure 28 Specific impulse and total operating power with respect to propellant temperature

Since at lower heavy particle temperatures plasma density is higher at the orifice exit, the electron pressure component represents a larger fraction of the total thrust components. ISP is therefore artificially higher at lower heavy particle temperatures than pure gas dynamic theory would predict, something found in current hollow cathode thruster research.

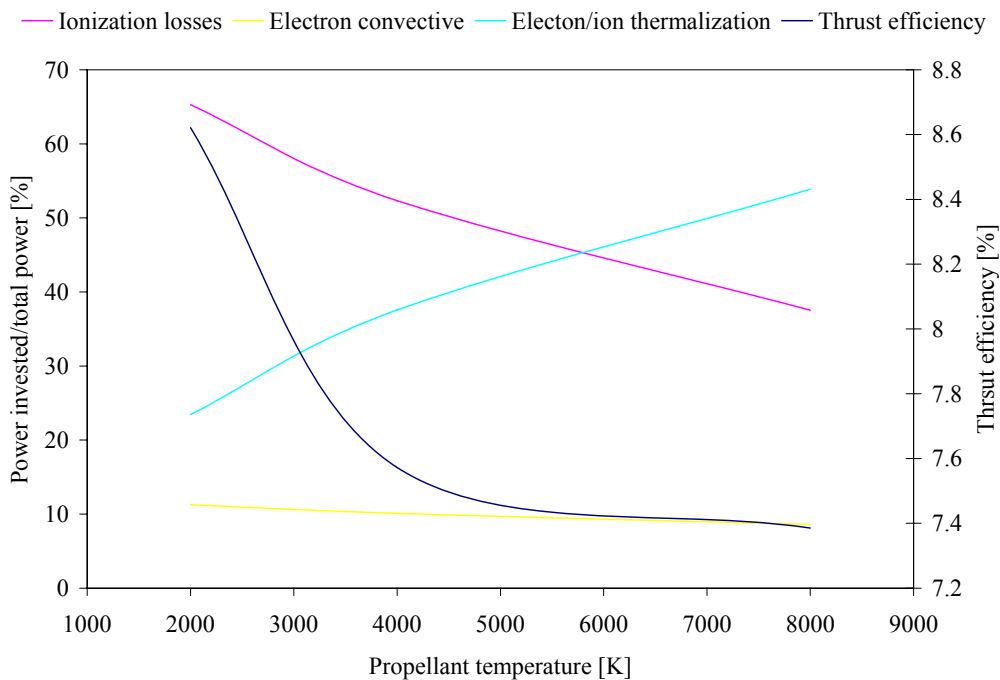


Figure 29 Relative power investment and total efficiency with increasing propellant temperature

Figure 29 depicts the change in relative power fractions as discharge current is increased. Given the longer orifice, electron convective losses remain below 10%, however frozen flow losses reduce propulsive efficiency at higher heavy particle temperatures since there is not full energy conversion.

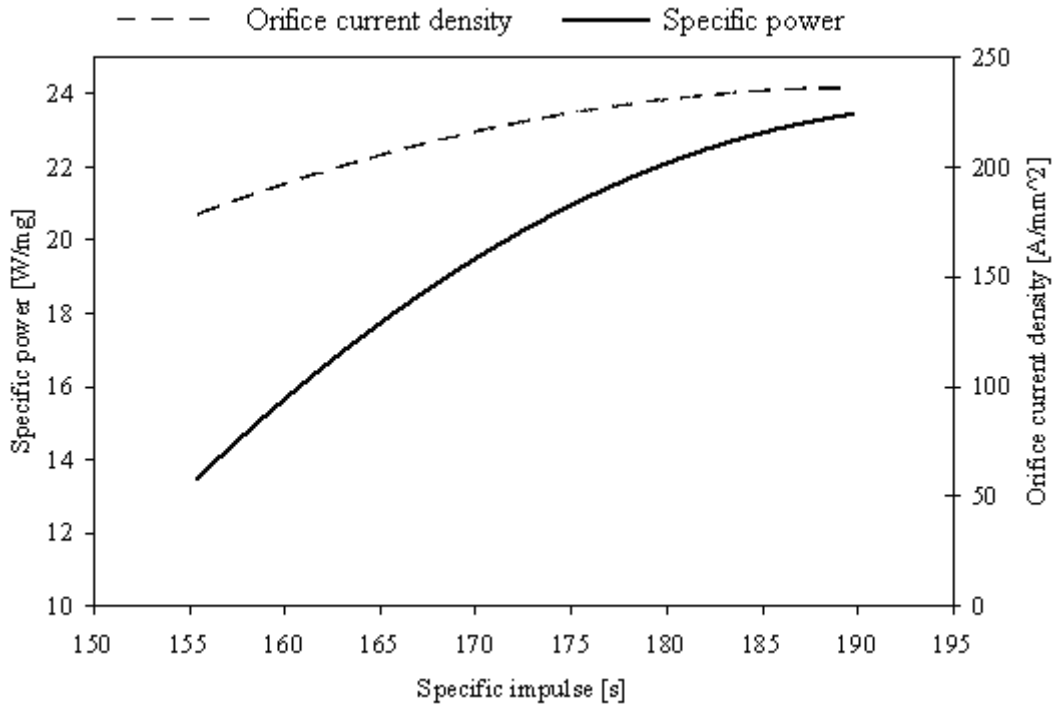


Figure 30 Specific power an orifice current density with respect to specific impulse

Figure 30 shows that by use of the +Ve orifice cathode performance can be varied without excessively high orifice current densities. Since the convective and ion recombination losses are minimized the device shows much lower specific powers for the same specific impulse as the T5 cathode.

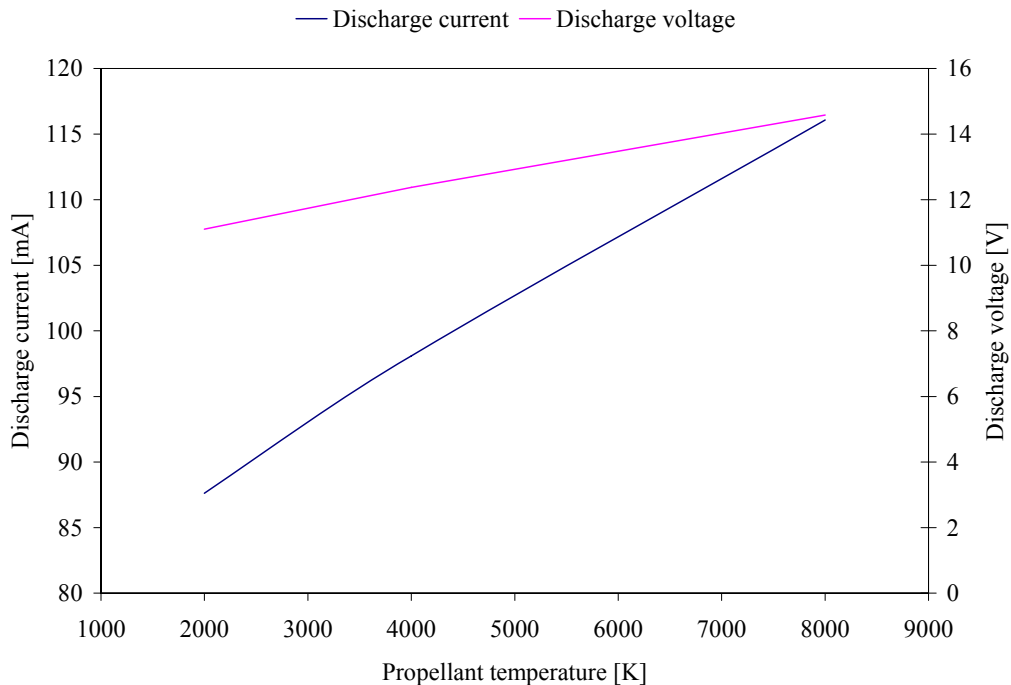


Figure 31 Required discharge current and discharge voltage with respect to propellant temperature

Figure 31 shows the necessary discharge current to increase heavy particle temperature and the corresponding operating voltage.

Design iteration 3 has provided insight into the possibility of changing the performance of a hollow cathode microthruster with a +Ve anode based on current regulation. This suggests that changing the performance of an individual cathode may be possible whilst keeping the discharge voltage within reasonable limits if the orifice geometry is selected accordingly. Operation in a POHC configuration also significantly reduces the orifice current density from a minimum (longest orifice lengths) of 608Amm^{-2} to 162Amm^{-2} in comparison to the negative orifice hollow cathode. Typical plasma screen microarrays operate at modest currents $\sim 5\text{--}10\text{mA}$ and give current densities $0.16\text{--}0.33\text{Amm}^{-2}$ however these devices rely on high voltages to facilitate ionization whereas operation in a hollow cathode demands higher current densities to facilitate ionization and promote low voltage efficient operation. As stated, current densities in the T5 hollow cathode are an order of magnitude higher than these microdischarge devices $\sim 65\text{Amm}^{-2}$ [70] yet the device has demonstrated lifetimes of many thousands of hours due to low voltage operation.

Within the orifice, the plasma density is very high and can be over 5-bar static pressure. The flow field within in this condition is found to have Knudsen numbers of approximately 5.4×10^4 indicating continuum flow. Corresponding Reynolds numbers are >800 also indicating that the flow field is laminar. In this sense, due to the high pressure and high temperature within the orifice a simple conical nozzle may also be beneficial.

6.11.1. Series Heater

Due to the low resistivity of tungsten, and indeed all refractory metals, a significant reduction in heater cross sectional area is required to give the desired resistivity for series operation. Figure 32 for example shows the relationship between heater track length width, length and height to provide 1.43W of input power (giving a 1200°C ignition temperature) while maintaining a voltage drop of 24V .

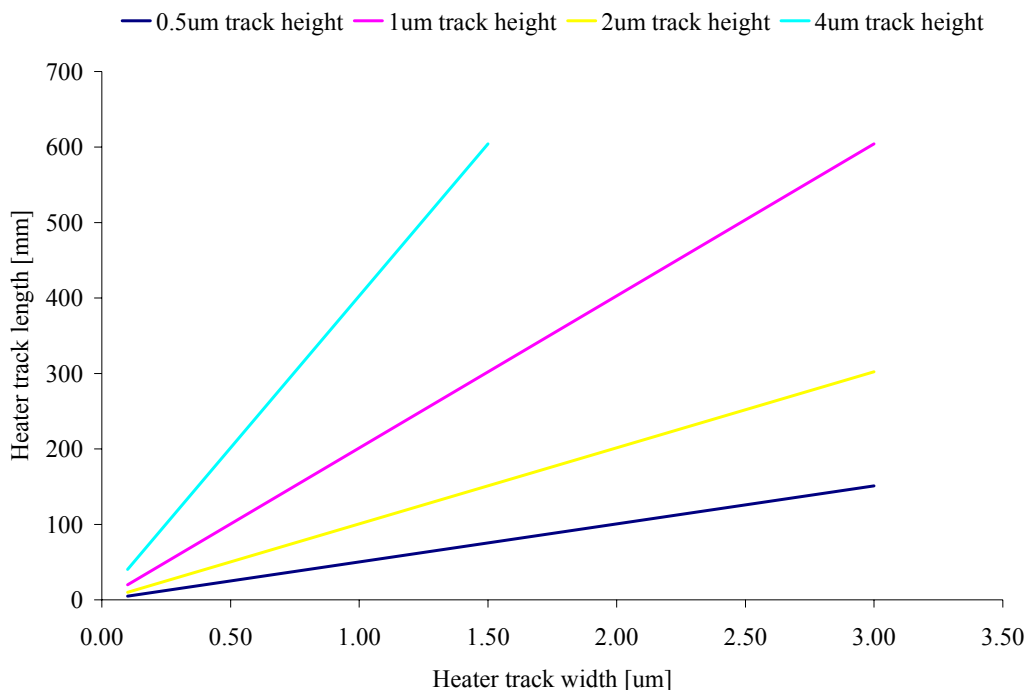


Figure 32 Figure Required heater track length to maintain operation at 24Volts dissipating 1.43W (59.6mA)

For a worst case chip size is 5.41mm and the track length can be considered as a number of windings, each winding constituting 5mm of track length. The practical upper limit for chip surface coverage by heater windings can be considered 50% . In this case of the product of track length and

width should not exceed 50% of the chip surface ($25,000,000\mu\text{m}^2$), for instance 200 windings ($1,000,000\mu\text{m}$ or 1000mm) of track width over $2.5\mu\text{m}$. It can be seen that for all reasonable track heights and widths we are some way below this limit. For the smallest track heights the highest surface coverage would be expected however a heater with a $3\mu\text{m}$ track width and $0.5\mu\text{m}$ track height gives only a 9% chip coverage area with 30 windings.

6.11.2. Parallel Heater

Alternatively to reduce the chance of a heater failure resulting in the failure of the device the heater windings can be connected in parallel in which case an individual winding failure would result in increased current through each winding and a corresponding increase in voltage and dissipative output from each winding but not device failure. Track length is assumed to be the length of the chip.

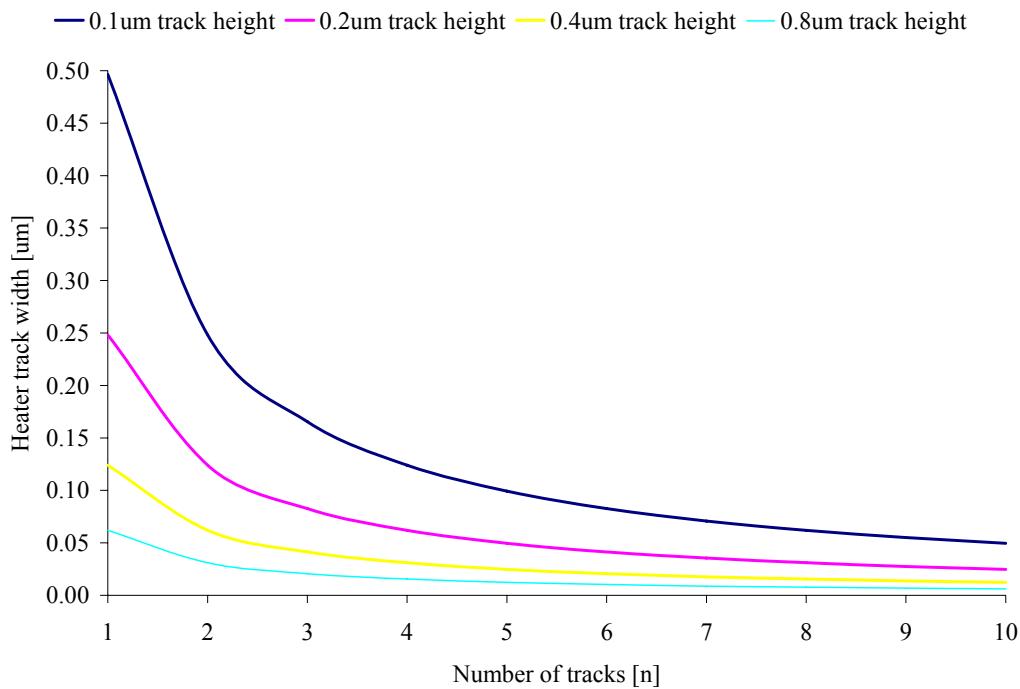


Figure 33 Figure Required track length width base on track number and height in a parallel heater circuit

Number of tracks [n]	Track resistance [Ohms]
1	402.80
2	805.59
3	1208.39
4	1611.19
5	2013.99
6	2416.78
7	2819.58
8	3222.38
9	3625.17
10	4027.97

Table 4 Individual track resistance for increasing track numbers

The individual resistive parameters for each track are shown below in Table 3. As the number of tracks increases so does the required resistivity in each individual track to maintain the total circuit resistance. Again the circuit has been designed to give a total voltage drop of 24V consistent with a small satellite bus. In this case 59.6mA is required to give the 1.43W dissipative power in the heater

for ignition, the total circuit resistance being 403.8Ω . Since the track length is short, the required track height and width dramatically decreases with greater track numbers generating very thin tracks, thus making redundancy in design itself a reliability issue. This can be overcome by individually winding each track to give a much longer track length, generating higher resistivity. This can easily be produced by conventional MEMS manufacturing processes. By winding each track 20 times the following parameters are achieved.

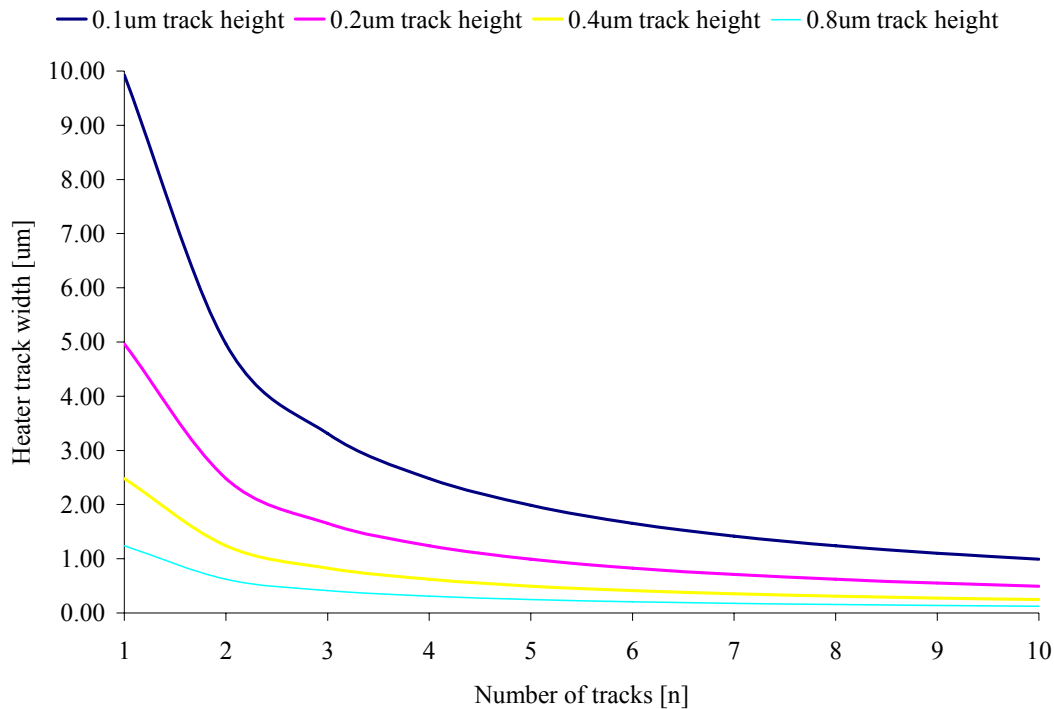


Figure 34 Figure Track geometry required for 20 windings on each track of a parallel heater circuit to produce 1.43W at 24V with 59mA

Reduced track height and winding to increase track length results in greater track width and thus increased binding area with the substrate while allowing for a chosen degree of redundancy in the system. The greatest track coverage is also only 3.9% of the chip surface. The parallel heater circuit design gives much more redundancy over a series circuit in the event of an individual track failure and is therefore the preferred option.

7. Discussion

7.1. Concepts

From our parametric model we have outlined the approximate terminal parameters such as discharge current, mass flow rate, orifice geometry and orifice design have on the performance of a potential hollow cathode microthruster. We have also shown how orifice plasma conditions and performance demands strongly influence backpressure and thus emitter geometry for preservation of the hollow cathode effect to reduce discharge voltage. Since orifice diameter must be set to give sufficient backpressure for small emitter geometries orifice length and discharge current must also be selected to give sufficient resistive dissipation and ion heating for the required performance

level. Operation at lower currents can be achieved by increasing orifice length which decreases the required chip size to maintain radiative cooling, but also then reduces the power requirement for ignition. In the +Ve orifice design there is no issue in increasing orifice length since ions are not inclined to recombine on its walls. Orifice aspect ratios should be kept reasonable however to facilitate the process of ignition since long thin orifices have shown difficulty in igniting. We have also shown that, at least at the discharge voltages we encounter, comparisons with empirical low energy sputtering data would not suggest that thruster lifetime based on ion erosion is an issue even for the higher energy ions sometimes seen in hollow cathode discharges.

This parametric scaling model can be used to determine the possible design of hollow cathode thrusters in both conservative and demanding configurations. We have considered 3 separate configurations for both a micro (20kg) and picospacecraft (1kg). These concepts with associated design criteria are shown in Table 4.

Concept	Micro-Spacecraft [20kg]			Pico-Spacecraft [1kg]		
	Array	Conservative	Demanding	Array	Conservative	Demanding
Thrust level [mN]	0.11			0.014		
Specific impulse [s]	>130s	>130s	>180s	>130s	>130s	>180s
Orifice current density [A/mm ²]	<150	<150	>300	<150	<150	>300
Number of cathodes	25	1	1	100	1	1
Operating pressure [bar]	<1	<1	<5	<1	<1	<5
Propulsive efficiency [%]	>5	>5	>8	>5	>5	>8

Table 5 Preliminary device criteria

Each spacecraft has 3 configurations based on the conservativeness of the design. The first is an array of hollow cathodes with 25 and 100 cathodes for the micro and picospacecraft respectively. This design reflects an ultra-conservative approach with arrays of thruster for multiple redundancies operating at low current density and with modest performance parameters. The conservative approach reflects the same design criteria as previous however with only a single cathode. The final demanding configuration reflects a design requiring high specific impulse with little concern for reducing current density.

7.2. Parametric Scaling Results

Based on the performance parameters in table 1, the model was iterating until the maximum number of criteria were met for each configuration. The result for each concept is shown in Table 6.

Spacecraft Type	Microspacecraft (20kg)			Picospacecraft (1kg)		
	Array	Conservative	Demanding	Array	Conservative	Demanding
Dimensions						
Aspect ratio [orifice diameter/orifice length]	0.20	0.29	0.38	0.02	0.25	0.23
Orifice Diameter [μm]	6	28	15	0.5	10	7
Orifice Length [μm]	30	98	40	25	40	30
Number of thrusters on array	25	1	1	100	1	1
Emitter diameter [μm]	107.6	93.7	37.1	23.5	93.9	63.5
Emitter length [μm]	1075.8	937.1	371.1	234.8	939.2	635.0
Required Surface Area for radiation at 1000C [mm ²]	1.79	0.89	0.89	0.15	0.18	0.17
Required Surface Area for radiation at 800C [mm ²]	3.55	1.77	1.77	0.29	0.36	0.35
Propulsive performance						
Thrust [uN]	110	110	110	14	14	14

Effective Isp [s]	155.4	155.4	189.7	155.4	155.4	189.7
Thrust Efficiency [%]	8.42	9.02	7.67	5.13	8.65	7.47
Electrical operating parameters						
Discharge current/cathode [mA]	4.27	53.16	53.28	0.09	10.83	10.41
Discharge voltage [V]	9.34	17.48	25.03	23.59	11.40	16.74
Total operating power [W]	0.996	0.929	1.334	0.208	0.123	0.174
Specific power [W/mg]	345.22	12.88	22.57	2264.01	13.43	23.17
Physical operating parameters						
Mass flow [μg/s]	2.89	72.16	59.10	0.09	9.18	7.52
Required Gas Temperature [K]	2000	2000	8000	2000	2000	8000
Pressure electrode separation product [Torr/cm]	2.48	9.30	9.58	9.46	3.79	4.20
Orifice						
Choked flow velocity through orifice [m/s]	459.4	459.4	918.8	459.4	459.4	918.8
Orifice plasma density [/m ³]	1.0E+24	1.2E+24	1.7E+24	4.6E+24	1.2E+24	9.7E+23
Electron temperature within orifice [K]	5797	5797	5797	5797	5797	5797
Lambda	15.36	15.29	15.11	14.60	15.29	15.38
Orifice resistance [Ohms]	2189.2	328.9	469.8	267688.7	1052.5	1607.6
Orifice Pressure [Torr]	826.28	948.54	2395.26	3785.87	946.47	1399.83
Orifice pressure [bar]	1.09	1.25	3.15	4.98	1.25	1.84
Orifice current density [A/mm ²]	150.9	86.3	301.5	448.8	137.8	270.6
Orifice power loading [MW/cm ³]	2994.3	1052.2	7357.9	16463.3	2572.4	5733.5
Emitter						
Plasma density inside emitter [/m ³]	5.91E+24	6.78E+24	1.71E+25	2.71E+25	6.77E+24	1.00E+25
Cathode internal pressure [bar]	1.22	1.40	3.55	5.60	1.40	2.07
Cathode internal pressure [Torr]	929.57	1067.10	2694.67	4259.10	1064.78	1574.80
Emitter number density [/m ³]	4.39E+24	5.04E+24	1.27E+25	2.01E+25	5.03E+24	7.44E+24
Electric field strength [V/m]	6.01E+07	6.44E+07	1.02E+08	1.29E+08	6.43E+07	7.82E+07
Effective work function [eV]	2.21	2.20	2.12	2.07	2.20	2.16
Emitter operating temperature [K]	1160.2	1315.1	1461.9	1126.7	1223.2	1270.5
Emitter diameter pressure product [Torr-cm]	10	10	10	10	10	10
Current density given at emitter surface [kA/m ²]	0.436	8.220	132.999	0.867	1.660	5.170
Power flow parameters						
Electron convective power loss/cathode [mW]	5.34	66.48	66.63	0.11	13.54	13.02
Electron convective loss/total power [%]	0.54	7.15	5.00	0.05	10.97	7.47
Ion power loss/total power [%]	63.73	68.32	38.99	38.87	65.50	37.98
Thermal energy addition to ions + electrons/total power [%]	0.92	24.53	56.01	0.56	23.52	54.55
Pressure thrust contribution [%]	69.86	69.86	50.63	69.86	69.86	50.63
Pre ignition						
Preheating requirement with 800°C radiating area [W]	0.948	0.472	0.473	0.078	0.096	0.092
Preheating requirement with 1000°C radiating area [W]	0.239	0.119	0.119	0.020	0.024	0.023
Heater track width [μm]	1	2	1	0.1	0.5	0.5
Heater layer height [μm]	0.5	0.5	0.5	0.01	0.1	0.1
Heater track length [mm]	75.99	304.96	152.14	1.84	74.87	77.84
Total heater resistance [Ohms]	607.96	1219.86	1217.12	7357.76	5989.88	6227.55
Heater operating voltage [V]	24.00	24.00	24.00	24.00	24.00	24.00
Heater current [mA]	39.48	19.67	19.72	3.26	4.01	3.85
Number of windings and number of tracks	1419(5)	322(5)	160(5)	478(2)	175(2)	186(2)
Surface coverage of chip by heater %	79.22	72.30	17.97	32.30	48.28	53.22
Flow conditions						
Debye length [m]	5.23E-09	4.89E-09	4.09E-09	2.45E-09	4.89E-09	5.35E-09
Reynolds number	28.89	154.77	236.64	11.03	55.15	64.54

Table 6 Parametric scaling results for both pico and micro spacecraft concepts for array, conservative and demanding configurations

7.3. Microspacecraft Concept

All solutions to provide the 0.11mN of thrust for the microspacecraft concept seem feasible. The array configuration requires very small orifices $\sim 6\mu\text{m}$ which are also long $\sim 30\mu\text{m}$ to give sufficient resistive dissipation into the plasma. Arrays larger than 5x5 therefore require orifices which are limited by current MEMS manufacturing processes as discussed in Part 2. As expected, the array configuration gives a lower efficiency due to the higher total current requirement however the device is still able to provide 155s specific impulse while still operating at 1.0W. Operation at a higher performance 190s in a single thruster produces the poorest performance of 7.67% and requires 1.33W. Chip size correlates with total discharge current however even the high current array requires only 1.79mm² and 3.55mm² surface area for radiative cooling at 1000°C and 800°C respectively. Chip size and packing density are therefore not anticipated to be an issue.

Scaling of the emitter cavity has also shown that by selecting orifice diameter to regulate backpressure $>1\text{bar}$ minimizes emitter geometry. Consequently the ‘demanding’ thruster configuration has shown high backpressures of up to 3.55 bar. This may present a propellant utilization problem however if necessary orifice diameter could be increased along with discharge current for the same performance at lower efficiency. Reynolds numbers are also shown to be below 250 for all conditions indicating laminar flow and Knudsen numbers would also indicate that the flow is in a continuum regime. In reality this highlights that the actual values of specific impulse based on a heated choked flow assumption may be close to the theoretical values.

For the conservative and array concepts the chip coverage area by the heater is fairly high due to the need for very long track lengths to provide sufficient resistance in the circuit. In any case it should be possible to manufacture a heater on chip operating $\sim 24\text{V}$ as also discussed in Part 2. The preheating power requirement is very dependent on the chip area. Chips designed to operate at 1000°C have considerably lower preheating requirement than the 800°C chip size due to the 4th power relation. It is likely that the chip would be designed to reside at the higher operating temperature in order to minimise conductive losses from the emitter which will drive up discharge voltage. In this case the preheating power requirement is 25%, 13% and 8.9% of the total operating power for the array, conservative and demanding design respectively.

The electric field at the emitter surface $\sim 10^7\text{ V/m}$ primarily due to the small Debye length (4 - 5.2pm) leads to a large reduction in effective work function from 0.3 – 0.43eV for both the pico and micro concepts. This is a significantly larger reduction than in conventional LaB₆ cathodes since they are traditionally operated at much lower operating pressure and thus relatively high temperatures. At the temperatures shown in this study a safe assumption would be that lifetime will not be limited by thermal desorption of the emitter material since LaB₆ cathodes have traditionally operated at much higher temperatures for thousands of hours.

Since a cathode array must operate in the abnormal glow mode it is important to realize that a hollow cathode thruster array can only be designed for operation beyond a critical current. Operating at discharge currents below the abnormal glow mode will result in negative resistance in one or more individual cathodes and thus excessive current flowing to these cathodes. Increased orifice pressure in the higher current cathodes will then also drive increased mass flow to other cathodes and thus the array may experience a significant drop in efficiency or excessive current to individual cathodes. Abnormal glow mode will be distinguishable by a general increase in discharge voltage with discharge current thus dictating the power level and performance however this relationship will have to be established empirically.

Since the operating parameters of the thruster fall well within the general resource constraints of small spacecraft it is anticipated that the successful development of a hollow cathode microthruster on a chip would seem feasible from an operation viewpoint.

7.4. Picospacecraft Concept

The pico spacecraft concepts generated cathodes which could meet the thrust requirement of 0.014mN while operating at much lower power (0.12 – 0.21W). The array configuration of 100 cathodes however required very small orifices of 0.5 μ m to give sufficient backpressure. This is on the limit of MEMS manufacture given that the orifice also had to be 25 μ m in length to give sufficient dissipation. Such long thin orifices may also suffer from ignition problems given the relatively large separation between electrodes. This may result in electrical breakdown at higher voltages than the spacecraft bus is able to provide.

The ‘conservative’ and ‘demanding’ designs operated at 8.65% and 7.47% efficiency similar to the corresponding microspacecraft designs however the array operated at only 5.13%. Current density in the array configuration is also high (~ 450 A/mm²), almost 7 times that of the T5 cathode. Heater power required for ignition is 9.5% 19.7% and 13.3% of the total operating power for the array, conservative and demanding concepts respectively with the circuit designed such that the total heater voltage drop was 24V at maximum power. In this case the pico configuration required low cross sectional area tracks to minimise chip coverage. At the extreme case the array configuration required 0.1 μ m width tracks of height 0.01 μ m. Furthermore only 2 tracks could be used for all configurations for acceptable chip coverage. In this case a heater winding failure will result in a double over current in one single winding, thus 4 times the power dissipation. In this case heater voltage will have to be monitored for any sign of single heater winding failure and current adjusted accordingly. Again Reynolds numbers are low (<70) for all conditions indicating suggesting laminar flow and Knudsen numbers would also indicate a continuum regime and that ISP predictions should be reasonably accurate.

7.5. Empirical Comparisons

Hutchinson [97] conducted experiments on the scaling of hollow cathodes to low power. Three devices were manufactured with differing characteristic; a simple molybdenum body cathode, a body impregnated cathode and an emitter-impregnated cathode with insert. Cathodes had a 0.2mm diameter internal orifice channel and the carbon-carbon emitter matrix in the third case was impregnated with barium carbonate. A 1mm diameter central orifice keeper 1mm deep was placed at varying distances from the cathode and a 25mm diameter tantalum ring 10mm in depth was used as the anode.

Hutchinson showed that initiation voltage scaled with anode cathode separation while operating with anode keeper separations of from 0.5mm, 0.8mm and 1.2mm. Figure 36 below shows extrapolations of Hutchinson’s results down to zero separation. In our parametric scalings we have used flow rates in individual cathodes ranging from 2.89 μ g/s to 72.16 μ g/s however due to the much smaller orifice diameter we have used (25 μ m-98 μ m) the operating pressure is much higher. The range of orifice lengths we have used can also represent the separation distance between electrodes. It is difficult to draw conclusions on these empirical comparisons given the difference in geometry, operating pressure and the influence of field effects; however, it can be seen that electrode separations in the 25 μ m-98 μ m range, even for low pressure operation, the projected ignition voltage is low. Since Hutchinson’s orifice diameter was over 200 μ m, the operating pressure would have been much lower and ignition much more difficult.

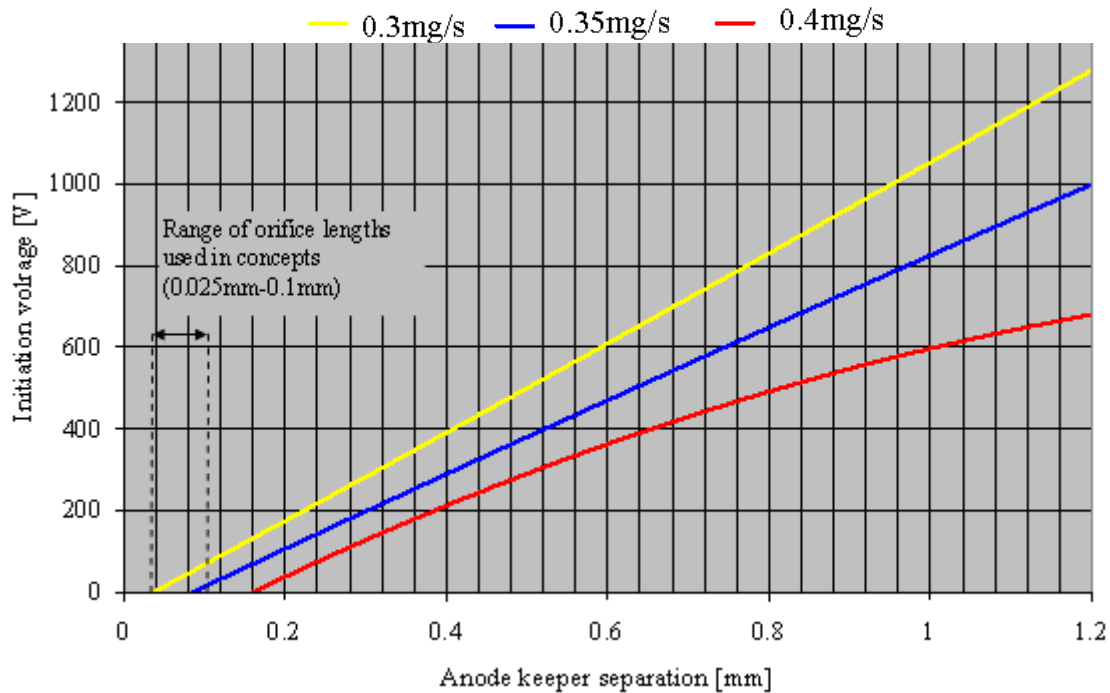


Figure 35 Extrapolation of Hutchinson's results down to very small anode keeper separations

Flow rate, kg s^{-1}	Minimum Discharge Voltage [V]		
	Simple Mo 0.9mm (keeper dist)	Surface impregnated 0.5mm (keeper dist)	Impregnated insert 0.5mm (keeper dist)
4.5×10^{-7}	355	91	78
1×10^{-6}	160	75	63
1.8×10^{-6}	142	64	58

Table 7 Minimum discharge voltage obtained from 3 types of cathode

The minimum discharge voltage for each of the cathodes is shown in Table 7. Discharge voltage is seen to significantly reduce with the inclusion of impregnates in the cathode. Although the impregnated insert manufacture may have been far from perfect, it does demonstrate that at higher flowrates, and hence higher discharge pressures, it is possible to achieve discharge voltages at least as low as 58V. In our case we are operating at much higher discharge pressures and at an optimum point with regards to the pressure-emitter diameter product. We would also be operating with a pure LaB_6 emitter and may have reduced work function in comparison to the carbon-carbon matrix. In the case of Hutchinson cathodes p-d values would have also been far below optimum for hollow cathode enhancement and emitter to anode separation is at least 20 times greater, both of which would lead to an increase in discharge voltage. In this case it can be assumed that we would with confidence be able to produce discharge voltages of at least <58V with our scalings. The major operating parameters of the impregnated insert cathode are shown in Table 8 and compared with the results from the parametric scaling for the microspacecraft conservative and demanding scenarios. The table also shows a parametric model result given the geometry and approximate flowrates of Hutchinson's design however with an operating point determined (in the model) give a fully ionized flow with a heavy particle temperature of 1500°C.

For similar flow rates and geometry the required discharge current of 100.1mA does significantly exceed the 1.5-13.3mA of Hutchinson's work however this can be expected since the flow in Hutchinson's cathode is likely to have a very low ionization fraction. The discharge voltage in the model of 32V would seem representative since Hutchinson showed that discharge voltage reduced with increasing discharge current however he was limited in the maximum current of the power supply to 13.3mA. Should he have increased current further he may well have seen further

reduction in discharge voltage to the levels of our parametric comparison. The total operating power is also close to the upper bounds found with Hutchinson's cathode.

Cathode	Hutchinson (impregnated insert)	Hutchinson/ parametric model	Conservative micro- spacecraft	Demanding micro- spacecraft
Orifice size [μm]	200 I.D, 1000 length	200 I.D, 1000 orifice	28 I.D, 98 orifice	15 I.D, 40 orifice
Flow rate [kgs^{-1}]	$2.7 \times 10^{-7} - 2.2 \times 10^{-6}$	3×10^{-7}	7.22×10^{-8}	5.91×10^{-8}
Discharge current [mA]	1.5 – 13.3	100.1	53.16	53.28
Discharge voltage [V]	54 – 220	32.1	17.48	25.03
Power [W]	0.33 – 2.93	3.21	0.929	1.33

Table 8 Comparison of major parameters for Hutchinson's cathode and the parametric model results for Hutchisons cathode and also the conservative and demanding microspacecraft designs

Table 8 also shows a comparison with the major parameters of the conservative and demanding microspacecraft design. Although significantly different in geometry, this does generate confidence that the major operating parameters of a real miniaturized device should not be significantly different from those produced from the parametric model.

8. References

- [1] AN Grubisic and SB Gabriel, *Characterization of the T-series hollow cathode thrusters for all-electric spacecraft*, IEPC-2007-81, International Electric Propulsion Conference, Florence, Italy, (2007).
- [2] AN Grubisic and SB Gabriel, *Hollow cathode thrusters for all-electric spacecraft*, IAC-07-C4.4.07, 58th International Astronautical Federation Congress, Hyderabad, India, (2007).
- [3] S Pottinger, P Gessini, D Webb, R Intini Marques and SB Gabriel, *Electric propulsion research at the University of Southampton*, Journal of the British Interplanetary Society, **59**(5), (2006).
- [4] P Gessini, SB Gabriel and DG Fearn, *Thrust characterization of a T6 hollow cathode*, IEPC Paper 05-257, 29th International Electric Propulsion Conference, Princeton, NJ, (2005).
- [5] P Gessini, SB Gabriel and DG Fearn, *The T6 hollow cathode as a microthruster*, AIAA Paper 2005-4078, 41st AIAA/ASME/SAE/ASEE Joint Propulsion Conference & Exhibit., Tucson, AZ, (2005).
- [6] HL Gray, *Development of ion propulsion systems*, GEC Rev., **12**(3), 154-168 (1997).
- [7] NC Wallace and DG Fearn, *The design and performance of the T6 ion thruster*, AIAA Paper 98-3342, (1998).
- [8] D Fearn, A Singfield, N Wallace, S Gab and P Harris, *The operation of ion thruster hollow cathodes using rare gas propellants*, AIAA Paper 90-2584, (1990).
- [9] PM Latham, AR Martin and A Bond, *Design, manufacture and performance of the UK-25 engineering model thruster*, AIAA Paper 90-2541, (1990).
- [10] PT Harris and S Gair, *A review of the cathode construction for the RAE 10/25 mN thruster*, IEPC Paper 88-078, (1988).
- [11] CM Philip and DG Fearn, *Recent hollow cathode investigations at the Royal Aircraft Establishment*, AIAA paper 73-1137, (1973); AIAA J, **12**, 10, 1319-25, 1974.
- [12] DG Fearn, *The operation of hollow cathodes under conditions suitable for ion beam neutralization*, IEE Conf. Pub., **100**, 146-150 (1973).

- [13] AM Baker, A Da-Silva-Curiel, J Schaffner and M Sweeting, *Advanced low cost propulsion concepts for small satellites: Beyond LEO*, IAC Paper No. 04-IAF-S.1.08, (2004).
- [14] RS Jankovsky, JM Sankovic and S Oleson, *Performance of a FAKEL K10K resistojet*, AIAA-1997-3059, 33rd AIAA/ASME/SAE/ASEE Joint Propulsion Conference and Exhibit., Seattle, WA, (1997).
- [15] I Coxhill and D Gibbon, *A xenon resistojet propulsion system for microsattellites*, AIAA-2005-4260 41st AIAA/ASME/SAE/ASEE Joint Propulsion Conference and Exhibit., Tucson, Arizona, (2005).
- [16] Inter-Agency Space Debris Coordination Committee, *Space Debris Mitigation Guidelines*, IADC 02-01 (2002).
- [17] DH Manzella, FM Curran and DM Zube, *Preliminary plume characteristics of an arcjet thruster*, AIAA Paper No. 90- 2645, (1990).
- [18] J Mueller, *Thruster options for microspacecraft*, in ‘Micropropulsion for Small Spacecraft’ Volume 187 Progress in Astronautics and Aeronautics.
- [19] J Mueller, J Ziemer, A Green and D Bame, *Performance characterization of the vaporizing liquid micro-thruster (VLM)*, IEPC-03-247, AIAA International Electric Propulsion Conference, (2003).
- [20] MD Rayman and DH Lehman, *NASA’s first new millennium deep-space technology validation flight*, Second IAA International Conference on Low-Cost Planetary Missions, Laurel, MD, (1996), IAAL-0502.
- [21] P Bodin, S Berge, M Bjork, A Edfors, J Kugelberg and P Rathsmann, *The SMART-1 attitude and orbit control system: Flight results from the first mission phase*, AIAA-2004-5244 AIAA Guidance, Navigation, and Control Conference and Exhibit., Providence, Rhode Island, (2004).
- [22] H Kuninaka, Y Shimizu, T Yamada, I Funaki and K Nishiyama, *Flight report during two years on HAYABUSA explorer propelled by microwave discharge ion engines*, AIAA-2005-3673, 41st AIAA/ASME/SAE/ASEE Joint Propulsion Conference and Exhibit., Tucson, Arizona, (2005).
- [23] MD Rayman, TC Fraschetti, CA Raymonda and CT Russell, *Preparing for the dawn mission to Vesta and Ceres*, IAC-05-A3.5.B.011, 56th International Astronautical Congress, Fukuoka, Japan, (2005).
- [24] J Moerel, T Marée, V Bombelli and D Simon, *Economic benefits of the use of non-toxic mono-propellants for spacecraft applications*, AIAA-2003-4783, 39th AIAA/ASME/SAE/ASEE Joint Propulsion Conference and Exhibit., Huntsville, Alabama (2003).
- [25] M Coletti, A Grubisic, N Wallace and N Wells, *European student moon orbiter solar electric propulsion subsystem architecture – An all–electric spacecraft*, IEPC-2007-111, 30th International Electric Propulsion Conference, Florence, Italy, (2007).
- [26] R Walker, *The SIMONE mission: low-cost exploration of the diverse NEO population via rendezvous with microsattellites*, IAC-03-Q.5.05, 54th International Astronautical Congress of the International Astronautical Federation, The International Academy of Astronautics and The International Institute of Space Law, Bremen, Germany, (2003).
- [27] JL Cronin, *Modern dispenser cathodes*, IEEE Proc., **128**, 19–32 (1981).
- [28] RA Martin, *Atomic excitation processes in the discharge of rare gas ion-engines*, J. Phys. BLAtom. Molec. Phys., 7(10), pages? (1974).
- [29] M Crofton and ID Boyd, *Plume measurement and modeling results for a hollow cathode micro-thruster*, AIAA Paper No. 2001-3795, (2001).
- [30] TR Sarver-Verhey, *28,000 hour xenon hollow cathode life test results*, IEPC Paper No. 97-168, (1997).
- [31] VK Rawlin, *A 13,000 hour test of a mercury hollow cathode*, NASA TM X-2785, (1973).
- [32] TR Sarver-Verhey, *Extended test of a xenon hollow cathode for a space plasma contactor*, NASA CR–195402 (1994).
- [33] A Sahli and PJ Turchi, *Low power plasma thruster based on a hollow cathode discharge*, AIAA Paper No. 94-3126, (1994).

- [34] G Williams, T Smith, M Domonkos, K Shand, and A Gallimore, *Laser induced fluorescence characterization of ions emitted from a hollow cathode*, AIAA Paper No. 99-2862, (1999).
- [35] MT Domonkos, AD Gallimore and MJ Patterson, *An evaluation of hollow cathode scaling to very low-power and flow rate*, IEPC Paper No. 97-189, (1997).
- [36] I Katz and MJ Patterson, *Optimizing plasma contactors for electrodynamic tether missions*, Tether Technology Interchange, Huntsville, AL, (1997).
- [37] I Mikellides, I Katz, DM Goebel and JE Polk, *Theoretical model of a hollow cathode plasma for the assessment of insert and keeper lifetimes*, AIAA Paper No. 2005-4234, (2005).
- [38] JW Frame, DJ Wheeler, TA DeTemple and JG Eden, *Appl. Phys. Lett.*, **71**, 1165 (1997).
- [39] JW Frame and JG Eden, *Electron. Lett.*, **34**, 1529 (1998).
- [40] SJ Park, CJ Wagner and JG Eden, *IEEE Photon. Tech. Lett.*, **13**(1), 61 (2001).
- [41] SJ Park, J Chen, CJ Wagner, NP Ostrom, C Liu and JG Eden, *Microdischarge arrays: a new family of photonic devices* IEEE J. Sel. Topics Quantum Electron., **8**(3), 87–94 (2002).
- [42] OB Postel and MA Cappellia, *Parametric study of the vacuum ultraviolet emission and electrical characteristics of a He–Xe microdischarge*, *Appl. Phys.*, **89**, 4719 (2001).
- [43] AD White, *J. Appl. Phys.*, **30**, 711 (1959).
- [44] DJ Sturges and HJ Oskam, *J. Appl. Phys.*, **35**, 2887 (1964).
- [45] JW Frame and JG Eden, *Planar microdischarge arrays*, *Electron. Lett.*, **34**(15), 1529–1531 (1998).
- [46] KH Schoenbach, R Verhappen, T Tessnow, FE Peterkin and WW Byszewski, *Microhollowcathode discharges*, *App. Phys. Lett.*, **68**(1), 13–15 (1996).
- [47] JW Frame, DJ Wheeler, TA DeTemple and JG Eden, *Microdischarge devices fabricated in silicon*, *App. Phys. Lett.*, **71**(9), 1165–1167 (1997).
- [48] SJ Park, CJ Wagner, CM Herring and JG Eden, *Flexible microdischarge arrays: Metal/polymer devices*, *App. Phys. Lett.*, **77**(2), 199–201 (2000).
- [49] E Klassen, K Peterson, J Noworolski, J Logan, N Maluf, J Brown, C Storumment, W McCulley, and G Kovacs, *Silicon fusion bonding and deep reactive ion etching: A new technology for microstructures*, *Sensors & Actuators A*, **52**(1–3), 132–139 (1996).
- [50] JG Eden and SJ Park, *Microcavity plasma devices and arrays: a new realm of plasma physics and photonic applications*, *Plasma Phys. Control. Fusion*, **47**, 83–92 (2005).
- [51] J Chen, SJ Park, Z Fan, JG Eden and C Liu, *Development and characterization of micromachined hollow cathode plasma display devices*, *J. MEMS*, **11**(5), (2002).
- [52] M Trupke, F Ramirez-Martinez, EA Curtis, JP Ashmore, S Eriksson, EA Hinds, Z Moktadir, C Gollasch, M Kraft, GV Prakash and JJ Baumberg, *Pyramidal micro-mirrors for microsystems and atom chips*, *Appl. Phys. Lett.*, **88**, 071116, (2006).
- [53] S Eriksson, M Trupke, HF Powell, D Sahagun, CDJ Sinclair, EA Curtis, BE Sauer, EA Hinds, Z Moktadir, CO Gollasch and M Kraft, *Integrated optical components on atom chips*, *European Physical Journal D*, **35**(1), 135-139 (2005).
- [54] M Moselhy, I Petzenhauser, K Frank and KH Schoenbach, *Excimer emission from microhollow cathode discharges in argon*, *J. Phys. D: Appl. Phys.*, **36**, 2922–2927 (2003).
- [55] SJ Park, KF Chen, NP Ostrom and JG Eden, *40,000 pixel arrays of ac-excited silicon microcavity plasma devices*, *Appl. Phys. Lett.*, **86** 111501.

- [56] L Stenmark, M Lang, J Köhler, and U Simu, *Micromachined propulsion components*, Proc. 2nd Round Table on Micro/Nano Technologies for Space, ESTEC, Noordwijk, The Netherlands, ESA **WPP-132**, 69-76 (1997).
- [57] J Mueller, S Vargo, A Green, D Bame, R Orens and L Roe, *Development of a micro-isolation valve: Minimum energy requirements, repeatability of valve actuation and preliminary studies of debris generation*, AIAA Paper 2000-3675, 36th Joint Propulsion Conference, Huntsville, AL, (2000).
- [58] M Koch, N Harris, AGR Evans, NM White and A Brunnschweiler, *A novel micromachined pump based on thick-film piezoelectric actuation*, Sensors and Actuators A, **70**(1-2), 98-103 (1998).
- [59] C Haas and M Kraft, *Low-cost fabrication of valveless micropumps*, Proc. MME 2006 Conference, UK, 65-68 (2006).
- [60] CGJ Schabmueller *et al*, *Self-aligning gas/liquid micropump* J. Micromech. Microeng., **12**, 420-424 (2002).
- [61] CGJ Schabmueller, M Koch, AGR Evans and A Brunnschweiler, *Design and fabrication of a microfluidic circuitboard*, J. Micromech. Microeng., **9**, (1999).
- [62] H Sehr, AGR Evans, A Brunnschweiler, GJ Ensell and M Kraft, *A 3-dimensional actuator based on a novel combination of thermally actuated planar and vertical bimorphs*, Proc. 7th Int. Conf. On New Actuators, Bremen, Germany, 486 – 489 (2000).
- [63] KH Schoenbach, R Verhappen, T Tessnow, PF Peterkin and W Byszewski, Appl. Phys. Lett., **68**, 13 (1996).
- [64] YB Guo and FCN Hong, Appl. Phys. Lett., **82**, 337 (2003).
- [65] C Penache, A Braeuning-Demian, L Spielberger and H Schmidt-Boecking, Proc. of the Hakone VII, Greifswald, Germany, **2**, 501 (2000).
- [66] JW Frame and JG Eden, Electr. Lett., **34**, 1529 (1998).
- [67] JG Eden, SJ Park, NP Ostrom, ST McCain, CJ Wagner, BA Vojak, J Chen, C Liu, P von Allmen, F Zenhausern, DJ Sadler, J Jensen, DL Wilcox and JJ Ewing, J. Phys. D, **36**, 2869 (2003).
- [68] W Shi, RH Stark and KH Schoenbach, IEEE Trans. Plasma Sci., **27**, 16 (1999).
- [69] P von Allmen, DJ Sadler, C Jensen, NP Ostrom, ST McCain, BA Vojak and JG Eden, Appl. Phys. Lett., **82**, 4447 (2003).
- [70] P von Allmen, ST McCain, NP Ostrom, BA Vojak, JG Eden, F Zenhausern, C Jensen and M Oliver, Appl. Phys. Lett., **82**, 2562 (2003).
- [71] A Fiala, LC Pitchford and JP Boeuf, *Two-dimensional, hybrid model of glow discharge in hollow cathode geometries*, Proc. XXII Conf. Phenomena in Ionized Gases, Hoboken, NJ, **4**, 191 (1995).
- [72] SJ Park, JG Eden, J Chen and C Liu, *Microdischarge devices with 10 or 30 μ m square silicon cathode cavities: pd scaling and production of the XeO excimer*, Appl. Phys. Lett., **85**, 4869–4871 (2004).
- [73] MJ Kushner, J. Phys. D, **38**, 1633 (2005).
- [74] A Ketsdever, *System considerations and design options for microspacecraft propulsion systems*, in ‘Micropropulsion for Small Spacecraft’, Progress in Astronautics and Aeronautics, **187**, Chap. 4, (eds. M Micci and A Ketsdever), AIAA , Reston, VA, 139-163 (2000).
- [75] CM Marrese, *Compatibility of field emission cathode and electric propulsion technologies*, Ph.D. dissertation, University of Michigan, (1999).
- [76] RA Murphy, CT Harris, RH Matthews, CA Graves, MA Hollis, MA Kodis, J Shaw, M Garven, MT Ngo and KL Jensen, IEEE Int. Conf. on Plasma Science, San Diego, CA,, (1997).

- [77] CA Spindt and I Brodie, Technical Digest of the 1996 IEEE International Electron Devices Meeting (IEDM), 12.1.1 (1996); C. A. Spindt, C. E. Holland, P. R. Schwoebel, and I. Brodie, IEEE International Conference on Plasma Science, San Diego, CA, May 19-22, 1997.
- [78] MB Belikov, OA Gorshkov, RN Rizakhanov, AA Shagayda and SA Khartov, *Hall-type low and mean power thruster output parameters*, AIAA-99-2571, 35th AIAAJASMA/SAE/ASEE Joint Propulsion Conference and Exhibit, (1999).
- [79] JG Simmons, *Richardson-Schottky effect in solids*, Physical Review Letters, **15**(25), 967-968 (1965).
- [80] G Gaertner, D Raasch, D Barratt, S Jenkins, Appl. Surf. Sci., **215**, 72-77 (2003).
- [81] RW Springer and TW Haas, *Auger electron spectroscopy study of cathode surfaces during activation and poisoning*, J. Appl. Phys., **45**, 5260-5263 (1974).
- [82] JL Cronin, *Modern dispenser cathodes*, IEEE Proc., **128**, 19-32 (1981).
- [83] RE Thomas, JW Gibson, GA Haas and RH Abrams, *Thermionic sources for high-brightness electron beams*, IEEE Trans. Electr. Dev., **37**(3), 850-861 (1990).
- [84] KR Zavadil, DB King and JH Ruffner, *A novel thin film dispenser cathode for thermionic emission*, AIP Conf. Proc., **552**, 1165 (2001).
- [85] DM Goebel and RM Watkins, *LaB₆ hollow cathodes for ion and Hall thrusters*, AIAA-2005-4239, 41st Joint Propulsion Conference, Tucson, AZ, (2005).
- [86] MF Schatz. *Heaterless ignition of inert gas ion thruster hollow cathodes*, AIAA-85-2008, 18th International Electric Propulsion Conference, Alexandria, VA, (1985).
- [87] DM Goebel, JT Crow and AT Forrester, *Lanthanum hexaboride hollow cathode for dense plasma production*, Review of Scientific Instruments, **49**(4), 469-472 (1978).
- [89] DJ Willinst and RLF Boyd, *A study of the electron emission processes in a hollow cathode discharge*, J. Phys. D: Appl. Phys., **6** (1973).
- [89] DE Siegfried and PJ Wilbur, *A model for mercury orificed hollow cathodes: Theory and experiment*, AIAA Journal, **22**(10), 1405-1412 (1984).
- [90] L Rehn and HR Kaufman, *Correlation of inert gas hollow cathode performance*, AIAA Paper No. 78-707, (1978).
- [91] MJ Mandell and I Katz, *Theory of hollow cathode operation in spot and plume modes*, AIAA Paper No. 94-3134, (1994).
- [92] M Capacci, M Minucci and A Severi, *Simple numerical model describing discharge parameters in orificed hollow cathode devices*, AIAA Paper No. 97-2791, (1997).
- [93] L Spitzer Jr. , 'Physics of fully ionized gases', Interscience Publishers Inc., New York, (1956).
- [94] FW Crawford and JL Freeston, *The double sheath at a discharge constriction*, Proc. 6th Int. Conf. on Ionization Phenomena in Gasses, Paris, (1963).
- [95] FM Curran, A Sovie and TW Haag, *Arcjet nozzle design impacts*, JANNAF Propulsion Meeting, Cleveland, OH. (NASA TM-102050), (1989).
- [96] MW Crofton, *Evaluation of the United Kingdom ion thruster*, J. Spacecraft and Rockets, **33**(5), 739-747 (1996).
- [96] K.N.Leung, P.A. Pincosy, and K.W. Ehlers, "Directly heated lanthanum hexaboride filaments", Rev. Sci. Instrum., **55**,
- [97] Hutchison, K. G., 'Development of a Micro Hollow Cathode for use as a Ion Micro Propulsion Electron Source' PhD Thesis, University of Southampton, 2006
- [98] O. B. Postel and M. A. Cappelli , Appl. Phys. Lett., Vol. 76, No. 5, 31 January 2000

- [99] Sahli, A., Tirchi, P. J., 'Theoretical Modelling of Orificed Hollow Cathode Discharges' Paper 93-024, International Electric Propulsion Conference, Seattle, Washington, September 1993.
- [100] Sahli, A., Tirchi, P. J., 'Scaling Relations for Design and Operation of Orificed-Hollow Cathodes', AIAA-94-3133, 30th Joint Propulsion Conference, Indianapolis, IN, 1994.
- [101] Verheest, F., Hellberg, M., *Journal of Plasma Physics* (1997), 57:465-477 Cambridge University Press
- [102] Mandell, M.J. and Katz, I., "Theory of Hollow Cathode Operation in Spot and Plume Modes," AIAA Paper No. 94-3134, June 1994.
- [103] Doerner, R. P., Whyte, D. G., Goebel, D. M., 'Sputtering yield measurements during low energy xenon plasma bombardment, *Journal of Applied Physics*', pp. 8, Vol. 93, No. 91, May 1st 2003,

PART 2: MEMS PRODUCTION PROCESSES, DESIGN CONSIDERATIONS AND CONSTRAINTS

9. Introduction

When considering the basic sub-systems that comprise a micro-machined version of the standard hollow cathode thruster (*cf.* Figure 37), it is evident that it should be possible to design a prototype device where the fuel handling stage is not exposed to the high temperatures associated with the plasma propellant. Under these circumstances it would be logical to split the design into two, independently fabricated sub-systems: the propulsion system and the propellant storage and delivery system, which can then be later assembled into a single, gas-tight device. It may of course be possible to integrate the complete system into a single structure, but the anticipated high number of fabrication steps necessary to implement such a device could prove prohibitive. For example, a greater number of individual process stages would imply a greater degree of fabrication error (*e.g.* mask-alignment errors) with subsequent lower yield, potentially making the device uneconomical. With this in mind, the approach adopted here is to consider the entire system has two functionally independent entities and various strategies have been investigated toward their realisation. This approach also has the advantage that a number of different thruster designs can be investigated for suitability of purpose, with each integrateable upon a common propellant handling unit.

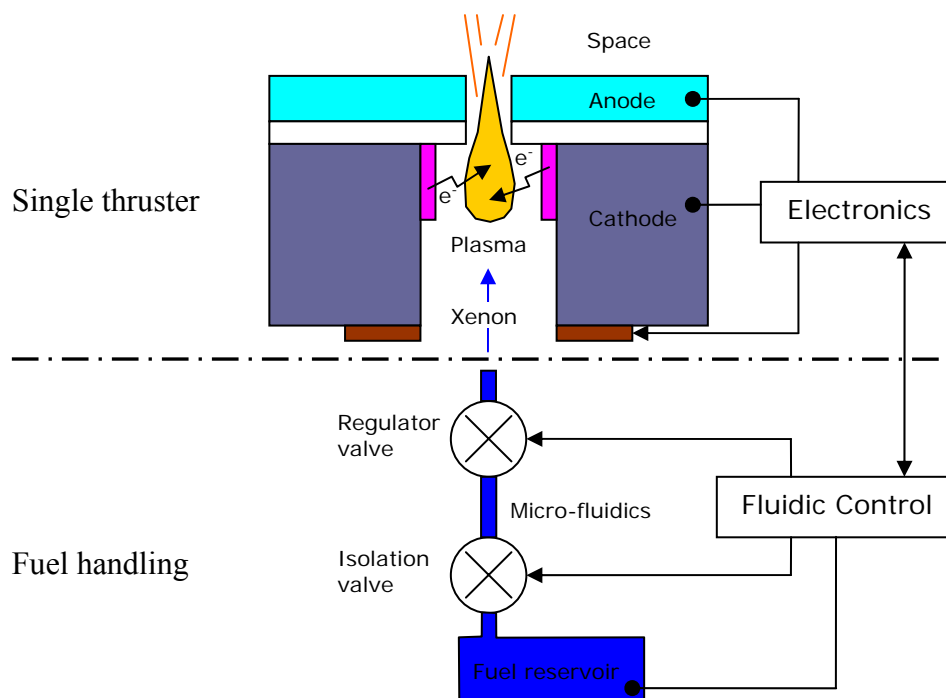


Figure 36 Basic sub-systems of a micro-mechanical hollow cathode thruster.

Although still somewhat nascent, the desire to produce micro-scale propulsion systems for space applications is by no means new [B1, B2]. A cursory review of the available literature reveals much

research in this area over the last decade in particular. Of the various techniques investigated, most fall within two categories based on the ignition of either solid propellants or liquid propellants, though the range of materials used to create these microstructures is quite broad. For example, in 2000 Lewis *et al* produced a MEMS micro-thruster array in silicon and glass that used a solid propellant (lead styphnate) which is ignited by electrically heating a resistive element [B3]. Expanding gases then rupture a thin membrane at the surface of the device to provide thrust with impulse of the order of 10^{-4} Ns. They estimate that upward of 1 million micro-thrusters can be produced on a single silicon wafer.

Rossi *et al* have demonstrated an array of 36 microthrusters fabricated in silicon that also use a heated solid fuel (glycidyle azide polymer, GAP) as the propellant source [B4]. In their research, they also investigate the influence of nozzle geometry on the performances of the thruster. The same team has also produced devices from machineable ceramics [B5]. Other solid fuel microthrusters include devices that use gunpowder [B6]. This particular design was fabricated using low-temperature co-fired ceramic technology and proved comparable with silicon-based systems.

Of the liquid propellant microthruster variations, the vaporising liquid microthruster has probably received the most attention. Mukerjee *et al* have demonstrated a system comprised of anisotropically wet-etched silicon bonded to Pyrex glass [B7]. Using water as a fuel, thruster force magnitudes ranging from 0.15 mN to a maximum force output of 0.46 mN depending on fabrication parameters (chamber length, nozzle geometry, heater power and liquid flow rates) were achieved. A similar design produced by Maurya *et al* consisting of two micromachined, bonded silicon chips produced thrusts in the range of $5 \mu\text{N}$ to $120 \mu\text{N}$ with a heater power of 1 W to 2.4 W using an exit nozzle of throat size $30 \mu\text{m} \times 30 \mu\text{m}$ [B8]. A maximum thrust of $120 \mu\text{N}$ was produced with a heater power of 2 W at a water flow rate of $0.7 \mu\text{l s}^{-1}$ with exit nozzle of throat size $50 \mu\text{m} \times 50 \mu\text{m}$.

Of the various spacecraft micropropulsion systems investigated, very little (if any) research appears to have been performed in the area of microthrusters based on hollow cathode structures. The majority of the work in this area has instead been aimed at plasma display devices. For example, Chen *et al* describes the microfabrication of hollow cathode plasma display devices in silicon which are shown to be able to work at much higher pressures (typically up to 1 atm) than their macro-scale counterparts [B9]. A more in depth review of emerging technologies in micropropulsion for space applications can be found in [B10].

As will be shown, the practical reality of fabricating a MEMS based hollow cathode thruster is not simply a matter of scaling down the physical dimension of a conventional device to micro-scales. Other factors such as choice of materials and processing techniques need to be considered. Consequently, before describing the methodologies, design variations and processes required in realising this objective, it is first worth reviewing the MEMS processes available for microfabrication, as detailed in the following section.

10. MEMS Design Considerations

An overview of the MEMS manufacturing processes mentioned in this section is given in the Appendix. In pursuing a MEMS-based solution for the fabrication of a hollow cathode microthruster, it is tempting as an initial trial to try and directly reproduce the conventional macro-scale device albeit at greatly reduced dimensions, as illustrated in Figure 38. As suggested in the previous section, the materials and processing techniques already exist to seemingly make this approach viable. However, even this simplified design has associated with it a number of possible variations and imposed constraints.

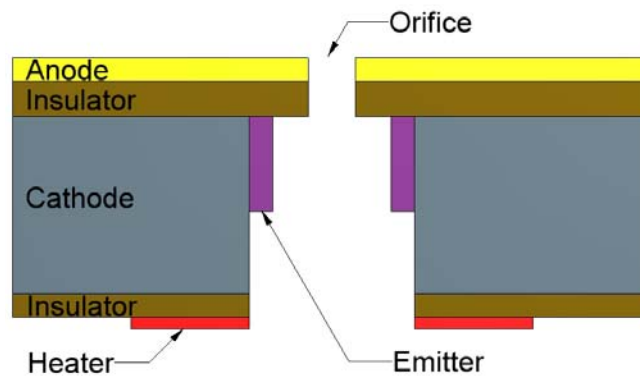


Figure 37 Cross-section through conceptual MEMS-based hollow cathode microthruster.

The first thing to note about this basic design is that it is composed of two electrically conductive sections (the cathode and anode) separated by an insulating layer. At least one of these conductive sections, preferably the cathode, would be fabricated in electrically conductive silicon (p-type or n-type). The other electrode layer can also be produced in silicon, though any of a large range of metals may also be a viable alternative. There is also a choice in the composition of the insulating layers, which can be produced from a number of different silicides (*e.g.* silicon dioxide, silicon nitride or silicon carbide). In choosing an appropriate insulator material, physical characteristics such as breakdown strength, thermal resistance and insulation resistance will need to be considered in conjunction with practical, achievable deposition thicknesses.

An obvious difference between this MEMS hollow cathode thruster and its macro-scale counterpart is the location of the heater element. It is not possible to place the heater concentrically around the cathode longitudinal axis in the MEMS version and so this has to be positioned at one end of the cathode structure. This instantly has implications on the amount of power that would be required to heat the emitter material to a temperature sufficient to initiate the thermionic emission of electrons. An obvious solution to help reduce this problem is to minimise the height of the cathode so that the heater is located as close to the emitter material as possible. However, this may not be practically possible: there will be a minimum thickness of silicon wafer that can be used in the design simply as a requirement imposed by mechanical handling considerations.

10.1. Scaling Issues

Unfortunately, when scaling down the physical dimensions of a conventional hollow cathode thruster (such as the Qinetiq T5) to the micromechanical level, certain fundamental parameters do not scale accordingly and in contrast have to be maintained. Typically, the body temperature of a standard hollow cathode thruster using xenon gas as the plasma fuel source and oxides of barium, calcium and aluminum impregnated within a porous tungsten insert as the thermal electron emitter lies between 1000°C and 1150°C [B19], which has implications on the choice of materials used in a micro-fabricated replica system. This single fact has the potential to be a ‘show-stopper’ in the realisation of a micro-fabricated hollow cathode thruster based solely on silicon technology, simply because this temperature range is not far from the melting point of silicon (1414°C [B20]). Indeed, conventional wisdom dictates that the maximum operating temperature for electronic devices fabricated from silicon should not exceed 300°C [B21]. Neudeck *et al* are even more cautious and state that practical operation of silicon power devices at temperatures above 200°C are problematic [B22]. Such guidelines are issued with respect to the consequences of temperature on the electrical properties of silicon devices such as charge carrier mobility and drift, changes to dopant concentration levels and changes in device resistance. However, such factors may not be of consequence here, where silicon is being used primarily as a mechanical element rather than as an electrical element. Nevertheless, the mechanical integrity of critical components of a silicon design

that are exposed to these high temperatures (*e.g.* the inner walls of the hollow cathode, the cathode aperture or the anode) may be compromised and therefore any practical design must accommodate for this.

Other scaling issues that are of importance include the fact that the surface-to-volume ratio of the hollow cathode plasma chamber increases when micro-fabricated, which leads to greater electron wall loss from the plasma with a corresponding adverse effect on thruster efficiency. Furthermore, components of the propulsion feed system may not lend themselves to miniaturisation at all. For example, given that the volume of a spherical propellant reservoir tank is proportional to the cube of its radius, any reduction in propellant mass and therefore containment volume has only a limited effect on the tank geometry. Such issues have been addressed by Ketsdever and Mueller, who provide a more thorough review of micropropulsion scaling issues [B23].

10.2. Base Material Selection

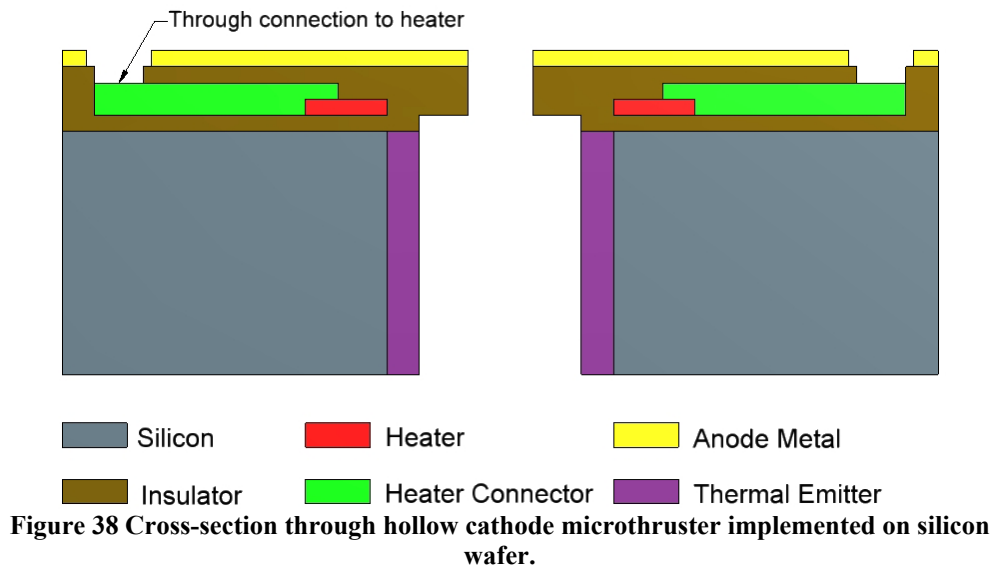
It is evident from Figure 38 that there is a clear demarcation between the MEMS processed structures associated with the cathode and those associated with the anode of a single microthruster. This would suggest that one method of implementation would be to fabricate these two distinctly different structures on two separate silicon wafers which can then be thermally (or otherwise) bonded together at a later stage. Though technically feasible, it is anticipated, however, that this approach would result in lower device yield due to alignment errors between both halves of an individual microthruster and is therefore not recommended. Fortunately, a more suitable type of silicon wafer for this type of microstructure exists. Known as a ‘Silicon on Insulator’ (SoI) wafer, this type of wafer comprises two layers of silicon, referred to as the handle wafer and the device wafer, separated by a silicon dioxide insulating layer. The two silicon layers usually have the same crystallographic orientation and electrical conductivity (*i.e.* contain the same dopant type and concentration), though customised versions can be obtained. The use of a SoI wafer in the fabrication of a microthruster has the obvious advantage that it removes two process steps, *viz* the deposition of the anode layer and electrode separating insulation layer.

SoI wafers are commercially available with a range of thicknesses for both the handle and device wafer as well as for the insulating layer. For example, Table 7 lists available thickness ranges from two typical suppliers.

Supplier	Wafer diameters	Device wafer	Insulator	Handle wafer
Silicon Quest International [B24]	100, 125, 150, 200	2 → 20 ± 1 21 → 100 ± 2	0.05 → 10 ± 5%	300 → 725 ± 15
Soitec [B25]	100, 150, 200, 300	0.34 → 1.5	0.1 → 3	375 → 775

Table 9 Wafer diameters (mm) and layer thicknesses (µm) of some ‘Silicon on Insulator’ wafers.

An alternative fabrication route is to use just a single silicon wafer to form the cathode structure and to then fabricate the anode from a metallisation layer deposited on the top surface of the wafer. This method would seemingly be simpler to fabricate and has the advantage that the heater element can be located closer to the emitter layer, at the orifice end of the hollow cathode structure, which is not possible with the SoI implementation. With this arrangement, it would be necessary to open a window in the anode layer to permit electrical connection to the underlying heater, as illustrated in the conceptual design shown in Figure 39. Whether this buried metal layer within the insulator that separates cathode from anode will affect the electrical field between these electrodes is yet to be established.



The alternative implementation for the heater circuit is to use two materials with different resistivities: a low resistivity for the connecting track and a higher resistivity for the actual heater element. For the latter, polysilicon is the material of choice, having resistivities in the range 10^{-3} to 10^{-5} Ohm-m (dependant on dopant type and concentration), exhibiting a strong bond with silicon and its silicides and being compatible with MEMS processing techniques [B27-B31]. In fact polysilicon has precedence for its use as a heater element in nearly all microfabricated vaporising liquid thrusters [B5-B8].

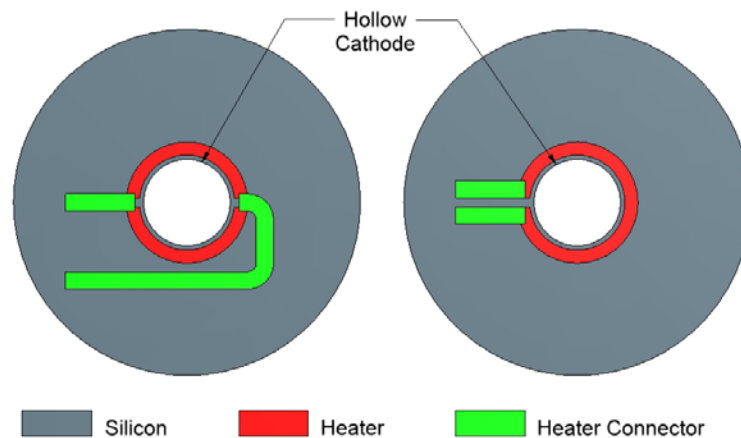


Figure 40 shows two different arrangements for producing the heater element when two different materials are employed for the heater and connecting tracks. In both configurations, it is assumed that the heater material has been deposited on the silicon surface first and that the connecting tracks are then deposited on to the silicon with a small portion overlapping the heater material in order to make an electrical contact. The figure shows that in both instances the heater element has a circular profile and is positioned at the base of the hollow cathode structure, entirely about its perimeter and concentrically aligned with the cathode longitudinal axis. The picture on the right shows the heater element with a single track break allowing both connecting tracks to be positioned on the same side of the design. Current passes in a continual flow around the heater element. That on the left shows the heater element split symmetrically across a diameter such that the current is divided and passes in equal proportions around both semi-circular elements. This arrangement allows the connectors to

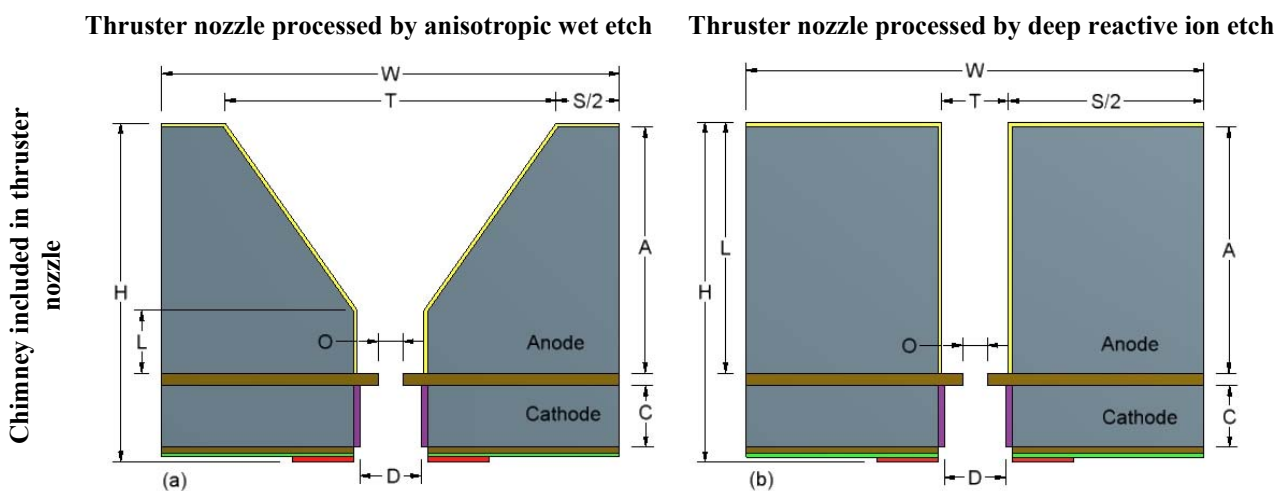
be positioned on opposite sides of the heater. If more than one thruster is to be produced as part of a propulsion unit, each will require a separate heater element. In this situation, individual heater elements should not be connected in series, but rather in parallel with the connector tracks serving as ‘drop-offs’ from two master power bus lines. This prevents the potential problem associated with series connected systems whereby a single track break in a power supply connector effectively removes power from every single device.

10.3. Generic Design Geometries

Taking the silicon on insulator fabrication route as an example and taking into consideration the conventional silicon processing techniques available and described previously, a number of generic micro-scaled structures can be imagined, as shown in Figure 41. In formulating these designs, three binary-weighted design options have been included, namely:

- Forming the thruster nozzle by an anisotropic etching method (slanted sidewalls, square profile) or by a deep reactive ion etching method (straight sidewalls, circular profile). [Forming the thruster nozzle by isotropic etching has been discarded since geometries of sidewalls cannot be reliably predicted *a priori*.]
- The inclusion or absence of a ‘chimney’ structure within the thruster nozzle.
- The inclusion or absence of an orifice at the hollow cathode end-plate.

Other variants on these basic generic designs can also be considered where, for example, the diameter of the thruster chimney (if present) is different to the internal diameter (D) of the hollow cathode. Each of these generic designs has relative merits and shortcomings that effect different aspects of the system as a whole.



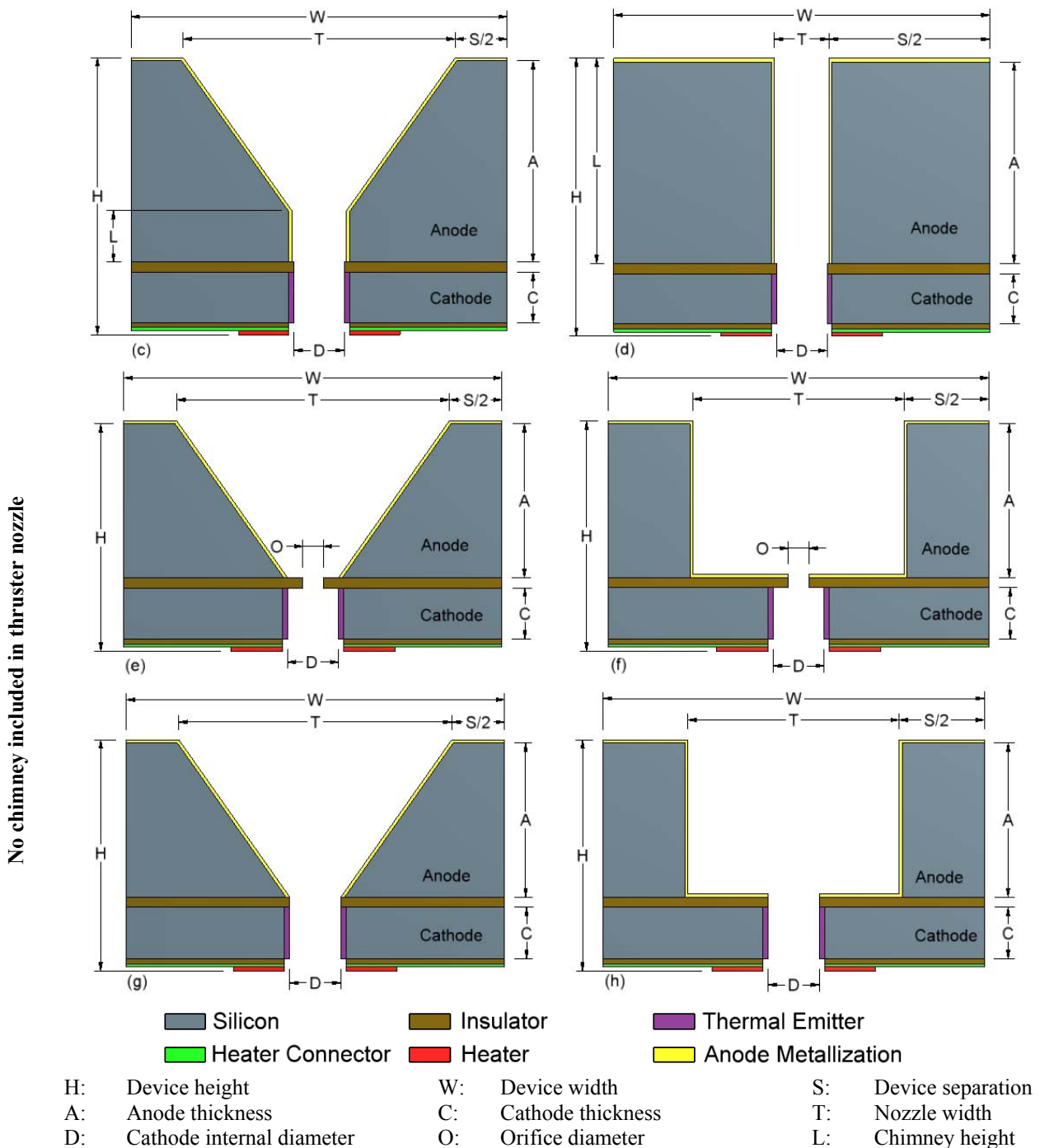


Figure 40 Generic variations for MEMS microthruster devices fabricated using a SoI wafer (not to same scale).

As previously mentioned, to ensure safe and simple handling of the silicon wafers during processing, as well as ensuring the mechanical integrity of the processed devices, there will be a minimum overall thickness for the SoI wafer used for fabrication. As an example, Table 10 shows that the minimum thickness of the handle wafer is of the order of 300 microns. This will have repercussions on the minimum geometries of each of the generic device versions illustrated in Figure 41. In particular, the fixed angle of the sloping walls that define the thruster nozzle of the anisotropically wet etched devices (54.7°) means that the nozzle throat width, T , and the overall device width, W , are directly related to the anode thickness, A . The same is not true, however, of those devices where the nozzle in the anode is fabricated using the deep reactive ion etching technique, since here the nozzle throat width is entirely independent of the anode thickness. Clearly, for a given thickness of anode layer, a greater packing density of microthruster devices can be

achieved for designs where the thruster nozzle is formed by the deep reactive ion etching technique than for those where the nozzle is formed by anisotropic wet etching.

This raises the design question as to whether the majority of the thickness of the SoI wafer should be utilised in the construction of the anode layer or the cathode layer. Put more simply, which half of the design should be rendered from the handle wafer? Intuitively, the answer would seem obvious: increase the thickness of the cathodic region at the expense of a thinner anode, so that devices with nozzles etched by either technique can attain larger packing densities on a single wafer. However, because the heater element can only be located at the end of the cathode structure distal to the orifice, a thicker cathode would require a greater amount of electrical power to be supplied to the heater element to raise the temperature in the hollow cathode sidewalls to that necessary for thermal electron emission. Evidently then, a design trade-off exists, which may negate the use of one or more of the generic designs illustrated depending upon the packing densities of individual thrusters required.

It should be noted though that the inclusion of a chimney structure in the anisotropically etched thruster nozzle will reduce the influence the anode thickness has on the overall device width and hence on the maximum packing density. This point is clearly illustrated in Table 10 which shows minimum thruster device widths for anisotropically etched thruster nozzles based on an arbitrary anode thickness (A) of 300 microns and fixed spacing (S) of 10 microns, as a function of the ratio of chimney height to cathode internal diameter (L:D) of 20:1, 10:1, 1:1 and 0 (*i.e.* no chimney).

D = 5 μm		D = 10 μm		D = 15 μm		D = 20 μm	
L μm	W μm	L μm	W μm	L μm	W μm	L μm	W μm
0	434.8	0	434.8	0	434.8	0	434.8
5	427.7	10	420.7	15	413.6	20	406.5
50	364.0	100	293.2	150	222.4	200	151.6
100	293.2	200	151.6	300	N/A	400	N/A

Table 10 Minimum device widths (W) for thruster nozzles with chimneys fabricated by anisotropic etching as a function of hollow cathode internal diameter (D) and chimney length (L).

Table 10 shows that for the parameters given, the minimum width of a thruster that incorporates a chimney structure and whose thruster nozzle has been formed by anisotropic wet-etching, ranges from approximately 150 microns to just over 430 microns depending on the length of the thruster chimney, with larger chimneys resulting in the lower device widths. By comparison (and using the same parameter values), the minimum width of a thruster with chimney and nozzle formed by deep reactive ion etching can be as low as 10 microns. Clearly anisotropically etched nozzles result in larger inter-device separation distances (*i.e.* lower packing densities). While this may appear to be a disadvantage, there are good reasons why wet-etched nozzles should not be disregarded off-hand. Chief amongst these is the fact that the anisotropically wet-etched nozzle presents a greater surface area for ion collection at the anode surface than its deep reactive ion etched counterpart. This may significantly help to reduce the detrimental effect of charged ions and particles contained within the emergent plasma charging the external surface of the spacecraft. Additionally, the sloping sidewalls of the wet-etched nozzle allow the plasma plume to spread laterally on egress without interference. Finally, from a production perspective, wet-etch processes are relatively simple procedures that can be performed in the laboratory without the need of specialist, expensive equipment and etch rates are well defined, relying solely on etchant temperature, etchant concentration and etch time.

11. Micro-Thruster Body Designs

To avoid the potential ‘show-stopper’ situation attributable to the propellant plasma operating temperature being comparable with or higher than the melting point of the material from which the hollow cathode thruster is fabricated and thereby affecting mechanical structural integrity, a number of different design strategies have been investigated where this problem should be reduced or negated. Of these, three different design philosophies have been identified as offering the safest mitigation routes, whilst still being practicable, namely:

- A device based on silicon and using conventional thermal emitter materials with their concomitant high temperature plasma, but where critical and exposed regions of the silicon construction have been sufficiently thermally insulated to prevent structural damage.
- A device based on silicon using a thermal emitter material of lower work function, such that the plasma is initiated and sustained at an operating temperature well below the melting point of silicon.
- A device based on a different micro-machineable material as the underlying structure with a higher melting point than silicon.

Other design philosophies have also been investigated, no matter how esoteric or unconventional they may seem at present. Included here is the concept of using a porous silicon structure as a matrix to support a barium-calcium-aluminate impregnate for the emitter layer. Such a structure would be the closest in design to the conventional T5 hollow cathode thruster, but is reliant on the plasma temperature not affecting the mechanical integrity. Other alternative designs considered include techniques of initiating a plasma that do not involve the bombardment of the fuel with energetic, thermally emitted electrons. For example, coupling the energy from an RF source into the cathode core or by using electrons emitted from ferroelectric materials. The relative merits and deficiencies of each of these approaches are described in more detail in the following sections.

Some of these concepts and designs may prove to be technically unfeasible with the current state of technology. However, with rapid advances in materials science and in processing techniques within the microfabrication sector, what may be unworkable today may well be possible in the near future. Accordingly, these designs should not be discarded but explored to identify their limiting aspects.

11.1. Thermally Insulated Devices

Silicon as a substrate material (and by extension, SoI wafers) may present mechanical integrity issues when subjected to the proposed plasma temperatures which could be as high as 1150°C. The melting point of silicon is 1414°C and so whilst we may not expect it to melt, there may be other structural and electrical issues to consider. For example, it is likely that the distribution of dopants dispersed within the silicon will be altered with concomitant effect on electrical conductivity. Furthermore, the high energy, ion rich environment in which these structures will operate could also adversely affect electrical properties (*e.g.* through self-doping). With this in mind, a prudent route to fabrication would be to thermally insulate critical, exposed parts of the silicon structure. However, this can bring about a dichotomy: one of the surfaces that would be exposed to high temperatures is the inner sidewall of the hollow cathode region and protecting this with a thermal insulator (implied low thermal conductivity) would mean that more power would be required to heat the overlying emitter layer than if this thermal insulator were not present.

Materials that could be used in this rôle that are also compatible with microfabrication techniques are the silicides: silicon carbide (SiC); silicon nitride (Si_3N_4) and silicon dioxide (SiO_2). The latter two of these materials are routinely used to electrically insulate silicon in the construction of electronic devices and should therefore present no problems in their incorporation into a thruster design, providing that the surfaces to be coated are readily accessible. Additionally, silicon carbide and silicon nitride coated silicon structures have also been shown to be more sputter resistant than silicon [B32] and therefore can prolong the life of structural parts which would otherwise be eroded by ions in the plasma impinging on unprotected surfaces.

Depending upon how these materials are formed, their thermal properties can be quite different. For example, silicon carbide is reported as having a melting point in the range 2650°C to 2950°C [B33]. Reaction bonded silicon carbide has a thermal conductivity of $150\text{-}200 \text{ Wm}^{-1}\text{K}^{-1}$ and a recommended upper continuous use working temperature of 1350°C . By comparison, hot pressed silicon carbide has a thermal conductivity of $90\text{-}160 \text{ Wm}^{-1}\text{K}^{-1}$ and an upper continuous use working temperature of $1500\text{-}1650^\circ\text{C}$. Silicon nitride decomposes at temperatures above 1900°C , though its recommended upper continuous working temperature range is lower at $1200\text{-}1500^\circ\text{C}$. The thermal conductivity of silicon nitride is given as $10\text{-}16 \text{ Wm}^{-1}\text{K}^{-1}$ for the reaction bonded form and $15\text{-}43 \text{ Wm}^{-1}\text{K}^{-1}$ for the hot pressed form [ibid.]. Silicon dioxide has a melting point of approximately 1600°C and a recommended upper continuous use working temperature of $900\text{-}1200^\circ\text{C}$. Its thermal conductivity is over an order of magnitude lower than the other two silicides, lying in the range $1.2\text{-}1.4 \text{ Wm}^{-1}\text{K}^{-1}$ [ibid.].

As with the case for Section 3.4, a number of different design geometries can be fabricated, but for convenience, just two representative designs are shown in Figure 42.

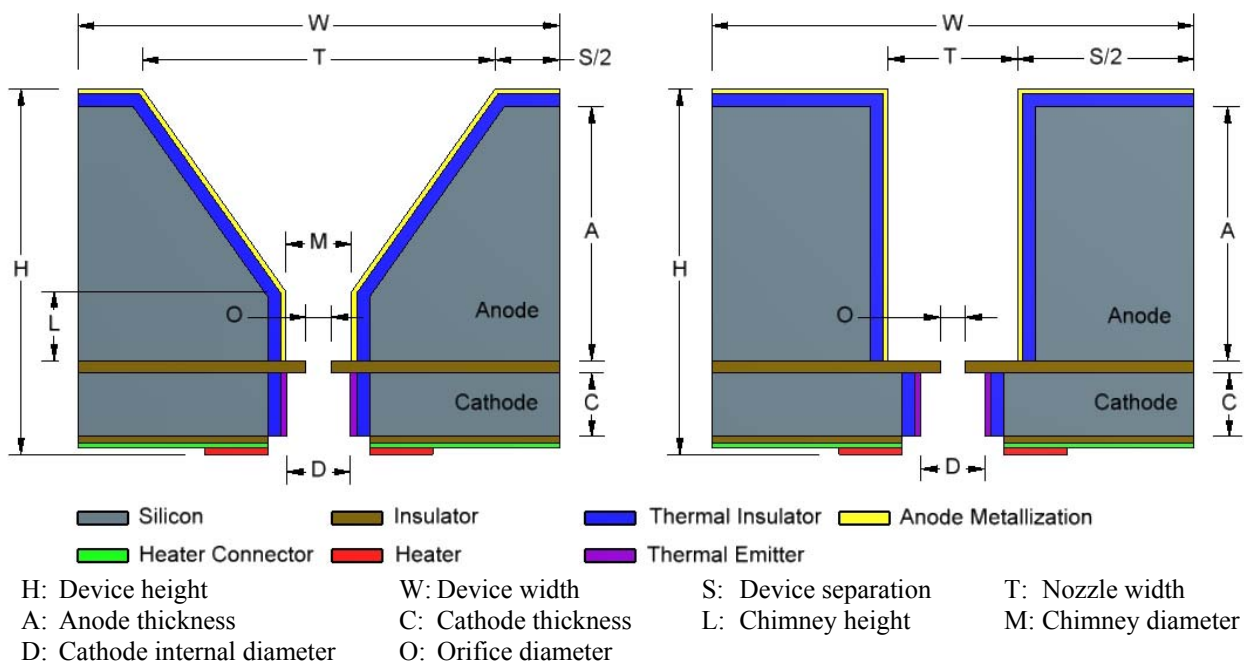


Figure 41 Examples of thermally insulated silicon microthrusters. Left – thruster nozzle formed by anisotropic wet-etch and incorporating a chimney structure. Right – thruster nozzle formed by deep reactive ion etching and having no chimney structure.

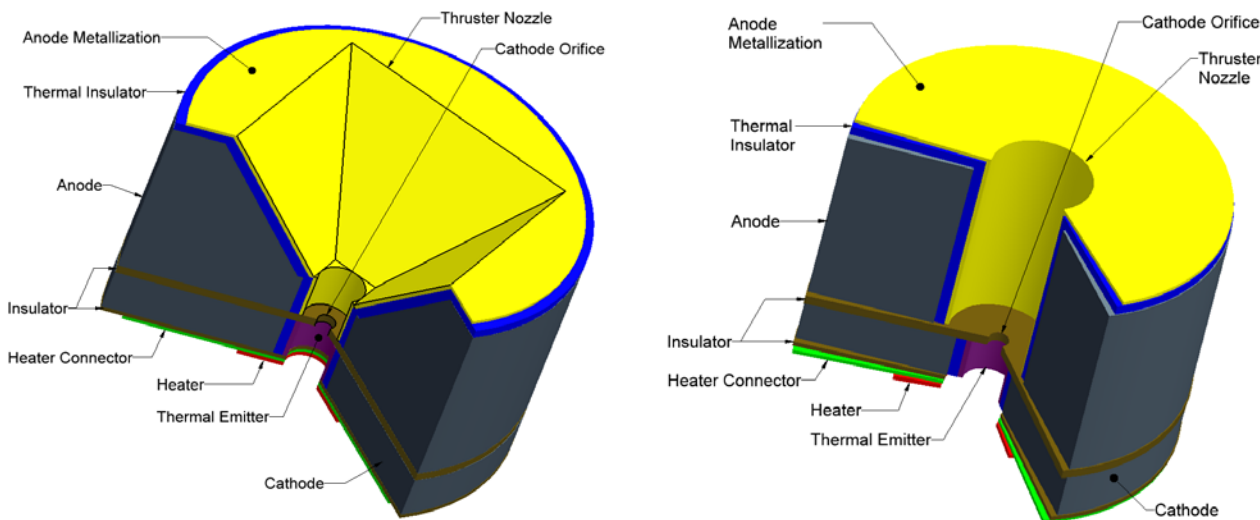


Figure 42 Cut-away isometric views of single thrusters depicted in Figure 42.

Figure 43 reinforces the fact that the anisotropically etched thruster nozzle is more dependant on the crystallography of the silicon substrate than the reactive ion etched nozzle, producing an inverted pyramidal cut-out where the etch process is naturally stopped by four $\{111\}$ planes. By comparison, the reactive ion etched nozzle can take any geometry, but here, merely as an example, is shown to be cylindrical and concentric about the cathode orifice.

There are a number of processing techniques by which layers of SiO_2 can be produced, including chemical vapour deposition, sputtering, epitaxial growth and through thermal oxidation of the bare silicon surface. Of these, it has been observed that the resistivity of thermally oxidised SiO_2 is twice or three times as high as that of SiO_2 films deposited by other means [W13]. This would appear to suggest that thermal oxidation would be the preferred processing method since electrical insulation properties should be maximised. However, it has also been reported that relatively large insulator thicknesses for SiO_2 can be obtained by low temperature oxide chemical vapour deposition (up to about 5 microns) compared to other film deposition techniques, giving (by virtue of the greater thickness) larger breakdown electric field strengths of the order of $600\text{-}700\text{ V}/\mu\text{m}$ and stand-off voltages of the order of 3 kV [B1].

11.2. Low Work Function Devices

If an electron emission material with a lower work function than the barium-calcium-aluminate impregnated tungsten used in the conventional T5/T6 hollow cathode thruster can be found that is compatible with MEMS processing, then it may be possible to initiate and sustain a propellant plasma at a much lower operating temperature. For example, mixed metal matrix cathodes such as porous tungsten-iridium have a work function between 0.20 and 0.25 eV lower than impregnated tungsten, which reduces the temperature by up to 100°C for a given emission current density [W1]. This in turn may permit standard silicon wafers to be used as the underlying material for the structure. Suitable materials with lower work functions are likely to include the alkali metals, transition metal borides, transition metal nitrides and caesium salts [X4]. Providing that these materials can be processed using standard (or slightly modified) microfabrication techniques, generic examples of how they could be incorporated as electron emitters within a MEMS microthruster structure are illustrated in Figures 44 and 45.

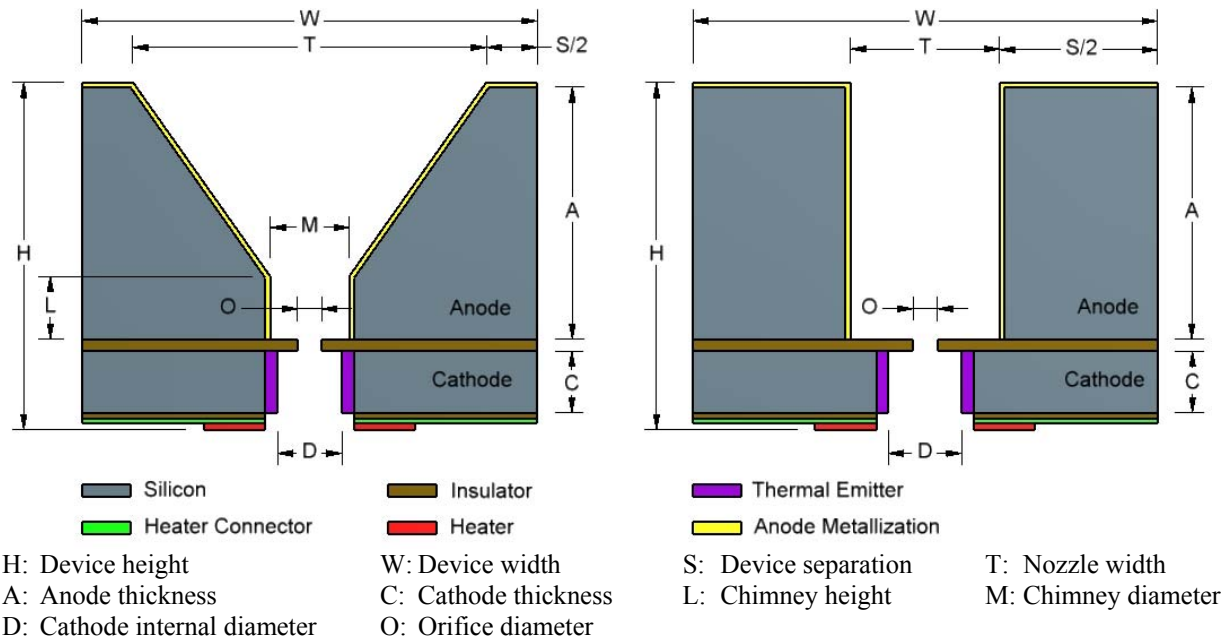


Figure 43 Examples of microthrusters with low work function thermal emitters. Left – thruster nozzle formed by anisotropic wet-etch and incorporating a chimney structure. Right – thruster nozzle formed by deep reactive ion etching and having no chimney structure

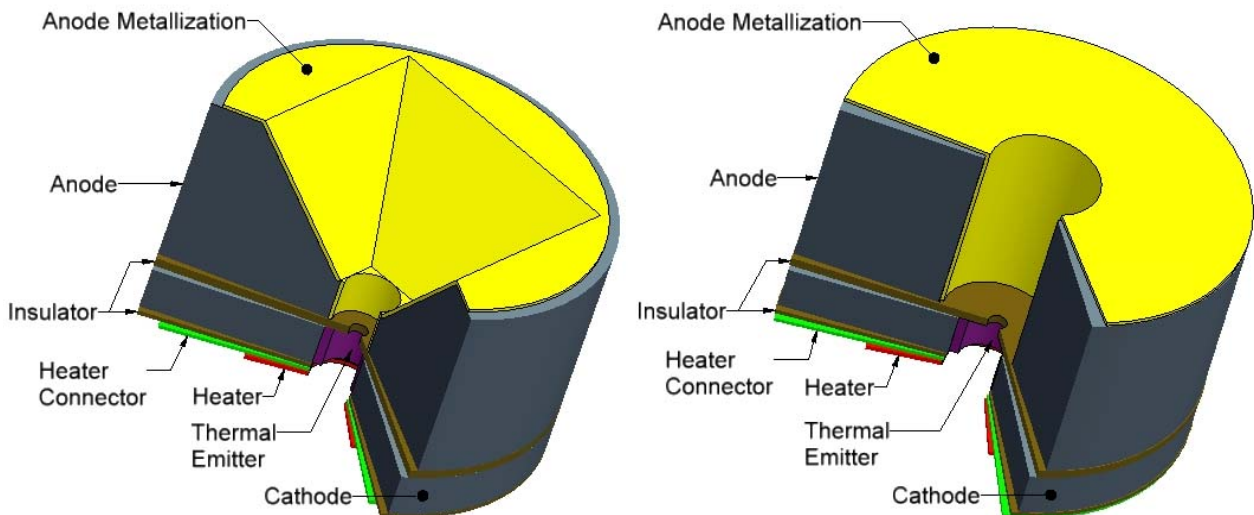


Figure 44 Cut-away isometric views of single thrusters depicted in Figure 43

Depending on the nature, composition and form of the material used as the thermal emitter, an additional seed layer may need to be deposited on the silicon surface to be coated to promote adhesion of the former to the latter.

11.2.1. Lanthanum Hexaboride (LaB₆)

Lanthanum hexaboride has a very low work function for thermionic electron emission and this property together with a low rate of evaporation and superior operating lifetime makes LaB₆ very attractive as a filament material [W2, W3, W4]. Indeed, it has for some time now been used as a protective coating on electron guns [B19] and in particular, as a coating for the tips in scanning electron microscopes [W5, W6]. It is therefore not surprising that it has been considered and trialed

as an electron emission source in both thermionic cathode and cold cathode applications [W7, W8, W9].

Lanthanum hexaboride and its homogeneity range has been studied intensely during the last few years, partly due to its increased industrial use as a high-performance thermionic emitter in electron beam instruments. The literature shows that it can be deposited using a variety of different, standard microfabrication techniques. It is commercially available in powder form of high purity as well as in rod, bar, disc, pellet and slab geometries (*cf.* for example [W10, W11, W12]). Reported values for work function when deposited as a film vary widely, spanning some 2.3 to 2.9 eV depending on material stoichiometry [W2, W7, W8, W13], crystallographic orientation [W14], deposition technique [W15, W16] and on the composition of the supporting metal [W17]. Early reports on the homogeneity range of lanthanum hexaboride were conflicting. Using microscopy and density measurements, Johnson and Daane found that the homogeneity range extends from LaB_{6.0} to LaB_{7.8} [W18]. They did not observe any cell dimension variation within the range of homogeneity but a change in the colour of LaB₆ was noted: the hexaboride is purple for stoichiometric composition and blue for boron-rich compositions.

In a report commissioned by NASA on the use of composite refractory compounds as thermionic converters, Swanson *et al* [W9] reported the thermionic work function of the {100} face of LaB₆ to be around 2.47 eV, but cautioned that this could increase by as much as a further 1.6 eV due to oxygen adsorption at the film surface. Whilst this may not be a problem in a space environment, the implications do need to be considered with regard to the state of the material pre-launch (*e.g.* whether some form of temporary hermetic sealing of the thrusters needs to be included). On a positive note, the authors also showed that the work function could be reduced to 1.39 eV through the adsorption of a partial monolayer of caesium, which is very promising for lower plasma temperature operation.

Some of the various techniques reported in the literature for depositing films of LaB₆ that could be adopted in a MEMS application are briefly reviewed below.

The electrochemical deposition of thin films of LaB₆ onto the surface of ionisation gauge filaments has been described as early as 1966 [W15], with successful coatings on metal filaments of tungsten, rhenium and molybdenum. A value for the work function of 2.56 eV was reported. The different metal filaments showed similar characteristics, differing only in the lifetime of the LaB₆ coating, attributed to variations in the rate of diffusion of boron into the filaments and therefore of evaporation of the lanthanum.

Wang *et al* report on the field emission characteristics of micromachined silicon tips coated with lanthanum hexaboride by electron-beam evaporation [W16]. Using molybdenum as a seed layer to promote adhesion of the LaB₆ films to the silicon tips, they conclude that the quality of the resultant films depends primarily upon the temperature of the silicon substrate (which significantly affects the stoichiometry and the crystallinity of the deposited film) and to a lesser extent on the beam evaporation power. Their results showed that when the substrate temperature was low, the adhesion between the silicon tip surface and the LaB₆ film became poor. Investigations revealed that best results were obtained at a substrate temperature of 300°C. Experiments performed with the coated tips show that compared to pure silicon and molybdenum coated silicon, higher emission currents were attainable, field emission stability was superior and the devices exhibited improved immunity to vacuum environments. By contrast, however, in their work on sintered lanthanum hexaboride, Pelletier and Pomot [W17] warn that the work function is highly susceptible to poisoning by contamination of the emitting surface by molybdenum vapour at high temperatures (above 1400K), raising the measured value from 2.36 eV to 2.7 eV.

Okamoto *et al* [W14] also used the electron-beam evaporation technique to deposit LaB₆ thin-films, but in their investigation opted to use nickel as the substrate material. They observed that the work function of the resultant film was dependant on its crystallographic orientation when deposited and achieved the lowest value of between 2.4 to 2.5 eV for the {100} orientation.

Craciun and Craciun investigated the deposition of LaB₆ films using the pulsed laser deposition technique [W19]. Their investigations found that crystalline films could only be grown on p-type {100} silicon wafers by using a KrF excimer laser fluence around 10 J/cm² or higher and for a substrate temperatures in excess of 800°C. Analysis by X-ray photoelectron spectroscopy (XPS) and Auger electron spectroscopy (AES) showed that the outermost layers of the deposited films contained significant amounts of oxygen and La-O and B-O bonds, though this could be reduced to below 10% by removing the surface region by sputtering.

Schmidbauer *et al* demonstrated that films of LaB₆ can be deposited on the surface of a heated {100} silicon substrate by both reactive and non-reactive d.c. arc deposition [W20]. Using, commercially available discs of LaB₆ with a porosity of 13% and purity of 99.5% as the source material, films with thickness up to 1.5 µm were successfully deposited in a low-pressure nitrogen background. Subsequent analysis of the deposited films revealed them to consist of a matrix phase in which macroparticles of polycrystalline LaB₆ with a size of the order of 1 µm were embedded, with the matrix phase consisting mainly of lanthanum and boron together with some carbon and oxygen from the residual gas. It is not clear whether the polycrystalline nature of this film would result in localised emission characteristics rather than homogenous emission across the entire film surface area.

Mroczkowski used magnetron sputtering to deposit a thin film of lanthanum hexaboride on to a tungsten substrate [W21]. The work function and electron emission characteristics of the coating were studied and after optimising sputtering parameters, a value for the work function of between 2.4 and 2.6 eV was determined. At 1200 K the emission density of a lanthanum hexaboride coated tungsten filament was measured as being 8.8 mA/cm², which was far in excess of that recorded for a clean tungsten filament at 9.7x10⁻¹² A/cm². Furthermore, coated tungsten filaments ran over 1000 hours without any reduction in the emission current in a vacuum of 10⁻⁷ Torr, and after an initial activation, were exposed to the atmosphere without any subsequent reduction in emission current density.

12. Conclusion

As has been shown the practical reality of fabricating a MEMS based hollow cathode thruster is not simply a matter of scaling down conventional devices. Manufacture on a wafer for example limits the possible geometries based on the range of possible processing technique to achieve the end result of which each play a significant role. The various methodologies have been reviewed and as have the possible design variations and processes required in realising this objective. MEMS-based solutions will not be able to reproduce conventional geometries however the study has shown that it should at least be feasible to produce device conducent to a functional thruster.

The operating temperature has implications on the choice of materials used in a micro-fabricated replica system. This single fact has the potential to be a 'show-stopper' in the realisation of a micro-fabricated hollow cathode thruster based solely on silicon technology, simply because this temperature range is not far from the melting point of silicon (1414°C).

An obvious difference between this MEMS hollow cathode thruster and its macro-scale counterpart is the location of the heater element. It is not possible to place the heater concentrically around the thruster body so it must be produced as a track on the wafer itself. The use of a SoI wafer in the fabrication of a microthruster has the obvious advantage that it removes two process steps, *viz* the deposition of the anode layer and electrode separating insulation layer cathode longitudinal axis. This type of wafer comprises two layers of silicon, referred to as the handle wafer and the device wafer, separated by a silicon dioxide insulating layer. An alternative fabrication route is to use just a single silicon wafer to form the cathode structure and to then fabricate the anode from a metallisation layer deposited on the top surface of the wafer. This method would seemingly be simpler to fabricate and has the advantage that the heater element can be located closer to the emitter layer, at the orifice end of the hollow cathode structure, which is not possible with the SoI implementation. With this arrangement, it would be necessary to open a window in the anode layer to permit electrical connection to the underlying heater.

Taking the silicon on insulator fabrication route as an example and taking into consideration the conventional silicon processing techniques available and described previously three binary-weighted design options have been included, namely:

1. Forming the thruster nozzle by an anisotropic etching method (slanted sidewalls, square profile) or by a deep reactive ion etching method (straight sidewalls, circular profile)
2. The inclusion or absence of a ‘chimney’ structure within the thruster nozzle
3. The inclusion or absence of an orifice at the hollow cathode end-plate.

The minimum thickness of the handle wafer required has been shown to be of the order of 300 microns. This will have repercussions on the minimum geometries of each of the generic device versions illustrated in Figure 8. In particular, the fixed angle of the sloping walls that define the thruster nozzle of the anisotropically wet etched devices (54.7°) means that the nozzle throat width, T , and the overall device width, W , are directly related to the anode thickness. The same is not true, however, of those devices where the nozzle in the anode is fabricated using the deep reactive ion etching technique, since here the nozzle throat width is entirely independent of the anode thickness. Clearly, for a given thickness of anode layer, a greater packing density of microthruster devices can be achieved for designs where the thruster nozzle is formed by the deep reactive ion etching technique than for those where the nozzle is formed by anisotropic wet etching. In the case of the SoI the handle layer can take the form of the cathodic or anode layer. Since the heater should be located close to the emitter it would seem intuitive to use the anode later as the handle and locate the heater directly behind the emitter on the rear of the wafer.

To avoid the potential ‘show-stopper’ situation attributable to the propellant plasma operating temperature being comparable with or higher than the melting point of the material from which the hollow cathode thruster is fabricated and thereby affecting mechanical structural integrity, a number of different design strategies have been investigated where this problem should be reduced or negated. Of these, three different design philosophies have been identified as offering the safest mitigation routes, whilst still being practicable, namely:

4. A device based on silicon and using conventional thermal emitter materials with their concomitant high temperature plasma, but where critical and exposed regions of the silicon construction have been sufficiently thermally insulated to prevent structural damage.
5. A device based on silicon using a thermal emitter material of lower work function, such that the plasma is initiated and sustained at an operating temperature well below the melting point of silicon.
6. A device based on a different micro-machineable material as the underlying structure with a higher melting point than silicon.

Finally lanthanum hexaboride has been proposed as an emitter solution to present a lower the work function surface for the reduction of operating temperature and discharge voltage. The literature shows that it can be deposited using a variety of different, standard microfabrication techniques. It is commercially available in powder form of high purity as well as in rod, bar, disc, pellet and slab geometries. The properties and homogeneity range has been studied intensely during the last few years, partly due to its increased industrial use as a high-performance thermionic emitter in electron beam instruments.

13. References

- [B1] J Mueller, I Chakraborty, S Vargo, C Marrese, V White, D Bame, R Reinicke and J Holzinger, *Towards micropropulsion systems on-a-chip: Initial results of component feasibility studies*, Proc. IEEE Aerospace Conference, **4**, 149-168 (2000).
- [B2] EJ Lerner, *Plasma propulsion in space*, The Industrial Physicist, **6**, 16-19 (2000).
- [B3] DH Lewis Jr, SW Janson, RB Cohen and EK Antonsson, *Digital micropropulsion*, Sensors and Actuators A, **80**, 143-154 (2000).
- [B4] C Rossi, T Do Conto, D Est`eve and B Larangot, *Design, fabrication and modelling of MEMS-based microthrusters for space application*, Smart Mater. Struct., **10**, 1156–1162 (2001).
- [B5] C Rossi, B Larangot, D Lagrange and A Chaalane, *Final characterizations of MEMS-based pyrotechnical microthrusters*, Sensors and Actuators A, **121**, 508-514 (2005).
- [B6] KL Zhang, SK Chou and SS Ang, *Development of a low-temperature co-fired ceramic solid propellant microthruster*, J. Micromech. Microeng., **15**, 944-952 (2005).
- [B7] EV Mukerjee, AP Wallace, KY Yan, DW Howard, RL Smith and SD Collins, *Vaporizing liquid microthruster*, Sensors and Actuators, **83**, 231-236 (2000).
- [B8] DK Maurya, S Das and SK Lahiri, *Silicon MEMS vaporizing liquid microthruster with internal microheater*, J. Micromech. Microeng., **15** 966-970 (2005).
- [B9] J Chen, SJ Park, Z Fan, J.G Eden and C Liu, *Development and characterization of micromachined hollow cathode plasma display devices*, J. Microelectromechanical Sys., **11**(5), 536-543 (2002).
- [B10] C Rossi, *Micropropulsion for space – A survey of MEMS-based micro thrusters and their solid propellant technology*, Sensors Update, **10**(1) 257-292 (2002).
- [B11] J Frühauf and S Krönert, *Wet etching of silicon gratings with triangular profiles*, Microsyst. Technol., **11**, 1287-1291 (2005).
- [B12] D Resnik, D Vrtacnik, U Aljancic, M Mozek and S Amon, *Different aspect ratio pyramidal tips obtained by wet etching of (100) and (111) silicon*, Microelectronics Journal, **34**, 591-593 (2003).
- [B13] S Janson, H Helvajian, S Armmoto, G Smit, D Mayer and S Feuerstein *Microtechnology for Space Systems*, Proc. IEEE Aerospace Conference, **1**, 409-418 (1998).
- [B14] LA Woldering, AM Otter, BH Husken and WL Vos, *Focused ion beam milling of nanocavities in single colloidal particles and self-assembled opals*, Nanotechnology, **17**, 5717-5721 (2006).
- [B15] M Henry, PM Harrison, I Henderson and M Brownell, *Laser milling – A practical industrial solution for machining a wide variety of materials*, [Where?](#)
- [B16] DT Pham, SS Dimov, PV Petkov and T Dobrev, *Laser milling for micro tooling*, [Where?](#)

- [B17] SL Campanelli, AD Ludovico, C Bonserio, P Cavalluzzi and M Cinquepalmi, *Experimental analysis of the laser milling process parameters*, J. Materials Processing Technologies, **191**, 220-223 (2007).
- [B18] J Wang, Y Gong, G Abba, J Cao, J Shi and G Cai, *Micro milling technologies for MEMS*, Proc. MEMSTECH 2007, Lviv-Polyana, Ukraine, 86-95 (2007).
- [B19] GI Kuznetsov, *Cathodes for electron guns*, Physica Scripta., **T71**, 39-45 (1997).
- [B20] For example: <http://education.jlab.org/itselemental/ele014.html>
- [B21] L Jiang and SM Spearing, *A reassessment of materials issues in microelectromechanical systems (MEMS)*, J. Indian Institute of Science, **87**(3), 363-385 (2007).
- [B22] PG Neudeck, RS Okojie and LY Chen, *High-temperature electronics – a role for wide bandgap semiconductors?*, Proc. IEEE, **90**(6), 1065-1076 (2002).
- [B23] A Ketsdever and J Mueller, *Systems considerations and design options for microspacecraft propulsion systems*, Proc. AIAA 35th Joint Propulsion Conference, Los Angeles, California, Paper 2723 (1999).
- [B24] Silicon Quest International: <http://www.siliconquest.com/>
- [B25] Soitec: <http://www.soitec.com/>
- [B26] RK Williams and DL McElory, *Title*, USAEC, ORNL-TM-1424, **pages?** (1966).
- [B27] QA Huang and NKS Lee, *Analysis and design of polysilicon thermal flexure actuator*, J. Micromech. Microeng., **9**, 64-70 (1999).
- [B28] S Gupta, *Effect of Born and BF_2^+ implant on polysilicon resistors*, J. Electrochem. Soc., **149**(4), G271-G275 (2002).
- [B29] F Meng and R Cui, *Novel model of electrical conduction property at grain boundary in polysilicon*, Jpn. J. Appl. Phys., **41**, 185-189 (2002).
- [B30] M Sciuto, L Papalino, C Gagliano, M Padalino, C Coccorese, D Mello, G Renna and G Franco, *Deposition pressure influence on morphological and electrical properties of polysilicon*, Cryst. Res. Technol., **40**(10-11), 955-957 (2005).
- [B31] VG Kutshoukov, L Pakula, GOF Parikesit, Y Garini, LK Nanver and A Bossche, *Fabrication of nanofluidic devices in glass with polysilicon electrodes*, Sensors and Actuators A, **123-124**, 602-607 (2005).
- [B32]
- [B33] For example: <http://www.goodfellow.com/csp/active/gfMaterialTables.csp>
- [W1] T Sarver-Verhey, *Continuing life test of a xenon hollow cathode for a space plasma contactor*, Proc. AIAA 30th Joint Propulsion Conference, Indianapolis, Indiana, Paper 3312 (1994).
- [W2] T Lundström, *Structure, defects and properties of some refractory bodies*, Pure & Appl. Chem., **57**(10), 1383-1390 (1985).
- [W3] P Frigola, G Andonian, S Reiche, JB Rosenzweig, S Telfer and G Travish, *Design and operation of PEGASUS thermionic cathode*, Proc. Particle Accelerator Conference, Portland, Oregon (2003).
- [W4] H Ahmed, PL Kanitkar, CV Dharmadhikari and DS Joag, *A new method for melting and recrystallization of lanthanum hexaboride (LaB_6) for preparing field emitters*, J. Phys. E: Sci. Instrum., **9**, 4-5 (1976).
- [W5] ED Gibson and JD Verhoeven, *The preparation of single crystal LaB_6 cathodes for electron microscopes*, J. Phys. E: Sci. Instr., **8**, 1003-1004 (1975).
- [W6] Electron Microscopy Sciences: <http://www.emsdiasum.com/microscopy/products/microscope/lab6.aspx#81080>

- [W7] DM Goebel, RM Watkins and KK Jameson, *LaB₆ hollow cathodes for ion and Hall thrusters*, J. Propulsion and Power, **23**(3), 562-570 (2007).
- [W8] JE Polk, DM Goebel, R Watkins, K Jameson, L Yoneshige, J Przybylowski L Cho, *Characterization of hollow cathode performance and thermal behaviour*, Proc. AIAA Joint Propulsion Conference, Sacramento, Arizona, Paper 5150 (2006).
- [W9] LW Swanson, JT Dickinson and DR McNeely, *Fabrication and surface characterization of composite refractory compounds suitable for thermionic converters*, NASA Contractor Report CR-2668, (1976).
- [W10] Metall Rare Earth Limited: <http://www.metall.com.cn/>
- [W11] Cathay Advanced Materials Limited: <http://www.cathaymaterials.com/>
- [W12] Applied Physics Technologies Incorporated: <http://www.a-p-tech.com/>
- [W13] M Nakamoto, T Hasegawa, T Ono, T Sakai and N Sakuma, *Low operation voltage field emitter arrays using low work function materials fabricated by transfer mold technique*, Electron Devices Meeting International, 297-300 (1996).
- [W14] Y Okamoto, T Aida and S Shinada, *DC gas-discharge display panel with LaB₆ thin-film cathode*, Japan J. Appl. Phys., **26**(10), 1722-1726 (1987).
- [W15] DO Hayward and N Taylor, *A simple method of coating ionization gauge cathodes with lanthanum hexaboride*, J. Sci. Instrum., **43**, 762-763 (1966).
- [W16] X Wang, Z Lin, K Qi, Z Chen, Z Wang and YJiang, *Field emission characteristics of lanthanum hexaboride coated silicon field emitters*, J. Phys. D: Appl. Phys., **40**, 4775-4778 (2007).
- [W17] J Pelletier and C Pomot, *Work function of sintered lanthanum hexaboride*, Appl. Phys. Lett., **34**(4), 249-251 (1979).
- [W18] K Johnson and AN Daane, *The lanthanum-boron system*, J. Phys. Chem., **65**, 909-915 (1961).
- [W19] V Craciun and D Craciun, *Pulsed laser deposition of crystalline LaB₆ thin films*, Appl. Surf. Sci., **247**, 384-389 (2005).
- [W20] S Schmidbauer, H Klose, A Ehrlich, M Friedrich, M Röder and F Richter, *Vacuum arc deposition of thin films from an LaB₆ cathode*, Surface and Coatings Technology, **82**, 247-253 (1996).
- [W21] SJ Mroczkowski, *Electron emission characteristics of sputtered lanthanum hexaboride*, J. Vac. Sci. and Tech. A, **9**(3), 586-590 (1991).
- [W22] DJ Warner, RD Branam, WA Hargus Jr and Dm Goebel, *Low current cerium hexaboride and lanthanum hexaboride hollow cathodes*, Proc. 46th AIAA Aerospace Sciences Meeting and Exhibit, Reno, Nevada, Paper 1086 (2008).

APPENDIX

14. MEMS Processing Techniques

The field of microelectromechanical systems (MEMS) is now relatively mature, with sensors, actuators, fluidic and other mechanical systems routinely fabricated at micron and sub-micron scales using a variety of materials and techniques. With respect to the fabrication of a MEMS version of a hollow cathode microthruster, of particular interest are the materials and processing techniques used commonly in the semiconductor industry, not least because their adoption facilitates an economic benefit wherein existing manufacturing equipment may readily be utilised without need of modification or further capital expenditure. Understandably, to make use of this advantage necessitates that the constraints and limitations imposed in standard silicon processing techniques must be considered and adhered to at the design stage for any potential prototype microthruster architecture. Some of the more conventional processing techniques used in the semiconductor industry that could be applied here are described in the following sections.

14.1. Photolithography

Typically, a MEMS structure, like a microfabricated electronic circuit, is built up from a number of successive functional layers, each aligned with respect to the others and defined by a series of patterns or artworks. At the heart of the process lays the technique of lithography: the process by which a required pattern that constitutes a single part of a feature or structure of a MEMS device is transferred to the substrate material prior to its production. Depending on the type of energetic beam used in this process, lithography can be sub-divided into photolithography, electron beam lithography, X-ray lithography and ion lithography. Of these four patterning techniques, photolithography is the more commonly used, but is limited to producing two-dimensional, lateral structures and its resolution is also limited by the wavelength of the light source used.

In photolithography, a photosensitive emulsion layer, referred to as a resist, is used to transfer a desired pattern from a transparent mask to the substrate surface. The resist is usually deposited upon the substrate material by spin coating, although other methods can be employed such as electrochemical deposition, depending on the nature of the resist material. The mask used to transfer the pattern requires high contrast and is typically a transparent glass plate on which a metal pattern (usually chromium) is defined. By comparison, electron beam and ion lithography directly ‘write’ the pattern on to the resist layer by steering the path of an electron or ion beam under computer control over the resist coated substrate surface.

The process of lithography comprises three process steps:

- **Positioning:** In which the mask is laterally positioned on the resist coated surface of the substrate, making use of pre-defined registration markers.
- **Exposure:** In which the pattern is transferred to the resist layer by changing properties of areas exposed to the incident radiation (*e.g.* polymerisation).
- **Development:** This may involve either dissolution (for a negative resist) or etching (for a positive resist) of the resist pattern in a developer solution.

Generally, when patterning simple, thin structures such as metal layers for electrical connectors, photolithography using standard resists is the technique of choice because of its simplicity and quick turn-around time. However, with MEMS devices there is invariably a requirement to fabricate a deep (or thick) structure and in these instances, special resists such as SU-8 (which itself may be used as a MEMS functional material) and/or high-energy beams such as X-rays should be used. Under certain circumstances, silicon nitride or silicon dioxide may be used as a resist material, particularly when highly energetic radiation sources are used as the image forming source and delicate features already created need protecting.

14.1.1. Subtractive Pattern Transfer

In the subtractive pattern transfer technique, material is selectively etched from a functional layer using a pattern defined by the photolithography mask. The process starts by first coating the substrate with a layer of the required functional material as shown in Figure 2a. After spin coating the photoresist layer and selecting the right combination of resist type (positive or negative) and mask type (dark-field or clear-field), the pattern is transferred from the mask to the resist layer (Figure 2d). A subsequent selective etching process further transfers the structure to the functional layer (Figure 2e) before washing away the photoresist reveals the desired structure patterned into the functional layer (Figure 2f).

14.1.2. Additive Pattern Transfer

The most common additive technique used to transfer a pattern is known as the lift-off technique. Here, the substrate is first spin coated with the required resist type (Figure 46b) and the required pattern is then transferred to the resist layer by using photolithography through either a dark-field or clear-field mask (Figure 46d). The required functional material is then directly deposited over the developed and patterned photoresist layer (Figure 46e). By washing away the photoresist, the material that is deposited on the resist layer is also removed and the remaining functional material defines the transferred pattern (Figure 46f).

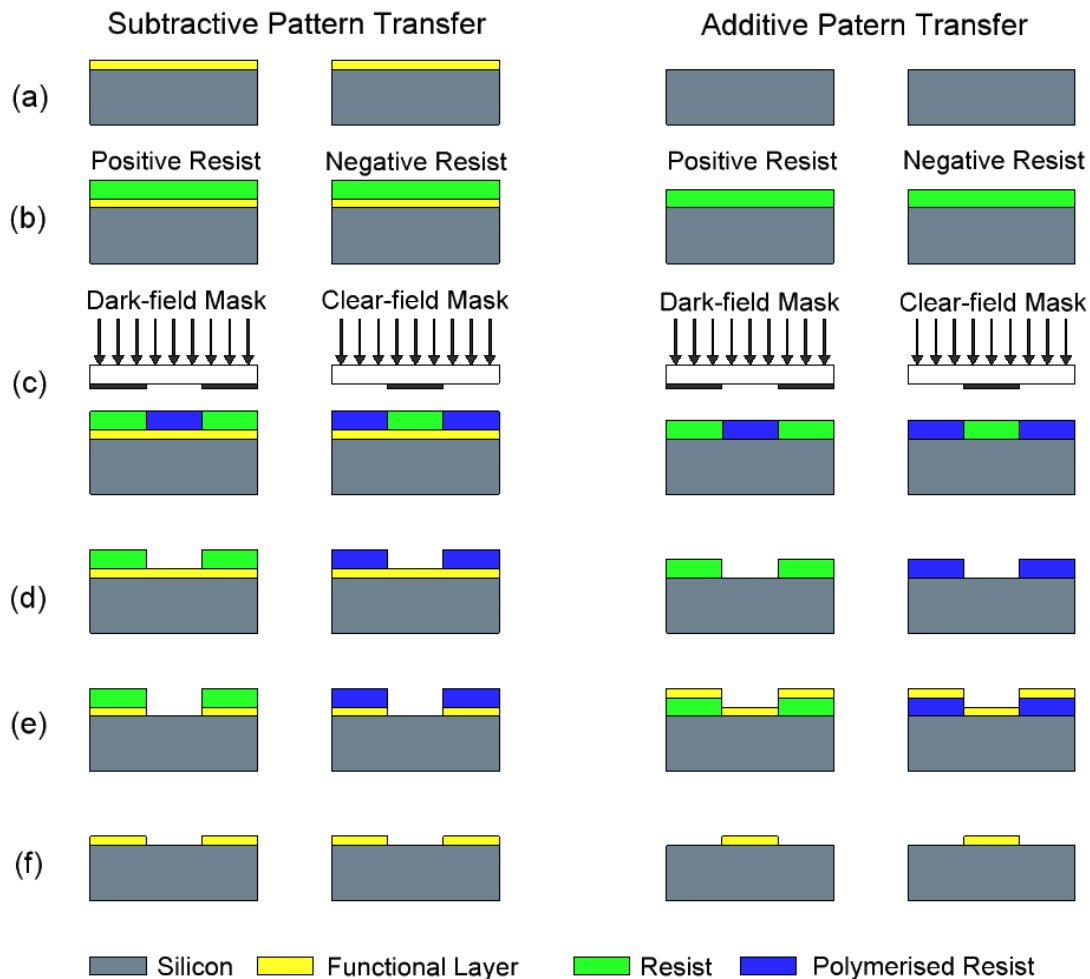


Figure 45 Process steps (top to bottom) for both subtractive and additive pattern transfer using positive and negative resists. (a) Deposition of functional material for subtractive pattern transfer process. (b) Coating of resist layer, either positive or negative. (c) Photolithography using dark-field mask or clear-field mask depending on resist type. (d) Developing resist. (e) Etching of functional material for subtractive pattern transfer technique or deposition of functional material for positive pattern transfer technique. (f) Removal of resist to leave pattern.

Other additive pattern transfer techniques use selective electroplating to transfer structures. The technique starts with the deposition of a metal seed layer on to a substrate surface or defined region of a substrate. After spin coating and developing a thick layer of resist, the functional material is deposited on to the seed layer by electroplating, using the seed layer as an electrode in an electrochemical cell. The resist is then removed as before to leave the required functional structure secured to the seed layer. The advantage of electroplating over other deposition techniques, such as sputtering, are the low cost and fast deposition rate though sputtered or evaporated films are generally smoother.

14.2. Subtractive Processes

Generally, subtractive processes involve the selective removal of material by chemical means (etching) or by physical means (milling).

14.2.1. Wet Etching

There are a number of different CMOS etching processes that can be used to form micromachined MEMS structures and features if the silicon substrate is first suitably ‘masked’ such that only selected regions are exposed to the etchant. Liquid etchants such as nitric acid (HNO₃) and

hydrofluoric acid (HF) in water or acetic acid (CH_3COOH) attack all exposed surfaces equally and can be used to undercut masked areas as shown in Figure 47b. Referred to as an isotropic chemical wet-etch, these processes typically exhibit etch rates from about 1-10 microns per minute depending on the concentrations of the acids used and the operating temperature [B11]. Of course, the undercutting effect is often considered undesirable particularly when designing lateral structures. Isotropic wet-etching is often used for removing thin layers or for thinning down a material or film. Stirring has a big impact on the etching results, because reaction products may act as a barrier between the etchant and the material surface. If the etchant solution is well stirred, then the isotropic etch front takes on a spherical form.

By comparison, etchants such as potassium hydroxide (KOH), hydrazine, ethylene diamine pyrocatechol (EDP) or tetramethyl ammonium hydroxide (TMAH) attack the crystallographic $\{111\}$ planes of silicon at a much slower rate than the other planes to produce sloping sidewall structures as shown in Figure 3c. These sloping walls follow the $\{111\}$ planes which form a 54.7° angle with the surface for a $\{100\}$ oriented silicon substrate and are effectively self regulating: the etching process coming to an end when four complete $\{111\}$ walls are exposed [B12]. Known as an anisotropic chemical wet-etch, etching rates are slower than their isotropic counterpart, typically about 1 micron per minute [B11], with the exact rate controlled by the concentration of the etchant solution and processing temperature. In practice, EDP and TMAH are typically used for bulk micromachining of silicon, and whilst these etchants remove the silicon at a high rate, the masking layer or any exposed metals are generally unaffected, depending on their composition.

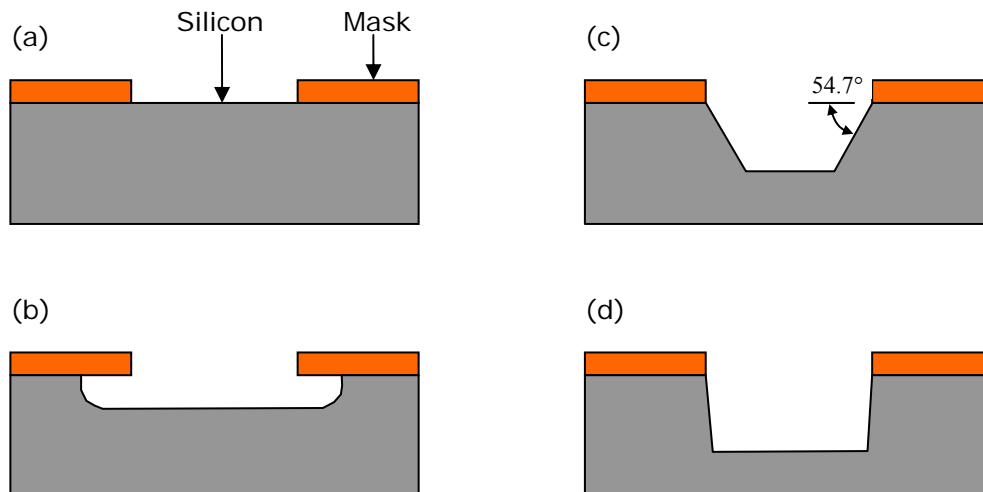


Figure 46 Etch profiles for various techniques on a $\{100\}$ silicon wafer (after [B13])

Some common recipes for wet-etching are listed in Table 11.

Base material	Etchant	Selective to
Si	HF, HNO_3 , CH_3COOH	SiO_2
Si	KOH	SiO_2
SiO_2	NH_4 , HF	Si
SiO_2	HF, HNO_3 , H_2O	Si
SiO_2	H_3PO_4 , HNO_3 , H_2O	Si
Si_3N_4	H_3PO_4	SiO_2
Al	H_3PO_4 , HNO_3 , H_2O	SiO_2

Table 11 Examples of wet etchant recipes.

14.2.2. Dry Etching

A number of different dry etching techniques are available. **Physical dry etching** utilises beams of ions, electrons or photons to bombard the material surface. The kinetic energy of the beam components knocks out atoms from the material surface, which are then evaporated within the high energy beam. Almost all materials can be etched by this process. However, there are some drawbacks, including: slow etch rates; low selectivity (because the beam attacks all materials) and trench effects caused by reflected ions.

Chemical dry etching uses a chemical reaction between etchant gases to attack material surfaces. The process is isotropic and similar to wet-etching in that it exhibits good selectivity. The etchant gases are either excited in an RF field to form a plasma, or react directly with the material to be etched. The process can be self-limiting because the deposition of reaction products can stop the etching process. Chemical dry etching can be used for cleaning and preparing silicon wafers. For example, photoresist can be removed with an oxygen plasma.

Reactive-ion etching is one of the most important techniques in micromachining and uses a plasma beam of chemically reactive ions to remove material. Under low pressures and a strong electrical field, ions hit the substrate surface almost perpendicularly, producing relatively vertical sidewalls as depicted in Figure 47d. Of the numerous types of reactive-ion etching techniques, the **deep reactive-ion etching** technique (DRIE), as exemplified by the Bosch process, is the most useful in the fabrication of MEMS structures. In this technique, the etching process repeatedly alternates between two phases: a plasma etch phase during which material is removed and a passivation phase during which a chemically inert material is deposited over the etched sidewalls to prevent further etching. This etching process is highly anisotropic, allowing deep features to be etched with very straight wall sections up to aspect ratios as high as 30:1. However, the cyclic nature of the process inevitably results in a stepped sidewall profile, with undulations of amplitude in the range 0.1 to 0.5 μm depending on the etch cycle time. Some common etch chemistries for different materials are given in Table 12.

Material Being Etched	Etching Chemistry
Deep Si trench	HBr/NF ₃ /O ₂ /SF ₆
Shallow Si trench	HBr/Cl ₂ /O ₂
Polysilicon	HBr/Cl ₂ /O ₂ , HBr/O ₂ , BCl ₃ /Cl ₂ , SF ₆
Al	BCl ₃ /Cl ₂ , SiCl ₄ /Cl ₂ , HBr/Cl ₂
AlSiCu	BCl ₃ /Cl ₂ /N ₂
W	SF ₆ only, NF ₃ /Cl ₂
TiW	SF ₆ only
WSi ₂ , TiSi ₂ , CoSi ₂	CCl ₂ F ₂ /NF ₃ , CF ₄ /Cl ₂ , Cl ₂ /N ₂ /C ₂ F ₆
SiO ₂	CF ₄ /O ₂ , CF ₄ /CHF ₃ /Ar, C ₂ F ₆ , C ₃ F ₈ , C ₄ F ₈ /CO, C ₅ F ₈ , CH ₂ F ₂
Si ₃ N ₄	CF ₄ /O ₂ , CHF ₃ /O ₂ , CH ₂ F ₂ , CH ₂ CHF ₂

Table 12 Etch chemistries for different etching processes.

14.2.3. Milling

Milling is the general term applied to a number of processes that selectively remove materials by physical means. Included here is **focused ion-beam** milling (FIB) where a focused beam of highly energetic particles are used to ablate or sputter a targeted region of a surface [B14]. Resembling a scanning electron microscope, the FIB milling machine uses electrostatic lenses to focus charged gallium ions onto the region to be milled which then sputters atoms from the surface. In so doing, some gallium atoms will be implanted into the top few nanometres of the exposed surface, which

can be disadvantageous. This technique is capable of removing material down to feature sizes of the order of a few 10's of nanometres [*ibid.*]. A more refined technique is that of **adaptive ion-beam** milling (AIM) which utilises a versatile ion gun assembly with controllable energy for aggressive milling but is also capable of gentle milling, and a versatile controllable dynamic beam that can impact a specimen at a multitude of angles of attack.

Laser milling involves targeting a substrate material with short pulses of laser light ranging from microsecond to femtosecond duration. The power delivered by the laser in these short pulses is sufficient to thermally evaporate material in very localised regions. The feature size resolution achievable by this technique is dependant on the beam spot size of the incident radiation, which in turn is dependant on its wavelength [B15] and can be focused down to a few microns [B16, 17].

Whilst the previously described methods can be considered true semiconductor microfabrication technologies, an alternative technique for producing micro-scale features in materials other than silicon is the mechanical process of **micro-milling** [B18]. As its name implies, this technique uses very fine milling tools (of the order of 0.05mm diameter) in a conventional computer controlled milling machine, removing material by physical abrasion/grinding and is suitable for producing trenches, slots, vias and cavities in machineable ceramics and glasses. This technology offers an economic advantage of those previously described and is often favoured in microfluidics as a means of producing fluidic channels in support structures such as plenums and manifolds and where accuracy of alignment is not too critical.

14.3. Additive Processes

There are a myriad of processes that can be used to deposit functional materials onto a substrate surface. The choice of process used is usually governed by what equipment is available, the composition of the material to be deposited and by the composition of what materials (if any) have already been deposited.

14.3.1. Chemical Vapour Deposition

Chemical vapour deposition (CVD) is one of the most important techniques for depositing films of functional materials onto the surface of a substrate. In a CVD process, gaseous reactants that contain the required functional material are introduced into a reaction chamber housing the substrate structure. The substrate is heated, resulting in the solid deposition of the functional material from the gas phase, whilst other gaseous reaction products are exhausted from the chamber. Depending on the reaction conditions, CVD processes are further categorised as: **atmospheric pressure chemical vapour deposition** (APCVD); **low-pressure chemical vapour deposition** (LPCVD) and **plasma-enhanced chemical vapour deposition** (PECVD).

APCVD and LPCVD involve elevated temperatures ranging from 500°C to 800°C and as such are too high for metals with low eutectic temperature with silicon, such as gold (380°C) or aluminium (577°C). In the PECVD process, parts of the energy is contained within the plasma and thus lower substrate temperatures are needed, typically in the order of 100°C to 300°C.

14.3.2. Physical Vapour Deposition

Physical vapour deposition (PVD) creates functional films on a substrate directly from a source of the required material. The technique covers two physically different methods: evaporation and sputtering.

Evaporation deposits thin films of material on a substrate by sublimation of a heated source material in a vacuum. Depending on the heating method employed, this technique can be further categorised as **vacuum thermal evaporation (VTA)**, **electron beam evaporation (EBE)**, **molecular beam epitaxy (MBE)** or **reactive evaporation (RE)**, the first two of which being the most common. VTA uses resistive heating, laser heating or magnetic induction to raise the source material temperature. In EBE, the electron beam is focused on the target material causing localised melting and evaporation.

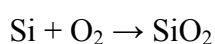
In **sputter deposition**, the target source is bombarded with chemically inert atoms, such as argon, thereby releasing a flux of atoms from the target which condense on the substrate surface as a thin film. Sputtering sources are usually magnetrons that utilise strong electric and magnetic fields to trap electrons close to the surface of the target material. The electrons follow helical paths around the magnetic field lines undergoing more ionising collisions with the argon gas near the target surface than would otherwise occur. The ionised argon gas particles are accelerated toward the target by virtue of the latter being held at an opposing potential. The sputtered atoms that are ejected from the target surface as a result of the bombardment are neutrally charged and so are unaffected by the magnetic trap. The process can deposit all types of materials including alloys, insulators and piezoelectric ceramics. The process is less directional than EBE but offers higher deposition rates. An important advantage of sputter deposition is that even high melting point materials are easily sputtered while evaporation of these materials in a resistance evaporator is problematic or impossible. In addition, sputter deposited films have a composition close to that of the source material and typically exhibit better adhesion to the substrate than evaporated films. It is possible for charge build-up to occur on insulating targets, when depositing insulating films, though this can be avoided with the use of **RF sputtering** where the polarity of the target potential is varied at a high frequency.

Ion-beam sputtering (IBS) is a method in which the target is external to the ion source. The source ions are generated by collisions with electrons that are confined by a magnetic field as in a magnetron and are then accelerated by the electric field emanating from a grid toward a target. As the ions leave the source they are neutralised by electrons from a second external source. Since the flux that strikes the target is composed of neutral atoms, either insulating or conducting targets can be sputtered. IBS has an advantage in that the energy and flux of ions can be controlled independently. The principal drawback of IBS is the large amount of maintenance required to keep the ion source operating.

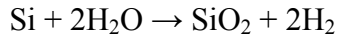
In **reactive sputtering**, the deposited film is formed by chemical reaction between the target material and a gas that is introduced into the vacuum chamber. Silicon oxide and silicon nitride films are often fabricated using this method because the stoichiometry of the film, and hence the film properties, can be finely controlled by varying the relative pressures of the inert and reactive gases.

14.3.3. Thermal Oxidation

Although silicon dioxide can be deposited by CVD, thermal oxidation is the simplest technique to create a silicon dioxide layer on exposed silicon surfaces. Depending on the type of oxidising agent, thermal oxidation is categorised as dry oxidation or wet oxidation. In dry oxidation, pure oxygen reacts in a furnace with silicon at high temperatures ranging from 800°C to 1200°C, according to:



In wet oxidation, water vapour reacts with silicon at high temperatures according to:



14.3.3.1. Sol-Gel Deposition

In a sol-gel deposition process, solid particles of a functional compound are dissolved in an appropriate solvent which is spin-coated on the substrate surface. Subsequent drying removes the solvent resulting in a solid film. Additional processing is sometimes required to solidify further the deposited film or to strengthen its bond to the substrate surface. This technique is ideal for depositing particular films over larger surface areas.

14.3.3.2. Spin Coating

Spin coating is the simplest method for depositing a film on a substrate and is the method of choice for coating resists used in lithography. Spin coating is typically used for depositing polymers or precursors for polymers. Similar to the sol-gel process, the material of interest is dissolved within a solvent which is then dripped onto the substrate surface and spun at high speed (of the order of 5000 rpm). Centripetal forces, surface tension and viscosity determine the thickness of the coated film in a predictable and repeatable manner. Part of the solvent is evaporated during the spinning process and the remainder is baked out at temperatures in the range 100°C to 200°C. Spin coating results in a relatively smooth, planar surface, even when deposited over a non-planar substrate. As such, this technique can also be used for planarisation purposes.

14.3.3.3. Ion Implantation

Sometimes not always thought of as an additive process, this technique is in fact one of the most important processes in microelectronics. The technique involves adding impurities to the substrate material and can be quite localised. Adding dopant atoms to silicon with three valence electrons, such as boron, creates positively charged carriers (holes). The resultant silicon is referred to as p-type. Conversely, adding dopant atoms with five valence electrons, such as phosphorous, creates negatively charged carriers (electrons), and silicon of this type is referred to as n-type. Ion implantation can also be used to form a buried insulating layer, such as silicon dioxide, in the substrate. At high temperatures, oxygen ion implantation creates an oxide layer with depths ranging from 0.1 to 1.0 µm from the substrate surface. The crystal defects in silicon above this layer are repaired automatically by the high temperatures used in the process. This particular technique is called **separation by implantation of oxygen (SIMOX)**.

14.3.3.4. Electrochemical Deposition

If the substrate material is electrically conductive, it can be used as an electrode in an electrochemical cell. As such, all manner of materials may then be grown over the exposed surface of this electrode depending on the cell solution and the potential applied to this cell with respect to a reference electrode contained within the same cell. Film growth rates and hence thicknesses are

dependant on the current density (following Faraday's laws). This technique is particularly useful for depositing films on surfaces that are otherwise occluded to techniques such as CVD and sputtering.

14.4. Bonding

In some circumstances, it is more convenient (or technically necessary) to realise a MEMS structure on two or more substrates which then must be bonded together as a final fabrication step. A number of MEMS compatible processes exist that serve this purpose.

14.4.1. Anodic Bonding

Anodic bonding is used to join silicon to glass, but can also be used to bond silicon to silicon if an intermediate glass layer is used between the two. The process is essentially an electrostatic technique and is performed at elevated temperatures (of the order of 400°C) and high electric field strength, with bonding voltages typically of the order of 1 kV. In the process, the silicon substrate is connected to the positive electrode and serves as an anode, which gives the name to this technique, whilst the glass is connected as a cathode. Because the process occurs at relatively high temperatures the thermal expansion coefficients of the silicon and glass must be matched to reduce the chances of thermal stresses causing microcracks at the interface when cooling down. Consequently, the number of glasses that can be used by this process is limited, but does include Pyrex.

14.4.2. Direct Bonding

Also known as **silicon fusion bonding**, this process directly bonds two silicon wafers to each other without the need for an intermediate layer. This is an important feature of the process, since the lack of an intermediate layer removes the complication of thermal coefficient mismatches and the concomitant possibilities of thermal stress induced fractures.

Silicon direct bonding utilises the reaction between hydroxyl groups (OH) present at the surface of the silicon substrates (either native or deposited). The substrates are first hydrated by immersion in an H₂O₂/H₂SO₄ mixture, boiling nitric acid or diluted sulphuric acid before being brought into contact and then bonded at elevated temperatures in the range 300°C to 1000°C. Subsequent annealing of the bonded composite can improve bond quality.

14.4.3. Eutectic Bonding

Eutectic bonding is a common packaging technique used in microelectronic fabrication. Gold-silicon eutectic bonding is achieved at a relatively low temperature of 363°C. For this purpose, thin layers of gold can be sputtered over the surface of the silicon structure.

14.4.4. Adhesive Bonding

Adhesive bonding uses an intermediate layer of material to 'glue' two substrates together. Depending on the substrate materials and intended application, the intermediate layer can be glass, epoxies, photoresists or other polymer materials, which can be deposited using any of the additive techniques previously described.